TECHNISCHE UNIVERSITÄT ILMENAU

Design and Testing of Compact Dual-band Dual-polarized Robust Satellite Navigation Antenna Arrays

DOCTORAL THESIS

For attaining the academic degree of

Doctor of Engineering (Dr.-Ing.)

Presented to the Faculty of Electrical Engineering and Information Technology, Technische Universität Ilmenau

By: M.Sc. Maysam Ibraheam
(19.06.1982)

Reviewed by:
- Univ.-Prof. Dr. rer. nat. habil. Matthias Hein
- Univ.-Prof. Dr.-Ing. habil. Reiner S. Thomä
- Univ.-Prof. Dr.-Ing. habil. Michael Meurer

Submitted on: 12. Feb. 2018
Defended on: 05. Jul. 2019

urn:nbn:de:gbv:ilm1-2019000261

Abstract

The increasing demand for accurate positioning solutions for highly-automated driving and safety-critical applications motivates the use of array-based satellite navigation receivers that feature better performance, due to the enhanced diversity gain and the potential beamforming capability. The need for improving the robustness of navigation receivers against sources of signal distortion such as multipath propagation, atmospheric impact, jamming, and spoofing violations requests to extend the receiver to exploit polarization and frequency diversities. The resulting design is challenged by the significant rise in hardware and software complexity. This complexity increases even more with the trend to miniaturize the navigation receiver, to ease the integration in vehicles or mobile systems, because mutual coupling rises between the radiating elements of the receiver, and deteriorates their radiation efficiencies and polarization purities, and hence degrades the system robustness. In this thesis, a compact dual-band dual-polarized array-based navigation receiver that uses array diversity, frequency diversity, and polarization diversity is studied and designed, to provide robustness against the different types of distortions. The main contributions of the presented work include the design of the dual-band dual-polarized patch antenna element, the design of the compact antenna array, the study of the cross-polarization sources in patch antennas, the analysis of the mutual coupling impact on radiation efficiency and polarization purity of radiating elements, and the mitigation of both impacts using eigenmode-based decoupling and matching networks. Furthermore, the work also involves the integration of the antenna system with an RF-IF front-end, developed in cooperation with IMMS GmbH, for power amplification, filtering, and down-converting. The dissertation covers also the integration with an array-based digital receiver, developed in cooperation with RWTH Aachen University and the German Aerospace Center (DLR), to implement data acquisition, direction-of-arrival estimation, beamforming, and anti-jamming algorithms. The feasibility of both the array diversity and the polarization diversity was confirmed in automotive-related field measurements, particularly for elevations below 40° and 60°, respectively; i.e., at directions far from the main beam direction of the even mode of the array (at zenith), and where the impact of multipath propagation on strength and polarization of the signal reaches sufficient levels to disturb the receiver. Measurements proved the receiver robustness against jamming-to-signal ratios up to 85 dB, outperforming several state-of-the-art receivers described in literature.

Kurzdarstellung

Die steigende Nachfrage nach präzisen Positionierlösungen für hochautomatisiertes Fahren und sicherheitskritische Anwendungen führt zu der Verwendung von Array-basierten Satellitennavigationsempfängern, die aufgrund des verbesserten Diversity-Gewinns und der potentiellen Strahlformungsfähigkeit eine bessere Leistung aufweisen. Die Notwendigkeit, die Robustheit von Navigationsempfängern gegenüber Quellen von Signalstörungen, wie Mehrwegempfang, atmosphärische, sowie Jamming- und Spoofing-Störungen, zu verbessern, verlangt, den Empfänger weiter auszubauen, um beispielsweise Polarisations- und Frequenz-Diversity auszunutzen. Das hieraus resultierende Design ist durch eine signifikante Zunahme der Hardware- und Softwarekomplexität gekennzeichnet. Diese Komplexität steigt noch mit dem Trend, den Navigationsempfänger zu miniaturisieren, um die Integration in Fahrzeugen oder mobilen Systemen zu erleichtern. Da die gegenseitige Verkopplung zwischen den Antennenelementen eines kompakten Antennen- Arrays steigt, verschlechtert sich deren Strahlungseffizienz und Polarisationsreinheit und damit die Systemrobustheit. In dieser Arbeit wird ein kompaktes, dualbandiges und dualpolarisiertes Antennenarray für einen Navigationsempfänger untersucht, schaltungstechnisch entworfen und aufgebaut, womit Array-, Frequenz-, und Polarisations-Diversity ermöglicht wird. Dies führt zu einer signifikant verbesserten Robustheit gegenüber den bereits oben angesprochenen Störungen. Die Hauptbeiträge der vorgestellten Arbeit umfassen das Design des dualbandigen und dualpolarisierten Patchantennenelements, das Design des kompakten Antennenarrays, das Studium der Kreuzpolarisationsquellen in Patchantennen, die Analyse des Einflusses der gegenseitigen Kopplung auf die Strahlungseffizienz und Polarisationsreinheit strahlender Elemente, und die Abschwächung beider Auswirkungen unter Verwendung von eigenmodebasierten Entkopplungs- und Anpassungsnetzwerken. Darüber hinaus beinhaltet die Arbeit die Integration des Antennensystems in ein HF- Frontend, das in Kooperation mit der IMMS GmbH entwickelt wurde. Dieses dem Antennenarray nachgeschaltete Frontend ist zur Leistungsverstärkung, Filterung und Signalkonvertierung der Satellitensignale erforderlich. Die Dissertation umfasst auch die Integration mit einem Array-basierten digitalen Empfänger, der in Zusammenarbeit mit der RWTH Aachen Universität und dem Deutschen Zentrum für Luft- und Raumfahrt (DLR) entwickelt wurde, in dem neben der Datenerfassung, auch die Richtungsschätzung, das Beamforming und die Anti-Jamming-Algorithmen implementiert wurden. Die Machbarkeit sowohl der Array-Diversity als auch der Polarisations-Diversity wurde in Automotive-related Feldmessungen bestätigt, insbesondere für Elevationswinkel unter 40° bzw. 60°, h. in Richtungen, die von der Hauptstrahlrichtung des Even-Modus der Array (im Zenit) weit entfernt sind, und wo der Einfluss des Mehrwegempfangs gegenüber dem Nutzsignals ausreichend hohe Pegel erreicht, um den Empfänger zu stören. Die Messungen bestätigten die Robustheit des Empfängers gegenüber Stör- Nutzsignalverhältnissen von bis zu 85 dB und übertrafen damit mehrere in der Literatur beschriebene „State-of-the-Art" Empfänger.

Acknowledgements

This thesis is a compilation of my achievements during the work as a research assistant at the RF and Microwave Research Laboratory of Technische Universität Ilmenau. The work was part of the project "Compact satellite receiver system for robust navigation applications (KOSERNA)", which has been performed in cooperation between Technische Universität Ilmenau, Institut für Kommunikation und Navigation (IKN) at the German Aerospace Center (DLR), Institut für Mikroelektronik und Mechatronik Systeme gemeinnützige (IMMS) GmbH, RWTH Aachen University, and Antennentechnik Bad Blankenburg (ABB) GmbH. It was funded by DLR on behalf of the German Federal Ministry of Economics and Technology under grant 50 NA 1405. The research was conducted under the roof of the Thuringian Center for Innovation in Mobility.

Before starting, I would like to acknowledge Univ.-Prof. Dr. rer. nat. habil. Matthias Hein, the head of the RF and Microwave Research Laboratory for initiating this research position, and for introducing me to compact antenna arrays, RF engineering, and robust satellite-based navigation systems. I thank him also for his appreciated efforts to bring this work to a successful state. This includes the detailed theoretical and technical discussions, the comprehensive comments and feedbacks, and the grateful support and guidance.

I also would like to thank Univ.-Prof. Dr.-Ing. habil. Reiner S. Thomä, head of the Electronic Measurement Research Lab at Technische Universität Ilmenau for reviewing and evaluating my thesis, and for all the support and cooperation during my master and doctoral study at TU Ilmenau.

I thank Univ.-Prof. Dr.-Ing. habil. Michael Meurer head of department of Navigation and director of Center of Excellence for Satellite Navigation at DLR, and the professor at RWTH Aachen University, for reviewing and evaluating my thesis, and for joint-work in the project KOSERNA.

I acknowledge the members of the project team, Dr.-Ing. Ralf Stephan, Dr. -Ing. Safwat Irteza Butt, and Dr.-Ing. Kurt Blau, for their scientific and technical contributions, which had a significant role in the successful completion of the work. I, particularly, thank Ralf for the fruitful conversations about antennas and system design, Safwat for the detailed discussions regarding decoupling and matching networks, and the system performance evaluation, and Kurt for the great knowledge of RF systems and RF circuit design.

I am thankful to my senior colleagues at the office, Alexander Krauß, Frank Wollenschläger, Hendrik Bayer, and Saqib Kaleem for the scientific discussions and feedbacks, and for the nice coffee breaks. I thank our technical team, Michael Huhn and Matthias Zocher for the valuable technical help during the work period.

Finally, I thank my big family for their support and encouragement, and my wife Lorean, and my kids, Ashraf and Sarah, for the patience, encouragement, and fruitful accompany during the last years.

Maysam Ibraheam

Ilmenau, 08.02.2018.

Contents

Chapter 1:

Introduction

The robustness of global navigation satellite systems (GNSS) against external interferers or distortions is a critical parameter that defines the capability of these systems to provide location, velocity, and time information with sufficient application-based accuracy and reliability, in the presence of the interferers. This is of high importance for real-time and safety-critical applications such as highly-automated driving, unmanned aerial vehicles, and autonomous maneuvering, where consistent, precise and real-time navigation data are prerequisite to avoid collision and ensure traffic safety.

However, the operation of many of the classical GNSS receivers available in the market depends on a single radiating element, usually a patch antenna, with simple hardware or software solutions dedicated to enhance the receiver robustness against potential sources of signal distortions. Hence, the reliability of these receivers might not be sufficient for the afore-mentioned applications. Therefore, improving the receiver robustness against different types of signal distortions has become an important research field for forthcoming satellite-based navigation receivers, especially in automotive industry [1-7].

Besides the common natural phenomena that adversely affect the performance of GNSS receivers, such as the multipath propagation and the atmospheric impact, jamming has become a growing threat, considering the availability of cheap commercial jamming devices that can block the service of classical receivers [1, 8]. Such types of interruptions raised the need to use adaptive multi-element antenna arrays, to replace the single element at the receive side. Antenna arrays empower the receiver with the ability to implement beam steering algorithms, e.g., to desensitize the radiation pattern at the directions of interferers or jammers [9-15].

Moreover, dual-polarized antennas provide the GNSS receiver with full polarization degrees-of-freedom, to compensate for the impact of multipath propagation on the signal polarization [7, 8, 16, 17]. Additionally, the dual polarization increases the number of degrees-of-freedom for the anti-jamming and null steering algorithms [18, 14, 19, 20]. It is proven in this work that dual polarization also increases the maximum jamming-to-signal ratio (JSR) that can be overcome by the anti-jamming GNSS receiver (JSR-tolerance).

Furthermore, dual- or multi-band GNSS receivers have been developed to improve the positioning accuracy and enhance the receiver robustness against atmospheric effects on the wave propagation [21-23].

In summary, growing efforts have been undertaken to design new generations of robust GNSS receivers that use antenna arrays (gain and spatial diversities), with polarization diversity, and frequency diversity, in addition to dedicated array signal processing techniques, to enable compensation for the atmospheric and multipath impacts on the wave propagation, and to maximize the received power at directions of the wanted signals and null it at directions of unwanted interferers.

This work describes the design, testing and evaluation of a robust dual-band and dual-polarized array-based global satellite navigation receiver, which has been developed under the project name "compact satellite receiver systems for robust navigation applications KOSERNA", in cooperation between the afore-mentioned partners TU Ilmenau, DLR, IMMS GmbH, RWTH Aachen, and Antennentechnik Bad Blankenburg GmbH.

The project is a continuation of previous projects where array-based, but single-polarized, satellite navigation receivers were developed by some partners of this project, namely the dual-band "Galileo Antenna Demonstrator GALANT [24]" developed by DLR, and the single-band "Compact Adaptive Terminal Antenna for Interference-Free Satellite Navigation KOMPASSION [25]" developed by DLR, TU Ilmenau, RWTH Aachen, and IMMS GmbH.

The new receiver, presented in Fig. 1.1, incorporates a four-element dual-band dual-polarized compact antenna array, connected to two eigenmode-based decoupling and matching networks (DMN) [4, 69, 76], to improve the radiation efficiency and cross-polarization discrimination degraded by mutual coupling. The resulting eigenmodes of the array are carried to a calibration circuit, and then fed to an RF-IF front-end for power amplification, frequency filtering, and RF-IF down-converting. Finally, the signals are carried to a digital receiver empowered with array-based algorithms to perform data acquisition, direction-of-arrival estimation, beamforming, and anti-jamming.

The antenna with its decoupling and matching networks and its calibration circuit were developed by TU llmenau. The front-end was developed by TU Ilmenau and IMMS GmbH. The digital receiver was developed in cooperation between RWTH Aachen, DLR, and TU Ilmenau. The robustness of the receiver, with its enhanced array and polarization diversities, were tested against different automotive-related multipath and jamming scenarios, in measurement campaigns run by all partners.

My responsibilities in this work included the antenna array, the decoupling and matching circuits, the calibration circuits, the integration and performance testing of the RF-IF circuits, the integration with the digital receiver, the setup and the performing of the

measurement campaigns in cooperation with the other partners, the analysis of the results, and evaluation of the system.

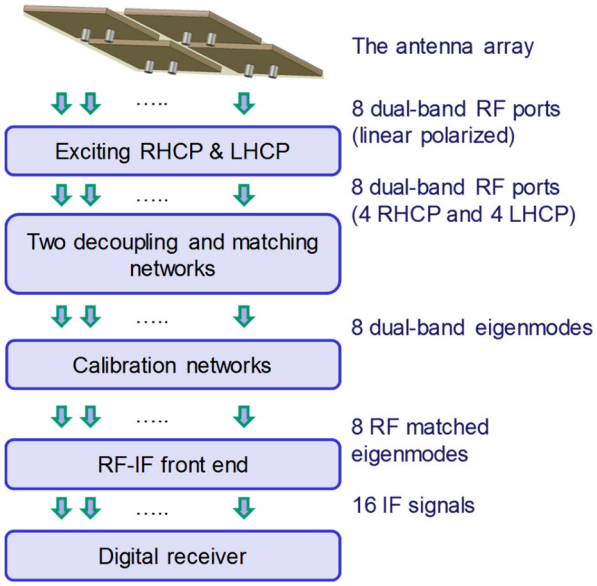

Figure 1.1: A block diagram of the proposed array-based dual-band dual-polarized GNSS receiver, showing the main components and the signal flow.

The automotive-related field measurements proved the usability of the higher-order right-hand circular-polarized (RHCP) eigenmodes of the array for receiving the navigation signals, particularly at low elevations, where the higher order modes have larger gain than the even mode (below 40° for the designed antenna array), and thus to extend the coverage angle of the receiver.

Measurements proved also the usability of the higher-order left-hand circular-polarized (LHCP) modes, particularly the odd modes, to receive the navigation signals at elevations below 60°, and thus to compensate for the polarization distortion caused by the multipath propagation. This, eventually, helps to improve the tracking quality, and hence the positioning accuracy of the receiver. It helps also to improve the anti-jamming robustness level of the receiver.

Measurements helped also to decide which left-hand modes should be selected for practical dual-polarized receiver, where limited number of RF channels can be processed, to reduce the system complexity and costs.

These results confirm the usability of dual-band dual-polarized antenna arrays to extend the scan-angle of GNSS receivers, improve their positioning accuracy, and enhance their robustness against polarization distortions and jamming interferers.

Comparisons found that the developed receiver outperforms several state-of-the-are anti-jamming receivers described in literature, particularly in the anti-jamming robustness level [3, 6, 26-28].

Analyses, to highlight the influence of each part of the analog and digital stages, found that all parts of the receiver are relevant to achieve improved robustness, since each stage of the system highly depends on the others. While array-based anti-jamming signal processing is essential to exploit the array and polarization diversities, a well decoupled and matched antenna array, with optimized array and polarization diversities, is a prerequisite for such a system. Additionally, a proper RF-IF front-end with low noise figure, gain control, and probably the possibility of online calibration, is necessary for the efficient integration of the receiver.

The motivation for the proposed design, together with the state-of-the-art are covered in **Chapter 2**.

The design of the single dual-band dual-polarized GNSS radiating element, with special focus on the polarization characteristics, is covered in **Chapter 3**.

Chapter 4 is dedicated to study the performance of radiating elements in compact antenna arrays, with focus on the impact of mutual coupling on the polarization purity of patch antenna elements.

Chapter 5 describes the receiver construction in detail, with focus on the hardware part of the receiver. The chapter combines the design and layout of the circuits, the circuit-level measurements, and eventually the system integration.

Chapter 6 is devoted to the automotive-related system performance evaluation of the receiver, with focus on the robustness against jamming sources, and the feasibility of array diversity and polarization diversity.

The conclusions and main findings of this thesis are finally presented in **Chapter 7.**

Chapter 2:

Motivation for Robust Satellite Navigation Systems

2.1 Global navigation satellite systems (GNSS)

Acquiring the basic geographical knowledge of the surrounding area, and the possible navigation paths towards resources, or other points of interest, played always a significant role in the history of human civilization.

Global Satellite Navigation Systems are used, nowadays, to fulfill this demand and provide users with the ability to calculate their position, velocity, and time. Advanced GNSS receivers can provide more information such as attitude. GNSS systems may work independently or integrate with other sensors (e.g., inertial measurement units) to improve accuracy and reliability.

A GNSS system, illustrated in Fig. 2.1, is a satellite-based broadcasting system, where satellites orbiting the earth broadcast dedicated L-band RHCP signals with navigation data and ranging codes. The navigation data of each signal contain the position, velocity, and clock bias of the related satellite, while the ranging codes are Pseudo-Random Noise (PRN) sequences that allow the receiver to calculate the travel time of the signal. The travel time and navigation information, if received from at least three satellites, should allow the receiver to calculate its relative position. However, due to the time ambiguity, four satellites are needed to find the position, time, and subsequently velocity information [29, 30, 31].

Several GNSS systems were deployed over the years to respond to the inevitable reliance on this service in wide variety of applications including transport, aviation, automotive, mapping, farming, disaster management, etc. These systems include GPS, GLONASS, Galileo, BeiDou, etc [32, 33].

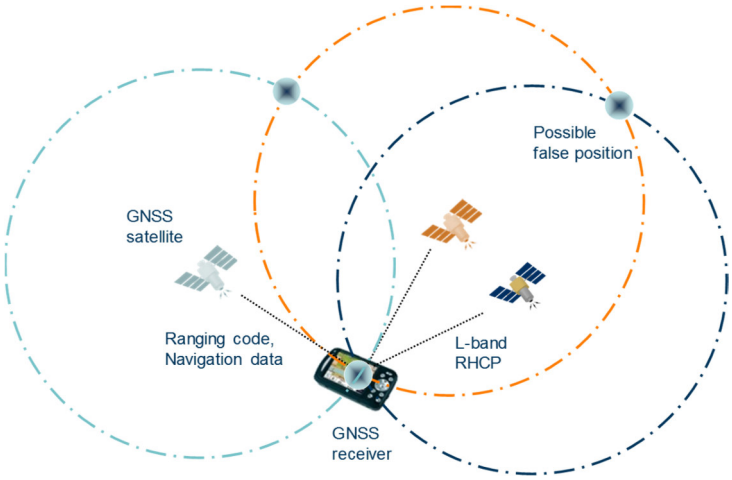

Figure 2.1: Basic illustration of a GNSS system, depicting the GNSS receiver, several GNSS satellites, and the main components of a GNSS signal.

2.2 Sources of signal distortion

With the low receive power at GNSS receivers (typically around -130 dBm), and the small gain of their antennas (typically around 3 dB to 6 dB at the main direction for the widely used patch antennas), these devices are vulnerable to several kinds of distortions that either directly affect the receivers themselves or distort the propagating navigation signals, resulting in positioning errors and decreased reliability, which limits the possibility of using these receivers for automotive or safety-of-life applications.

In addition to possible unintentional interferers from systems working close to the GNSS frequencies, sources of distortion include intentional jamming and spoofing devices, atmospheric impact, and multipath propagation, as illustrated in Fig. 2.2.

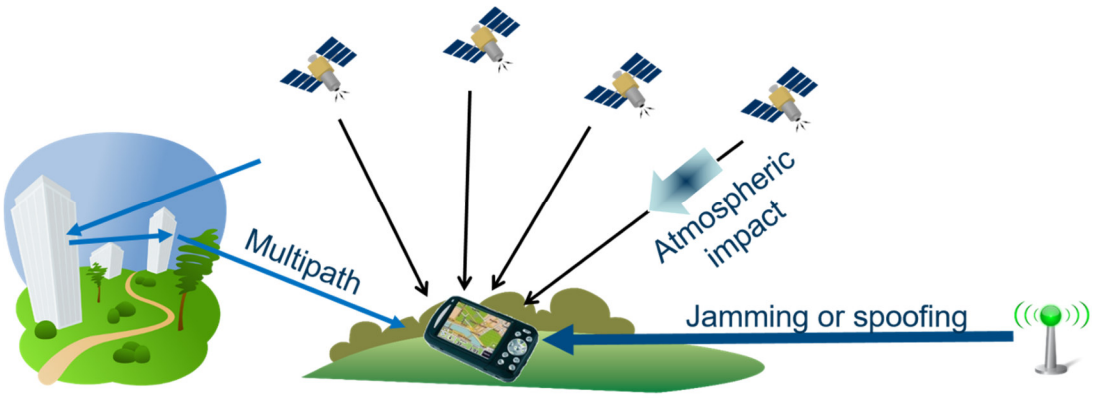

Figure 2.2: Illustration of a GNSS receiver in operation, with possible sources of distortions that may affect the receiver or the navigation signals.

These sources are to be covered in detail in the following paragraphs. The solutions to mitigate the influence of these sources of distortion are discussed thereafter.

2.2.1 Propagation effects (multipath and atmosphere)

Multipath propagation has a strong influence on the performance of GNSS receivers, especially in urban environments. Shadowing may block or limit the service. Reflections attenuate the strength of the reflected signal. The longer traveled-paths add delays, which affect the positioning accuracy. Moreover, instances of the signal coming through different paths add to each other destructively or constructively, resulting in fast fading which influences the stability of the receiver [7, 17, 34-37].

Furthermore, reflected instances of the signal may change their polarization from the nominal right hand circular polarization to the unwanted left hand circular polarization depending on the impinging angle as described in [7, 16, 38]. This phenomenon results in a received signal with stronger LHCP component at the receiver side, which introduces a polarization mismatch with the RHCP receiver.

Additionally, the atmospheric layers could have notable influence on the GNSS signal at certain frequency bands, depending on the weather condition and the direction of arrival of the signal [21, 22, 35, 39].

2.2.2 Intended signal modifications (jamming and spoofing)

One kind of intentional in-band interference is usually referred to as jamming. The jammer, usually, transmits high-power signals at the GNSS frequencies to prevent receivers in the area from operation. One of the most famous types of jammers is the personal privacy device (PPD), which is widely available on the market. The PPD, in the name of protecting the privacy of users from being detected, usually affects a wide area around the user, due to its high power, preventing other users from accessing the service. PPDs, mostly, transmit their signals from low elevations (0° to 15°), either from static or moving devices [1, 8, 40-42].

Despite the noise-like properties of the GNSS signal which make them robust against distortions 20 dB higher than the signal level [26], they fail against greater distortion levels, which can easily be reached by commercial jamming sources, if they were at suitable distances. A jammer, 100 meters away from the receiver, for example, needs a transmit power of only -14 dBm to reach a receive power level of -100 dBm at the receiver and jam it with a jamming-it-signal ratio of about 10 dB, assuming a free space loss of about 76 dB at the operation frequency of 1.575 GHz, and a receiver gain of only -10 dB at the low elevation direction of the jammer.

Spoofing is another kind of intentional interference, where the interferer transmits GNSS-like signals with information of artificial satellites, in order to deceive the receiver to calculate wrong positions [5, 43, 44]. Like jammers, spoofers usually transmit from low elevations, and can be static or dynamic.

2.3 Array-based robust satellite navigation receivers

Increasing efforts have been carried out in the last years to enhance the robustness of GNSS receivers against the aforementioned kinds of distortions. Proposed solutions mainly use antenna arrays and array-based signal processing techniques to compensate for the atmospheric and multipath propagation effects, and to improve the immunity from jamming and spoofing [2, 3, 6, 9-12].

In addition to the spatial diversity achieved by using multi-element antenna arrays, some receivers benefit from either frequency diversity, using multi-band radiating elements, or polarization diversity, using dual-polarized elements [14, 18-23].

In the thesis, in order to acquire all possible degrees-of-freedom, a GNSS receiver that exploits antenna arrays, frequency diversity, and polarization diversity is investigated, designed, and evaluated. Motivations for the use of such a diversity receiver are explained in detail in the following paragraphs.

Being influenced by automotive prerequisite for compactness, the thesis focuses on the design of “compact” antenna arrays, and the impact of the increasing mutual coupling on the array eigenefficiencies, and on the cross-polarization discrimination of the radiating elements, and how to mitigate that.

2.3.1 Antenna arrays

The need for global service coverage, with the limited number of available satellites, and the requirement of providing low dilution of precision (DOP), forced to distribute the GNSS satellites around the earth so that they appear at various elevations and azimuths in the sky-view of a user GNSS receiver. This distribution restricts the usability of the single-element planar microstrip antennas if their radiation patterns were directed to the zenith with poor radiation efficiency and polarization purity at low elevations, which is very common.

This challenge can be partially overcome using radiating elements with patterns of wider beams, at the cost of reducing the gain, increasing the fabrication complexity, and probably influencing the compactness of the device. However, a multi-element planar antenna array empowers the receiver with more degrees-of-freedom, and therefore features higher

diversity gain and enables implementing of advanced array signal processing techniques such as adaptive linear beamforming [2, 9-12, 45-47].

With adaptive beamforming, the receiver may either simply excite the even mode of the array (where all radiating elements are excited with the same amplitude and phase) to enhance its gain at the zenith and achieve better signal-to-noise ratio, to ensure better navigation accuracy, or excite a superposition of its radiation eigenmodes [4, 69, 76], in order to acquire navigation data from satellites at different directions [9-12]. This spatial diversity empowers the receiver with the capability to compensate for the impact of multipath propagation and track satellites at elevations down to 10° [48].

Moreover, array-based receivers can estimate the direction of arrival (DoA) of possible sources of interference, such as jammers or spoofers, and use beamforming to desensitize the radiation patterns at those directions [4, 9, 38]. Such a process, usually referred to as null-steering [13, 15, 49, 50], plays a pivotal role to improve the robustness of the receiver against unwanted interferers.

2.3.2 Dual-polarized Antennas

Classical GNSS receivers use RHCP antenna to cope with the polarization of the GNSS signal. However, multipath propagation changes the polarization purity of the signals, introducing larger LHCP components at the receiver, which results in polarization mismatching, and hence power loss [7, 8, 16, 17]. This phenomenon gives rise to the use of dual-polarized antennas, to enable receiving both the RHCP and LHCP signals.

Moreover, single-polarized RHCP planar antenna arrays suffer from degraded cross-polarization discrimination at lower elevations, due to mutual coupling, as studied in detail in chapter 4. This enables the arrays to, partially, receive the LHCP components. However, their LHCP patterns show poor efficiencies. Optimal reception of the signal with minimum polarization mismatch can only be achieved by acquiring the two polarization degrees-of-freedom, using dual-polarized antennas.

Furthermore, dual-polarized antennas enhance the robustness against jamming sources [14, 18-20]. Having a linear-polarized jamming source, null-steering algorithms that steer only the RHCP patterns can help to eliminate the influence of the jamming signal if a pure RHCP receiver is used. Unfortunately, jamming signal arrive usually from low-elevations where the receiving planar antennas have notable LHCP gains, e.g., at elevations below 10°, where the LHCP radiation modes of a patch antenna array can be comparable to the RHCP ones. This allows for the LHCP components of the linear-polarized jamming signal to jam the receiver. This challenge emphasizes the need for dual-polarized antennas to empower beamforming algorithms with both polarization degrees-of-freedom. It is shown in this work that dual-polarized antennas help to enhance the robustness of the designed receiver against jamming sources by about 10 dB to 15 dB at elevation of 10°.

Additionally, the increasing mutual coupling in compact RHCP antenna array degrades the polarization purity of the higher-order radiative modes, resulting in stronger LHCP components [51, 52]. This detrimental effect decreases the polarization diversity of the antenna array. However, the impact on the receiver performance can be reduced by receiving both polarizations using dual-polarized antenna elements [48].

2.3.3 Multi-band antennas

GNSS systems provide the navigation service on several frequency bands. Receivers that operate on two or more frequency bands allow for duplicating the navigation date, which results, with proper Kalman-filtering, in improved positioning accuracy, and enhanced robustness against frequency-dependent atmospheric and multipath propagation influences [21-23].

The additional resources help also to accelerate the resolving of ambiguities, and then to speed up the receiver lock time, which can be critical for real-time applications such as mobility [39].

2.4 State of the art

While GNSS systems have been developed since a few decades, systems robust against jamming, spoofing, and multipath propagation have been under increasing focus only in the last fifteen years, to serve in applications where reliable and robust navigation data are essential, such as in safety-of-life and automotive.

The global automotive supplier Ningbo Joyson Electronic Corp states that there are four core competencies in the research & development areas of automotive industry [53]:

- Navigation & driver assistance.
- Tuner & multimedia (Infotainment).
- Connectivity
- Telematics & data services

As confirmed by the list, the development of navigation and driver-assistance systems stands as an essential item of the recent and future research fields in automotive. Hence, Tier1 companies such as Bosch, Magna, Delphi, and Continental are putting increasing effort, nowadays, on the design of new Lidar-based, radar-based and satellite-based driver-assistance systems, in addition to ultrasonic sensors, cameras, and odometry sensors [54, 55], to enable cross talk, collision avoidance, and to even fulfill the increasing interest in fully-automated driving by OEM companies such as Volkswagen, Daimler, and even non-OEM companies such as Google. Figure 2.3 shows a photo of the fully-automated google car under test, from the google self-driving car project “Waymo” [56].

While the development of advanced driver-assistance systems involves many fields of research in hardware and software, the development of satellite-based navigation systems focuses more on improving the navigation accuracy through signal processing techniques, and not through array-based receivers. One major reason for that is the trend to make all sensors in the car as compact as possible to reduce the cost and ease the integration with the numerous electronic and mechanic devices in the vehicle. The reliability of GNSS receivers is usually improved through integration with inertial measurement units (IMU) in inertial navigation systems (INS) [57, 58].

Figure 2.3: A photo of the google fully-automated car, from the google self-driving car project "Waymo" [56].

In general, while multi-band receivers are increasingly used, array-based receivers and dual-polarized receivers are still not common on the market, and therefore, services such as robustness against jamming and multipath propagation are usually not provided, which makes this area of research quite promising for exploration.

Regarding the robustness against jamming, commercial single-element GNSS receivers usually provide a JSR-tolerance of only 20 dB or less [26]. Array-based GNSS receivers, described in literature, do not usually exploit all possible degrees-of-freedom such as adaptive beamforming, frequency diversity, polarization diversity, etc. Furthermore, many receiver systems do not provide adaptive gain-control of the front-end or on-line calibration of the RF signals. Hence, they provide a JSR-tolerance between 25 dB and 60 dB depending on the used techniques [3, 6, 26-28].

This thesis and the related project "KOSERNA" are part of the research in this field. The team of the project was part of a former project "KOMPASSION", where a **single-band single-polarized** array-based anti-jamming GNSS receiver was designed and equipped

with adaptive beamforming and null-steering technique to achieve a JSR-tolerance of about 55 dB, which was increased to about 70 dB later, using front-end gain-control.

In the project “KOSERNA”, we design a **dual-band dual-polarized** array-based receiver that involves the features of “KOMPASSION” in addition to **polarization diversity, adaptive beamforming**, **front-end gain control**, and **RF gain calibration**. Results at the end of this thesis reveal that the developed system outperforms several state-of-the-art systems, with a JSR-tolerance of about 85 dB. The receiver, due to the polarization diversity, partially compensates for the multipath propagation impact, and therefore features improved performance at low elevation directions, as well, i.e., far from the direction of the main beam of the antenna pattern, where the antenna features poor performance, while the multipath propagation, on the contrary, has stronger influence.

The following chapters describe the theoretical and practical challenges towards the full design of the receiver, and end with the system performance evaluation under automotive-related scenarios. The design of the antenna array, and the enhancement of its eigenefficiencies and the cross-polarization discrimination of its radiating elements, in order to improve the receiver robustness, are the main focus of the thesis. This includes the studying of the influence of mutual coupling on polarization purity of the radiating elements, and proving the feasibility of the decoupling and matching networks not only to enhance the array eigenefficiencies, but also to improve the polarization purity of the antenna elements. It also includes proving the feasibility of both the array and polarization diversities to enhance the robustness level of the receiver, to outperform element-based receivers or array-based single-polarized ones. The thesis also involves the integration between the antenna system and the RF-IF front-end, and the role the front-end plays in defining the anti-jamming robustness level of the system. Moreover, the thesis describes all the parts of the GNSS receiver, including the digital receiver.

Chapter 3:

Design of Dual-band Dual-polarized GNSS Single Antenna Elements

3.1 GNSS antenna design

3.1.1 Application requirements

Design of the single radiating element plays a key role in the development process of GNSS receivers. This importance increases in the case of dual-band dual-polarized robust GNSS receivers, since the radiation properties of the antenna at each frequency band and at each polarization determine the diversity gain of the receiver, and hence its level of robustness. This applies for both element-based [14, 18], and array-based receivers [19, 20].

Therefore, in addition to the focus on the classical antenna design parameters such as the operation frequency, the bandwidth, the gain pattern, and the co-polarization, the design of a radiating element made for dual-polarized GNSS receivers must put a strong focus on the cross-polarization discrimination of the antenna. This focus should not only cover the high elevations, where the classical approach that focuses on the gain at these elevations results usually in a good cross-polarization discrimination (XPD), but it should also cover the low elevations, since enhancing the polarization purity of the antenna, and thus the polarization diversity of the receiver, improves its robustness against multipath propagation, and subsequently extends the coverage angle of the receiver.

However, in comparison to the classical single-band single-polarized antenna, the prerequisite of dual-band and dual-polarization functionality increases the complexity of the element design, which rises the need to find compromises between the performance demands, the physical limitations, and the challenges of manufacturing technologies.

3.1.2 Antenna type

Due to technical, manufactural, and commercial reasons, most of the recent applications that require GNSS receivers prefer compact lightweight printed-circuit-based receivers with ease of fabrication and system integration. To fulfill these requirements, antenna designers may use planar printed patch, dipole, or monopole antennas. Patch antennas, however, are preferred for GNSS systems to enable the excitation of the right hand circular polarization, either directly by truncating the patch surface, or by exciting its vertical and horizontal polarizations with 90° phase shift. Patch antennas are also preferred for their miniaturized sizes, especially if high dielectric materials were used as substrates. Moreover, patch antennas are preferred for multi-band antenna systems, since it is possible to manipulate their surfaces to excite several bands, which avoids the need for extra space to deploy several single-band antennas.

3.1.3 Design approaches

A single patch antenna operates, in the nominal case, at a single frequency band. However, dual- or multi-band patch antennas were developed since early stages. Dual-band patch antennas, in particular, can be classified according to the implementation design into two main types; the multi-layer design, where the antenna is designed using several metallic layers to resonate at every frequency [59-61], and the single layer design, where the patch surface is manipulated to change the surface current distribution in order to excite several radiation modes at different frequencies [62-65].

The dual-polarization functionality is achieved, usually, using two feeding ports to excite two different radiation modes with orthogonal polarizations. The ports feed the patches at optimized positions to provide the best possible matching level at both frequency bands, and to excite the relevant orthogonal polarizations with minor cross-polarization coupling. More details about the design are to be mentioned in the following sections.

3.2 Multi-layer patch antenna element

In this approach, the dual-band antenna is designed using two patch layers, where a small patch is stacked over a larger one, which is stacked, in turn, over a ground layer, and a dielectric material is used between the three layers, as depicted in Fig. 3.1. This structure provides two cavities, resulting in resonating at two frequency bands. The lower band can be determined, mainly, by tuning the dimensions of the larger patch, and the higher band is achieved, mainly, by tuning the smaller one. However, each of the two patches influences the operation at the two bands, and hence both must be tuned jointly to achieve the resonance at both bands.

A single port capacitive feeding is used to excite the two patches at their different frequency bands, resulting in dual-band radiation with the same linear polarization. A similar feeding port is placed along the orthogonal principal axis to excite the patches with the orthogonal linear polarization.

Eventually, a dual-band dual polarized antenna is achieved. A design of such an antenna model was accomplished by our project-partners in the Institut für Kommunikation und Navigation (IKN) at DLR, using the Rogers 3010 material [66] as the dielectric substrate.

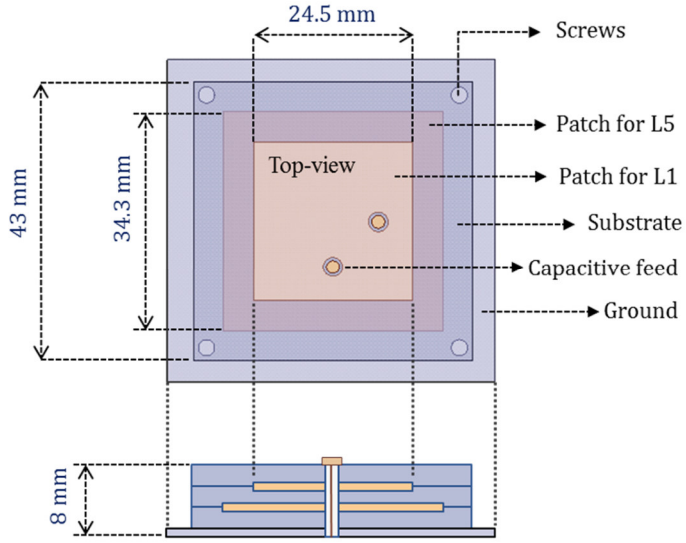

Figure 3.1: Top-view and cross-sectional view of a multi-layer dual-band dual-polarized antenna element

The single element design together with an array design are presented in detail in [66, 67], while the integration of the antenna with the front-end of a GNSS receiver is presented in [68, 69].

The antenna had a thickness of 8 mm, which was difficult to be manufactured in the available printed circuit board (PCB) manufacturing industry in Germany and Europe, where, for reasons of financial feasibility, industry focuses on establishing production lines for PCBs thinner than 5 mm. Therefore, the layers had to be printed separately, and then stacked manually in the lab. Thus, it was difficult, with such a fabrication complexity, to propose the antenna for massive production, and therefore it was decided to go for the single-layer approach.

3.3 Single-layer patch antenna element

3.3.1 Antenna design

As mentioned before, a single-layer patch antenna may resonate at two frequency bands only if its surface current distribution was modified to excite more radiation modes at different frequencies. This, equivalently, means that the antenna surface must be re-designed to provide acceptable input matching and radiation efficiencies at both frequency bands-of-interest. This can be achieved by making slots inside the patch as described in [63].

However, it was found in [63] that, due to the geometrical limitations of the slots and the patch surface, which determine the upper and lower resonance frequencies, the ratio of the two operation frequencies of a slot-loaded patch antenna cannot drop below 1.6. This design limitation creates a major challenge for GNSS receivers, where the commercial operation bands are between the GPS L5/Galileo E5a-band centered at 1176.45 MHz and the GPS L1/Galileo E1-band centered at 1575.42 MHz, which leads to a ratio of 1.34.

The 1.6 frequency ratio can be reduced using more slots in asymmetric designs [64]. However, this works only for single-polarized antennas. The need to excite two radiation modes with orthogonal polarizations and identical gain patterns forces the design to retain symmetry, and thus restricts the way how slots can be added.

In order to get rid of the limitation of adding slots, more spatial degrees-of-freedom can be brought by attaching stubs at the outer sides of the patch. This was found to help to overcome the ratio problem, without influencing the symmetry. A dual-band circularly-polarized patch antenna that uses a single square patch with four T-stubs arranged at the four edges was proposed in [65]. However, the antenna operated at frequency bands centered at 1.531 GHz and 3.050 GHz, which results in a frequency ratio of 1.9 > 1.6.

The stub-loaded antenna was re-designed in [70], to address the GPS L1- and L2-bands, centered at 1176.45 MHz and 1227.6 MHz respectively, with a frequency ratio of 1.284. However, the dual-band antenna was single-polarized with asymmetric shapes and positions of the T-stubs, in order reduce the axial ratio at the two frequencies.

The idea of stub-loaded patch antennas was successfully employed in this work, for operation at the two L1- and L5-bands, with a symmetric design that excites two orthogonal polarizations, as illustrated in Fig. 3.2. Two feeding ports were used to allow for the excitation of two orthogonal linear polarizations, namely vertical and horizontal. The positions of the two ports were selected based on electromagnetic full-wave simulations of the field distribution within the patch, such as to minimize the cross-polarization coupling.

The RHCP and LHCP polarizations were excited by feeding the two antenna ports using a quasi-lumped coupler with a 90° phase shift.

The organic laminate Rogers 3010, was used to limit the geometrical dimensions of the antenna to about 3 cm × 3 cm, attributed to its high dielectric constant of 10.2. The material was also selected for its low dissipation factor of $\tan\delta = 0.0022$, and its excellent dimensional and dielectric constant stability with temperature between -50 and 150 °C [71]. Two substrate layers of an individual thickness of 2.54 mm were stacked over each other, using a 0.1 mm adhesive layer of Rogers 4450F [72], to enhance the radiation efficiency and the bandwidth of the antenna. This results in an antenna of 5.18 mm thickness, or 5.215 mm thickness if the thickness of the metallic surfaces was counted, which is almost at the upper limit recommended for mass production by the printed circuit board industry in Europe.

Adding the adhesive material, with 3.52 permittivity, was found to reduce the equivalent permittivity of the substrate from 10.2 to around 9.8, resulting in shifting the two resonance frequencies of the antenna by about 32 MHz at the L1-band and 24 MHz at the L5-band. The antenna was retuned in the numerical full-wave simulations, to compensate for this impact. The design and the simulations were performed using the frequency solver of CST Microwave Studio [73].

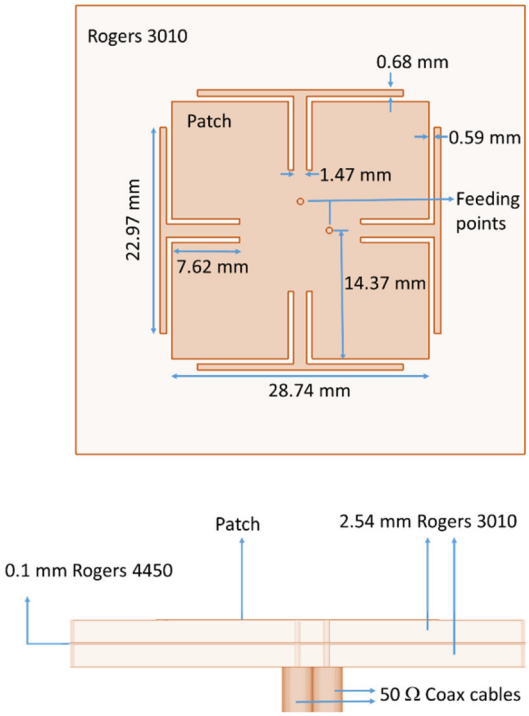

Figure 3.2: Top-view (upper panel) and side-view (lower panel) of the single-layer dual-band dual-polarized stub-loaded patch antenna element, with material composition and geometrical dimensions as shown

3.3.2 Manufacturing challenges

Numerical simulations of the stub-loaded patch antenna found that the resonance frequencies, radiation efficiencies, and polarization purity, at both bands, were strongly sensitive to the dimensions of the stubs, the dimensions of their feed lines, and the gaps between the stubs and the patch edges. Therefore, in order to reduce the influence of the fabrication tolerance of 100 μm, the design was optimized while keeping all dimensions greater than five times the fabrication tolerance, i.e., 500 μm.

The complexity of this optimization process was overcome using the CST built-in genetic algorithm, which is a global optimization method suitable for problems with large number of parameters. The algorithm searches for the global solution of the problem following the principles of the process of natural selection [74, 75]. The optimization parameters of the algorithm were the antenna dimensions, while the main targets were:

- Dual-band operation with a reflection coefficient below -10 dB at both bands.
- A bandwidth larger than 4 MHz at the L1-band and 20 MHz at the L5-band.
- Polarization purity with XPD larger than 10 dB over the entire upper sphere.
- A released gain larger than 2 dB at both bands.

First manufactured designs showed downward frequency shifts of about 30 MHz from the L1-band and L5-band, mainly because of the difference between the nominal and actual values of the dielectric constant of the Rogers 3010 substrate. The actual dielectric constant was recomputed, based on the frequency shift, and was found to be 10.8 instead of the nominal value of 10.2. The antenna was redesigned based on the new value of the dielectric constant (basically, all dimensions of the patch layer where miniaturized by the ratio $\sqrt{10.2} / \sqrt{10.8} \approx 0.97$). S-parameter measurements of the corrected design showed a very good frequency response, as seen in Fig. 3.3.

3.4 Single-layer antenna measurements

3.4.1 Frequency response

Antenna measurement results of the final design proved the antenna resonance at both bands-of-interest, with a reflection coefficient of about -15 dB at the L1-band and -12 dB at the L5-band, as depicted in Fig. 3.3. The same performance was measured for both polarizations.

Measurements of antennas from different fabrications showed very good reproducibility, with a frequency deviation of about 1.5 MHz and a maximum frequency shift of about 3 MHz. This shift is quite acceptable for GNSS application as it is still below half the bandwidth of the antenna, which is about 6 MHz at the L1-band and 25 MHz at the L5-

band. The reproducibility can be improved through more accurate manufacturing of the patch layer.

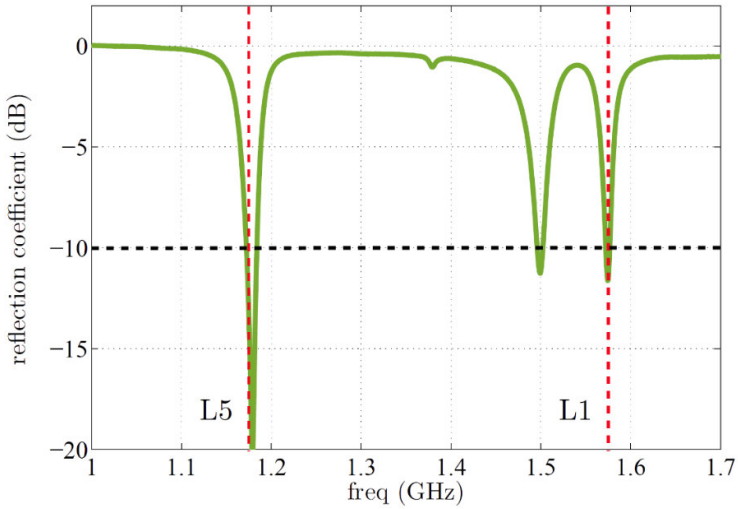

Figure 3.3: Reflection coefficient vs. frequency, measured at a single port of the dual-band dual-polarized antenna element. The other port shows similar measurements.

Due to the sophisticated geometry, simulations and measurements show that the antenna has an additional resonance at 1.5 GHz, which is not wanted by the design specifications. However, this resonance is associated with the mode TM_{22}, which is orthogonal to the dominant mode TM_{10} that resonates at the L1- and L5-bands, and therefore it has minimal effect on the receiver operation at these two bands. Moreover, this mode has a radiation pattern of two beams, with a null at zenith, which is not desired by the classical GNSS antennas, and therefore it was not feasible to retune the antenna to use this mode in a multi-band GNSS receiver. Furthermore, the mode suffers from a radiation efficiency below 10%, which makes it not practical for a multi-mode antenna system too. Therefore, this mode is to be filtered out in the GNSS receiver by the antenna matching networks, and the front-end RF filters.

3.4.2 Radiation pattern

The realized-gain patterns were measured for each polarization in the anechoic chamber. Measurements confirmed that each of the gain patterns at L1- and L5-bands has one lobe directed at zenith, as expected from theory and numerical simulations, and as depicted in the normalized θ-cuts illustrated in Fig. 3.4. The maximum measured realized gain was about 2.5 dBi at the L1-band and 4 dBi at the L5-band. The patterns were almost constant versus azimuth, with changes below 0.2 dB due to fabrication and measurement tolerances.

As noticed, the maximum measured realized gain values are far from the expected values of a single-band patch antenna (5 to 7 dBi). Small part of this limitation is due to the difficulty of achieving 50 Ω feed matching at the two closely-spaced frequency bands

simultaneously. An input impedance Z_l of about 30 Ω at the L1-band and 45 Ω and L5-band was achieved, which results in a reflection coefficient Γ of 0.25 and 0.05, or a reflection loss RL of 0.28 dB and 0.01 dB, respectively, as can be calculated from:

$$\Gamma = \frac{Z_l - Z_o}{Z_l - Z_o} \tag{3.1}$$

$$RL = -10.log_{10}(1 - \Gamma^2), \tag{3.2}$$

where the characteristic impedance $Z_o = 50\ \Omega$.

The main reason for this limitation is attributed, in fact, to the stubs, which change the surface current distribution of the original single-band patch antenna, in order to force the patch to resonate at two frequencies, resulting in a radiation efficiency smaller at each band than the original radiation efficiency of the single-band patch antenna. Electromagnetic full-wave simulations found that the designed stub-loaded patch shows a radiation efficiency 2 to 4 dB below that of the single-band patch antenna designed with the same material at either L1- or L5-bands.

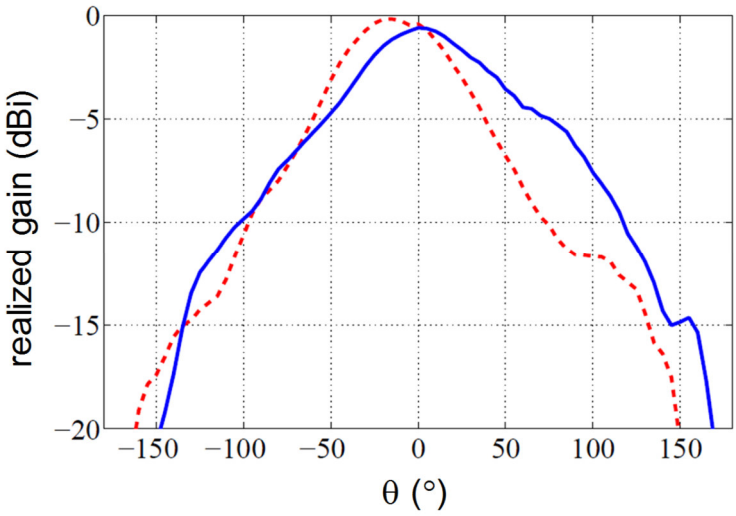

Figure 3.4: θ-cut of the measured realized-gain patterns, at zero azimuth, at a single port for the L1-band (red-dotted curve) and the L5-band (blue-solid curve). The other port shows similar measurements. The two patterns are almost constant versus azimuth, with changes below 0.2 dB.

Comparable results were also found in the case of the multi-layer dual-band antennas were a realized gain between 2 and 4 dBi was achieved.

The 3-dB beam-width amounts to about 75° at the L1-band, and to 90° at the L5-band. The 10-dB matching bandwidth extends over 4 MHz at the L1-band, and over 13 MHz at the L5-band. The bandwidth related to 3 dB below the maximum realized-gain is about 6 MHz at the L1-band and 25 MHz at the L5-band, which is quite sufficient for GNSS receivers,

were nominal bandwidths should be around 4 MHz at the L1-band and 20 MHz at the L5-band.

3.4.3 Cross-polarized coupling

Coupling between two ports describes the excitation of some energy at one port if the other port is fed. Quantitatively, it is represented by the scattering parameter S_{12}, where $|S_{12}|^2$ tells the ratio of the power received at the coupled-port No. 1 to the original power radiated by the coupling-port No. 2.

If the two ports have different polarizations, then coupling is referred to as cross-polarization coupling. In dual-polarized antennas, cross-polarization coupling reduces the polarization purity of the antenna, and hence its polarization diversity.

In the designed antenna, to reduce the coupling level between the two feeding ports P_1 and P_2, each port was positioned along the axis where the electrical field excited by the other port, between the patch surface and the ground, has zero strength. This is illustrated in Fig. 3.5, which shows a cross-section in the oxy-plane (parallel to the patch surface) of the strength of the electrical field $\vec{E}_1$ excited by the port P_1, which is placed along the oy-axis. The other port P_2 is placed along the ox-axis, where $\vec{E}_1$ has zero strength. In the same way, P_1 is placed along the oy-axis where the electrical field $\vec{E}_2$, excited by the port P_2, has zero strength. The exact positions of P_1 and P_2 were optimized along the orthogonal oy- and ox-axes, respectively, to ensure the best possible matching at both frequency bands.

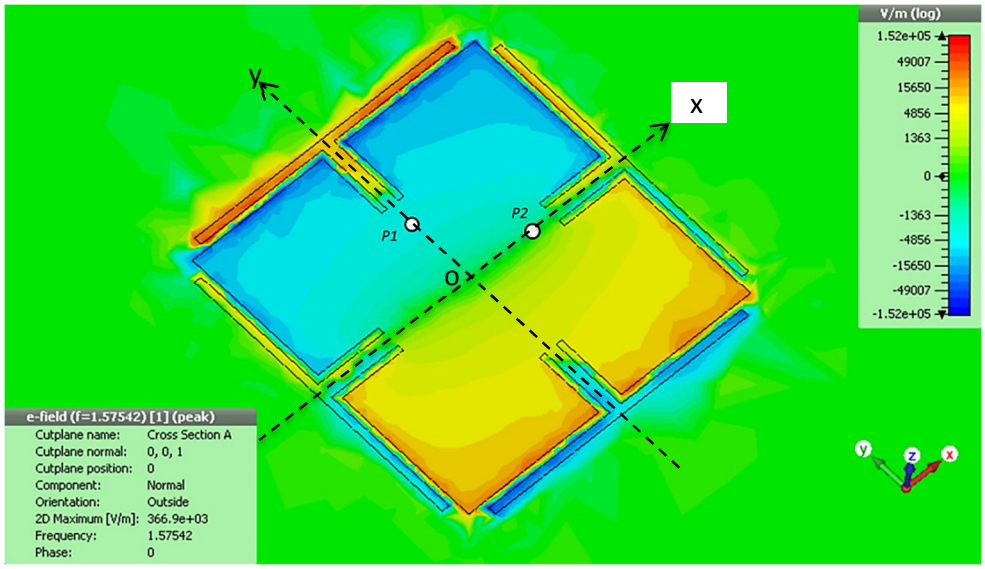

Figure 3.5: A cross section of the strength of the electrical field $\vec{E}_1$ excited by the feeding port P_1, between the patch surface and the ground. The feeding port P_2 is placed on the ox-axis, where $\vec{E}_1$ has zero strength.

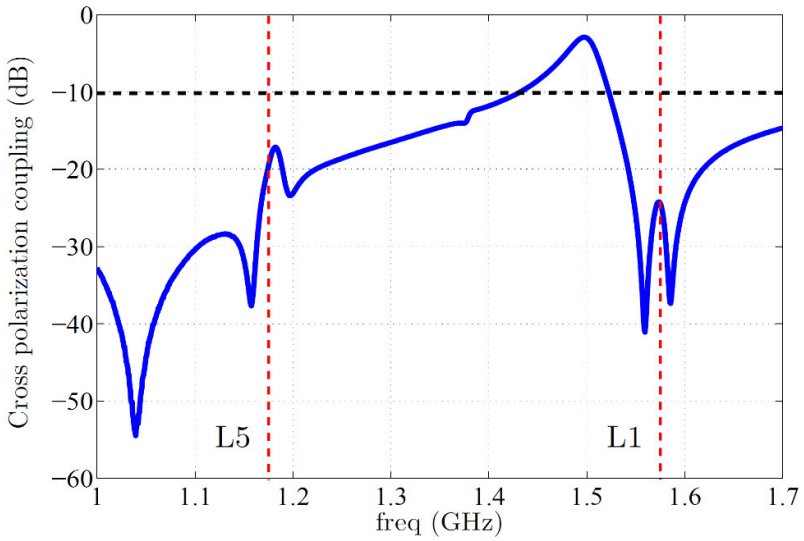

Figure 3.6: Measured cross-polarization coupling (S-parameter measurements) between the two orthogonal-polarized radiation modes exited by the feeding ports P_1 and P_2.

A cross-polarization coupling of only -17 dB at the L5-band, and -24 dB at the L1-band was achieved, as depicted in Fig. 3.6.

Even though, it tells nothing about the direction dependency, cross-polarized coupling is easy to be measured, and therefore is used as a first indication of the antenna quality regarding polarization.

3.4.4 Cross-polarization discrimination

Differently from the cross-polarization coupling, which is simply $|S_{12}|^2$ between two feeding ports of different polarizations, the cross-polarization discrimination describes the ratio between the co- and cross-polarized radiated power density of the same feeding port, as a function of direction (azimuth and elevation), and defined by:

$$XPD(\theta,\varphi) = \frac{\left|\vec{E}_{co}(r,\theta,\varphi)\right|^2}{\left|\vec{E}_{cross}(r,\theta,\varphi)\right|^2}, \tag{3.3}$$

where $\vec{E}_{co}(r,\theta,\varphi)$ and $\vec{E}_{cross}(r,\theta,\varphi)$ are the co- and cross-polarized electrical fields, respectively, r stands for the distance from the antenna, θ stands for the co-elevation, and φ for azimuth.

The designed antenna element features a cross-polarization discrimination of better than 15 dB for the two bands over the entire upper half-space, at all azimuth angles. Fig. 3.7 shows a θ-cut of the XPD pattern at the worst case, the L5-band, based on numerical simulations.

The XPD for L1-band is 2 to 4 dB larger. This high discrimination level confirms the orthogonality between the two excited polarizations, and hence the suitability of the antenna for dual-polarized applications.

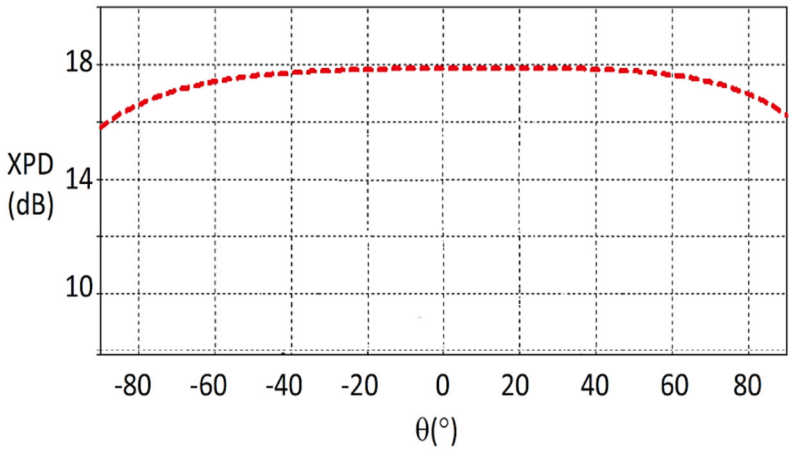

Figure 3.7: θ-cut of the cross-polarization discrimination of the single element, at zero azimuth, at the L5-band, based on numerical simulations.

3.5 Summary

A dual-band dual-polarized patch antenna was designed and fabricated for satellite navigation systems. The design employed a stub-loaded single-layer patch design. S-parameter and far field measurements confirmed the proper operation of the antenna at both bands-of-interest. The suitability of the design for dual-polarized applications was proven with a cross-polarization discrimination of better than 15 dB over the entire upper half-space, and a cross-polarization coupling below -17 dB at both band. In conclusion, the design was proven suitable for a miniaturized dual-band dual-polarized radiating element for robust and reliable GNSS receivers. The antenna design and the relevant measurement results were published in [51].

Chapter 4:

Compact Antenna Arrays, and Impact of Mutual Coupling on Polarization Purity

4.1 Motivation for, and definition of, compact antenna arrays

As mentioned in chapter 2, satellite navigation receiver that features robustness against jamming and spoofing must use arrays of radiating elements to exploit their beamforming capability to null directions of the interfere sources.

However, robust satellite navigation receivers intended to be used for applications such as highly-automated vehicles, unmanned quadcopters, or secure smartphones, are mostly installed in platforms where there is limited space for the receiver, due to the installation of many antenna systems and sensors to serve various kinds of applications such as radar-based safety systems, ultrasonic sensors, cameras, infotainment antennas, WIFI antennas, etc.

This space limitation gives rise to need to use receiver solutions that depend on compact antenna arrays integrated with compact RF circuits. While this approach is affordable in the above-mentioned applications, for the sake of complexity and cost, it is still not common in personal satellite navigation receivers, commercial smartphones, or smart hand-watches.

Electrically, an antenna array is considered compact if the electrical distance between the radiating elements is smaller than half the free-space wavelength at the operation frequency. For such antenna arrays, a strong mutual-element coupling arises between the radiating elements, resulting in drawbacks such as:

- Reduced radiation eigenefficiencies, and hence signal-to-noise ratio [76-79].
- Decreased spatial diversity [80].

Smaller direction-finding resolution [81-84].
- Shifted frequency responses, narrower frequency bandwidths, and increased sensitivity to dissipative losses [85]
- Disturbed polarization purity [52, 51], etc.

This chapter covers the topic of mutual coupling in compact antenna arrays, and its influence on the array radiation parameters, with special focus on the impact on polarization purity. The study focuses on patch antenna arrays, the common antenna type for GNSS receivers.

4.2 Mutual-element coupling in patch antenna arrays

4.2.1 Sources of mutual coupling

Mutual coupling between radiating elements has been studied in literature since more than three decades [86-89]. Coupling can be excited by various sources depending on the antenna type, and the array structure. The dominant sources of coupling in patch antenna arrays are mainly classified into three types, surface-wave coupling, nearfield coupling, and far field coupling, as illustrated in Fig. 4.1.

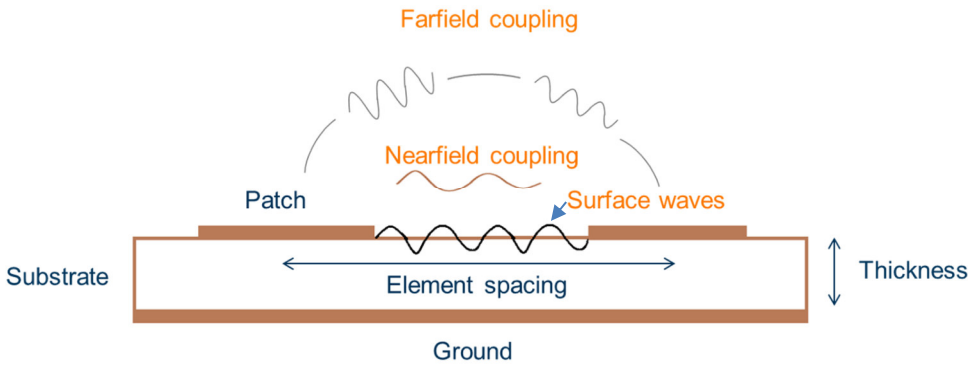

Figure 4.1: Dominating sources of mutual coupling in compact patch antenna array

Surface-wave coupling:

In this type of coupling, surface waves are guided by the substrate and the ground plane, and travel between the radiating elements with a radiation variation of $1/\sqrt{r}$, where r is the element spacing [89-93].

Due to its sources, this coupling is more pronounced for substrates of dielectric constants much higher than that of the air. It also increases with the effective electrical thickness h/λ_g, where h is the substrate thicknesses, $\lambda_g = \lambda_0/\sqrt{\epsilon_r}$ is the effective

wavelength, λ_0 is the free-space wavelength, and ϵ_r is the dielectric constant of the substrate. Therefore, literature usually neglects the surface-wave coupling for very thin patch antennas [87, 91]. Authors in [91], for example, suggest that this source of coupling becomes notable when the effective electrical thickness reaches or exceeds 5%.

Regarding the proposed GNSS receiver, as described in chapter 3, the attitude towards miniaturized antenna elements demands an antenna design that has a high dielectric constant of 10.8 to allow for small patch dimensions, and relatively a large substrate thickness of 5.18 mm, which makes an effective electrical thickness of 11%, to improve the radiation efficiency. Therefore, the influence of this source of coupling cannot be ignored for these antennas.

Nearfield coupling:

This coupling is caused by the reactive energy stored in nearfield between the radiating antenna elements. In some literature, as in [90], it is referred to, as a higher-order wave coupling. The field of this type of coupling decays by $1/r^2$ or faster outside the radiating element. I.e., it diminishes by 12 dB or higher when the element distance is doubled [94]. Nevertheless, this is still not enough to ignore this source of coupling for compact arrays, where element distances are below half the free-space wavelength. This source of coupling is relatively strong in the antenna array designed in this work, since the element distance is about one quarter of the free-space wavelength at the L1-band, and even one fifth of the free-space wavelength at the L5-band.

Far field coupling:

Since the coupling and the coupled antennas have two metallic surfaces with different potentials, an electrical field will be excited between them as well. This field will be responsible for carrying some energy between the antennas. Since the field will also radiate in the far field, this type of coupling is referred to as far field coupling by some literature [90, 94, 95], even though the antennas are in the nearfield of each other. Fields of this source of coupling propagate in the free space with a radiation variation of $1/r$ [90, 94]. This means that they diminish by only 6 dB when the element distance is doubled. Hence, as with the other sources of coupling, far field coupling also cannot be ignored for compact antenna arrays.

Other sources:

Coupling may happen due to other sources such as leaky waves. However, these waves diminish exponentially, and thus their impact is negligible, compared to the other sources.

Summary

As mentioned, the different sources of mutual coupling have different radial variations. While leaky waves diminish exponentially with a radiation variation of e^{-r}, nearfield coupling diminishes at a slower rate with radiation variation of $1/r^2$, far field coupling

diminishes with a radiation variation of $1/r$, and surface-wave coupling diminishes with a radiation variation of only $1/\sqrt{r}$.

Therefore, for all sources of coupling, the strength of the coupled fields depends on the distance between the radiating elements, in addition to other parameters. Because of its smaller radial variation, surface wave coupling is more dominant for large element distances, where nearfield and far field coupling fields diminish faster. However, this does not apply to compact antenna arrays where, due to the small element distance, nearfield and far field coupling fields are comparable to, or can be even stronger than, the surface-wave fields.

4.2.2 Influence of mutual coupling on radiation eigenefficiencies

The impact of mutual coupling on radiation efficiencies of antenna elements in compact antenna arrays has been intensively studied in literature [3, 49, 67, 69, 76, 80, 96, 97]. A comprehensive numerical analysis, described in [76], confirmed that mutual coupling increases for smaller element spacing values, as well as for larger number of radiating elements in the array. Consequently, it was shown by [77, 79, 80, 98, 99], that mutual coupling reduces the eigenefficiencies of the array, especially for the higher-order eigenmodes. This, eventually, decreases the beamforming degrees-of-freedom, and thus limits the diversity gain of the antenna.

However, literature focused on the influence of mutual coupling on the co-polarized radiation efficiency, considering mostly single-polarized antenna applications. The influence of mutual coupling on cross-polarized radiating fields, and hence on polarization purity of radiating elements had been rarely under investigation.

The following section describes how polarization purity changes in compact patch antenna arrays. The study starts by explaining how the single patch antenna element radiates, with focus on how cross-polarization is excited. The analysis expands to describe how mutual coupling arises in compact arrays, and how it affects the co- and cross-polarized radiating fields. Subsequently, it describes how coupling affects polarization purity of the radiating elements. The cross-polarization discrimination XPD is used as a figure-of-merit for determining the polarization purity.

4.3 Polarization purity of the single patch antenna element

4.3.1 Modelling of the problem

The distribution of the electrical field in a patch antenna depends on many parameters so that the extraction of its exact analytical description becomes too difficult. However, following the approach of the perturbation theory, the problem can be reformulated by

introducing some approximations, and thus, solutions that match with real measurements can be achieved [100].

Two widely accepted models, used to describe how patch antennas work are the transmission-line model, and the cavity model [90]. While both models give good physical insights, the cavity model provides insight into the radiation pattern, which is found to be comparable to the measured patterns, and therefore it is commonly used in literature.

In the cavity model, the patch antenna is modeled as a cavity bound by two electric conductors, which are the patch metallic surface above the substrate and the ground below it, and surrounded by four perfect magnetic walls, which represent the sides of the dielectric material [90].

The cavity model is also used to describe how mutual coupling arises [87, 88, 101 - 103], even though Balanis in [90] sees that it is difficult for both the cavity and the transmission line models to model coupling. This thesis uses the cavity model as well, as a basis for describing how cross-polarization radiation rises.

4.3.2 Fundamental mode in rectangular patch antennas

As described in detail in [90], applying a signal, resonating at the operation frequency, at the matched feeding point of a rectangular patch antenna, results in a charge distribution at both the bottom surface of the patch and the upper surface of the ground, as illustrated in Fig. 4.2.

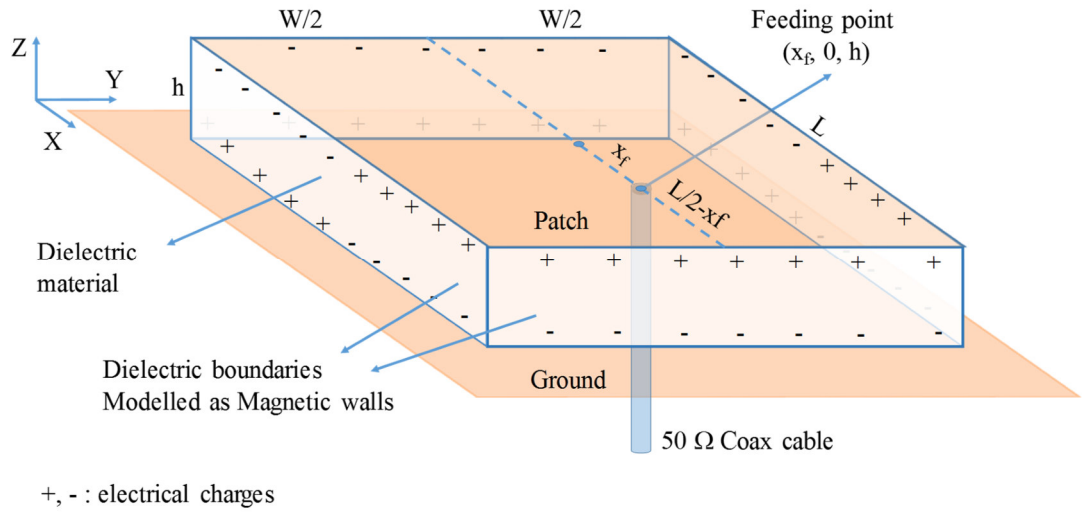

Figure 4.2. A simplified illustration for a snapshot of the charge distribution on the electric conducting surfaces, resulting from exciting the patch antenna at the matching feeding point, with a signal at the relevant operation frequency.

According to the Gauss' Law which describes how the electric field behaves around electric charges:

$$\nabla.\vec{E} = \frac{\rho_V}{\varepsilon_r} \tag{4.1}$$

where ∇ is the divergence operator, $\vec{E}$ is the electrical field, ρ_V is the electric charge density, and ε_r is the permittivity of the medium, an attractive mechanism rises between the opposite charges of the two surfaces, and a repulsive mechanism rises between the similar charges of each surface, which pushes them to the opposite edges of the surface. Considering a substrate thickness that is too small compared to the patch width, the electrical fields that arise between the opposite charges become strong enough to keep the charge concentration higher at the bottom side of the patch and the upper side of the ground. These electrical fields, directed along the z-direction, dominate within the cavity, and form the TM^z modes.

Solving the homogeneous wave equation of the vector potential by applying the boundary conditions, it is found in [90] that the vector potential within the cavity can be written as:

$$A_z = A_{mnp}\cos(K_x x)\cos(K_y y)\cos(K_z z), \tag{4.2}$$

where A_{mnp} is the amplitude coefficient of the mode TM^z_{mnp}, and the wavenumbers K_x, K_y, and K_z satisfy:

$$K_x = \frac{2\pi}{\lambda_g} = \frac{m\pi}{L}, m = 0, 1, 2, \ldots \tag{4.3}$$

$$K_y = \frac{2\pi}{\lambda_g} = \frac{n\pi}{W}, n = 0, 1, 2, \ldots \tag{4.4}$$

$$K_z = \frac{2\pi}{\lambda_g} = \frac{p\pi}{h}, p = 0, 1, 2, \ldots \tag{4.5}$$

where λ_g is the effective wavelength, L, W are the length and width of the patch, respectively, and h is the height of the substrate.

Hence, a mode TM_{mnp} can be excited within the cavity if its dimensions L, W, h are equal to half the effective wavelength multiplied by the integer numbers m, n, and p, respectively.

Following the configuration presented in Fig. 4.2, due to the half-wavelength patch antenna, the electrical field between the patch and the ground forms sinusoidal standing waves along the x-direction, with m=1, while it stays constant along the y- and z-directions. Therefore, it forms the radiation mode $TM^z_{mnp} = TM^z_{100}$, which is illustrated in Fig. 4.3.

4.3.3 Sources of cross-polarization in the single patch antenna element

The dominant TM^z_{100} mode results in a radiated electrical field, with a linear polarization, along the x-direction, in the far field. This linear polarization is referred to as the co-

polarized radiating field. However, due to various sources, orthogonal electrical field, usually with smaller strength, is also radiated. This field is referred to as the cross-polarized field. The following study will find the possible sources for the cross-polarized radiation.

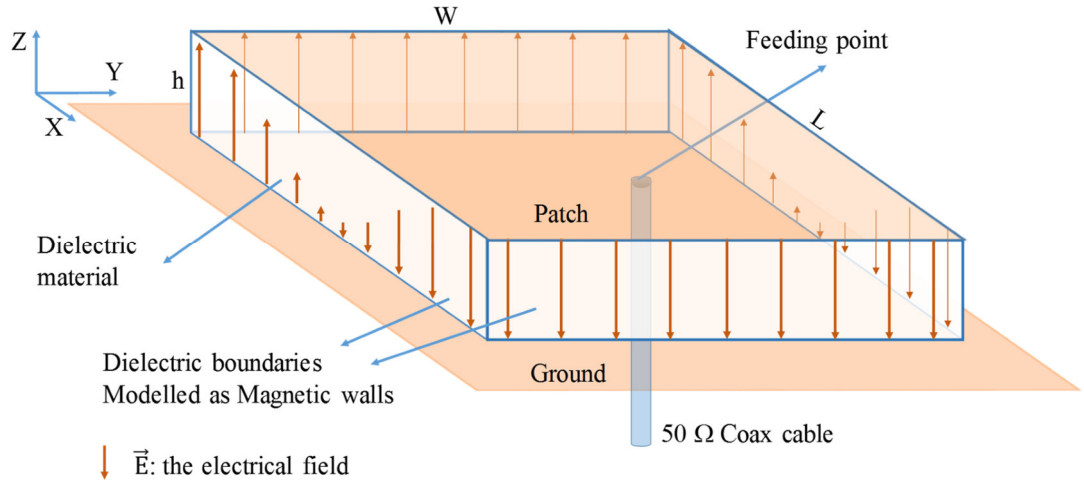

Figure 4.3: Electrical field mode TM^{z}_{100}, for rectangular microstrip patch antenna. The field between the patch and the ground forms a sinusoidal standing wave along the x-direction, while it stays constant along the y- and z-directions

A- Contribution of the dominant radiation mode

As mentioned, in the classical case where $L > W \gg h$, the dominant mode in the patch antenna is TM^{z}_{100}. This mode results in the charge distribution shown in Fig. 4.2. Subsequently, an electrical field will be excited between the edges of the patch and the ground. Top-view of the patch antenna with x- and y-components of the fringing fields in the nearfield is illustrated in Fig. 4.4. Fields here are computed on an xy-plane at λ/50 distance from the antenna surface.

In this case, since the charges along the opposite short edges of the patch are 180° out-of-phase, due to the $\lambda_g/2$ length of the patch, the x-components of the fringing fields excited between the ground and the short edges share the same phase, and thus add constructively, resulting, in the far field, in a radiating electrical field with linear polarization along the x-direction, and maximum strength along the z-direction, i.e., resulting in the classical single-beam co-polarized electrical field radiated by classic patch antennas. Nearfield distribution of this field is depicted in Fig. 4.5, which shows the two lobes of maximum strength along the two short edges.

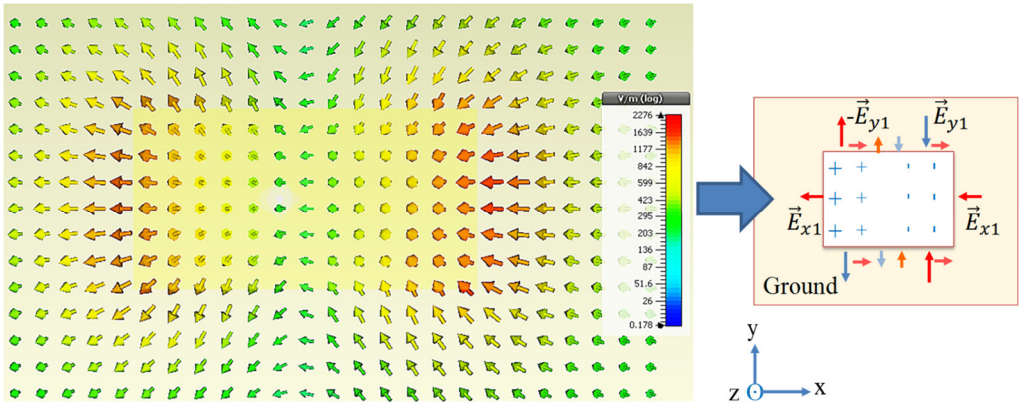

Figure 4.4: (Left): top-view of the fringing electrical fields related to the TM^{z}_{100} mode, in the nearfield, of a linear-polarized rectangular patch antenna. (Right): simplified illustration of the electrical field components for further analysis. The length of the arrow represents its magnitude.

Most literature assume that the antenna excites a pure co-polarization, while it is supposed that the unwanted cross-polarized electrical field exited along the y-direction, between the long edges and the ground, cancel each other due to the opposite phases. However, this is not fully true. These y-components do cancel each other at the yz- and xz-planes that cross the patch center, where the components will have the same strength and opposite phases, but they do not cancel each other along the planes that cross the center to the four corners of the patch, which gives rise to a cross-polarized electrical nearfield, with four lobes of maximum strength directed at the odd multiples of 45°, as depicted in Fig. 4.6.

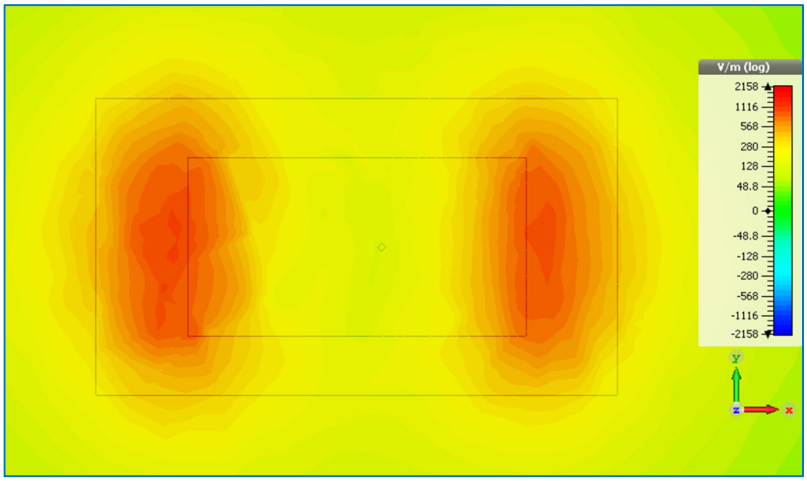

Figure 4.5: Top-view of the co-polarized electrical field strength related to the TM^{z}_{100} mode, of a linear-polarized rectangular patch antenna.

As shown in Fig. 4.6, the four lobes of the cross-polarized electrical nearfield are out-of-phase, resulting in a destructive superposition along the principal planes of the patch, and

accordingly in a far field radiation pattern of four beams tilted away from the norm-direction towards low elevations, as illustrated in Fig. 4.9.

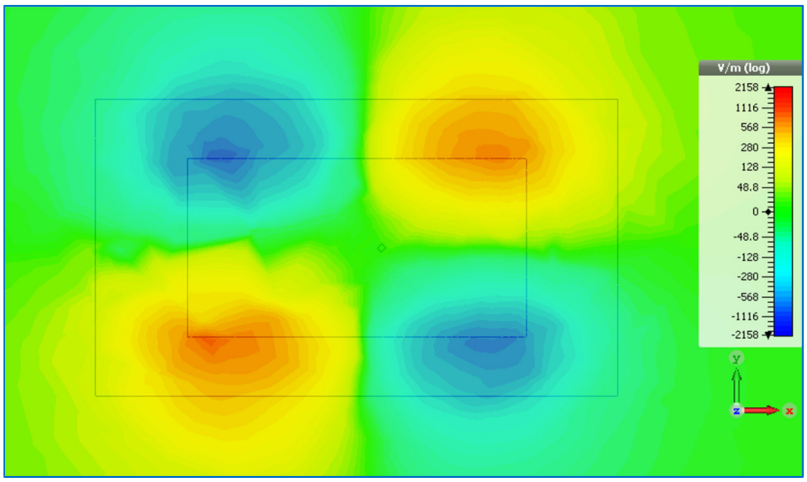

Figure 4.6: Top-view of the strength of the cross-polarized component of the electrical nearfield that relates to the TM^{z}_{100} mode, of a linear-polarized rectangular patch antenna.

This impact on the surface current distribution, which is a mere consequence of the electrical field distribution, is illustrated in Fig. 4.7. The charge distribution shown in Fig. 4.2, which is related to the dominant TM^{z}_{100} mode, resonates at the operation frequency, giving rise to the x-component currents that flow along the long edges of the patch with the same direction, as illustrated in Fig. 4.7 and Fig. 4.8 (top panel). These x-components of the current are a consequence of the co-polarized electrical field presented in Fig. 4.5.

On the other hand, the surface current turns with the corners giving rise to smaller y-components along the short edges, with opposite directions. These currents are out-of-phase at the opposite sides of the principal planes, and hence they cancel each other, which results in cancelling the cross-polarized fields at these planes. However, the currents do not cancel each other at the four corners, giving rise to the y-component of the surface current distribution shown in Fig. 4.7, and more explicitly in Fig. 4.8 (bottom panel). The y-components are a consequence of the cross-polarized electrical field shown in Fig. 4.6.

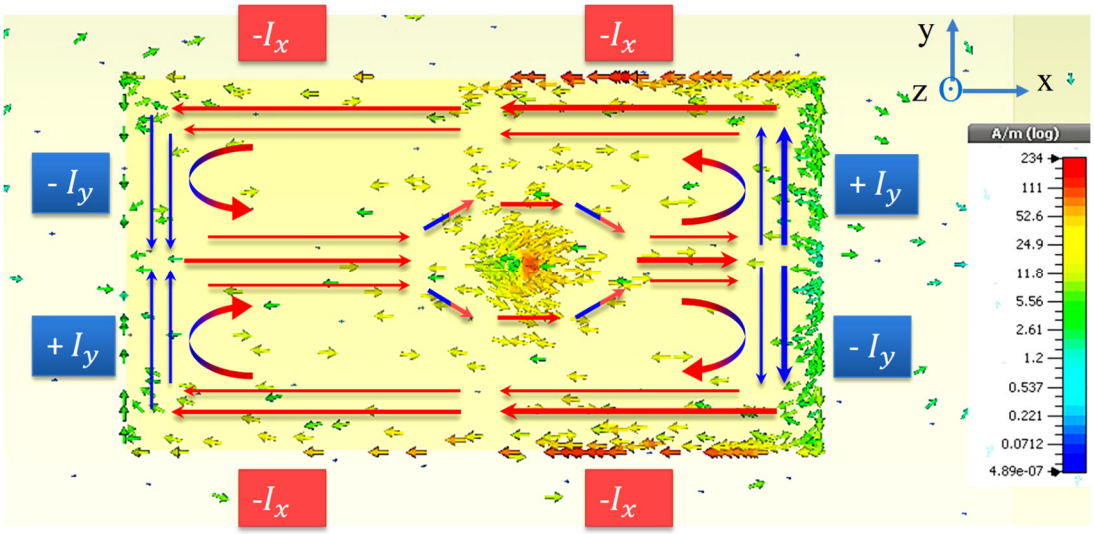

Figure 4.7: Linear-polarized rectangular patch antenna, with an illustration of the surface current related to the TM^{z}_{100} mode, as extracted by electromagnetic full-wave simulations in CST microwave studio. The x- and y-components of the current are highlighted with red- and blue-colored arrows, respectively. The direction of each arrow represents the current flow direction. The arrows with larger widths represent larger linear current densities (in A/m).

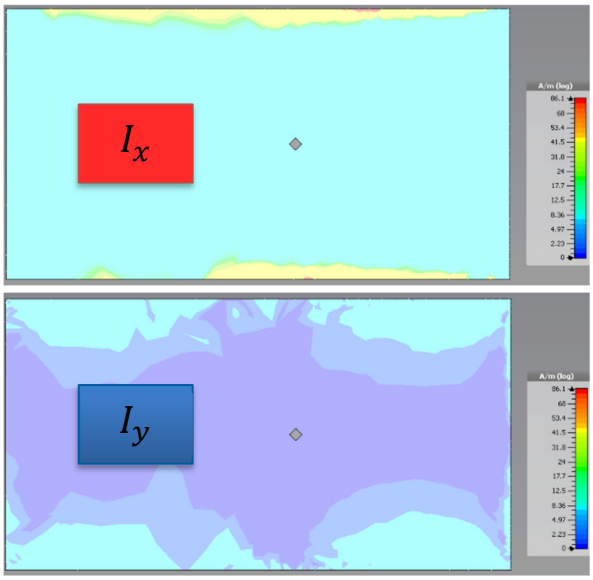

Figure 4.8: x-component (top) and y-component (bottom) of the surface current distribution, at the surface of a linear-polarized rectangular patch antenna.

Special case of circular patch antennas:

It is worth to mention that the cross-polarization is not caused due to the corners of the rectangular patch, but to y-components of the current. I.e., it is not enough to remove the corners to eliminate the cross-polarization, such as in circular patch antennas. It is needed to prevent the rise of the y-components of the current, which cannot be accomplished 100% in a 2-D surface where part of the current will always flow in x- and y-directions. A zero cross-polarization level can only be achieved using ideal 1-D antennas where the electrons cannot find a y-direction to flow along. However, it is possible to optimize the 2-D antenna to reduce its cross-polarization efficiency, as discussed in section 4.4.

Cross-polarization discrimination:

The strong cross-polarized field along the corners, i.e., along the azimuths of odd multiples of 45°, reduces the cross-polarization discrimination of the antenna at these directions. Accordingly, the resulting XPD pattern has smaller values at azimuths of odd multiples of 45° and maximum values at azimuths of even multiples of 45°. This behavior is illustrated in Fig. 4.9, which shows a φ-cut of the co- and cross-polarized gain patterns of a linear-polarized square patch antenna, together with the resulting cross-polarization discrimination.

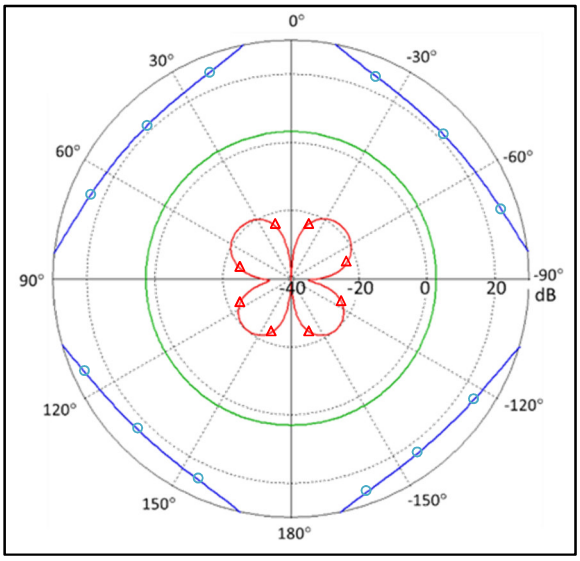

Figure 4.9: φ-cut at θ=45° of the co-polarized gain pattern (green curve), the cross-polarized gain pattern (red-triangles curve), and the XPD (blue-circles curve), of a linear polarized square patch antenna

On the other hand, a θ-cut of the co- and cross-polarized gain patterns of the linear-polarized rectangular patch antenna, with the resulting XPD, is presented in Fig. 4.10.

Figure 4.10 shows the classical co-polarized gain pattern of the linear-polarized rectangular patch antenna with its main-beam directed at zenith. The depicted θ-cut of the cross-polarized gain pattern shows two of the four beams seen in Fig. 4.9, with a null at zenith. Eventually, the figure shows the cross-polarization discrimination with its greatest value at the zenith, and its smallest values at zero elevation.

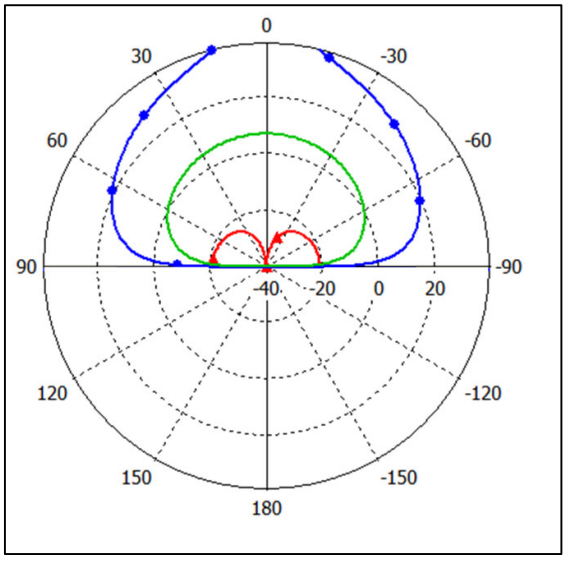

Figure 4.10: θ-cut at φ=90° of the co-polarized gain pattern (green curve), the cross-polarized gain pattern (red-triangles curve), and the XPD (blue-circles curve), of a linear-polarized rectangular patch antenna

B- Contribution of the higher-order modes:

The resonance frequency of the dominant mode TM^{z}_{100} can be calculated from:

$$f_{100} = \frac{c}{\lambda_0} = \frac{c}{\lambda_g\sqrt{\epsilon_r}} = \frac{c}{2L\sqrt{\epsilon_r}}, \tag{4.6}$$

where c is the speed of light in the free space.

Given a patch antenna with $W > L/2$, which is a widely existing case, the second-order mode TM^{z}_{010}, where the electrical field is constant along the ox-axis and forms sinusoidal standing waves along the oy-axis, will also be excited according to the conditions explained in section 4.3.2. This mode is in depicted in Fig. 4.11, and its resonance frequency f_{010} can be calculated from:

$$f_{010} = \frac{c}{2W\sqrt{\epsilon_r}} \tag{4.7}$$

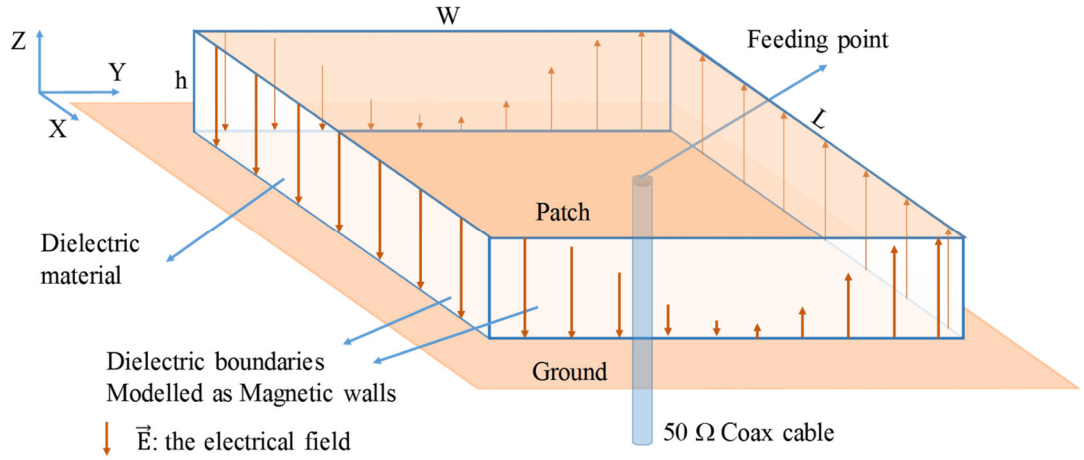

Figure 4.11: The second-order mode TM^{z}_{010}, in a rectangular microstrip patch antenna, where its electrical field is constant along the ox-axis and forms sinusoidal standing waves along the oy-axis.

Hence, the ratio between the two resonance frequencies of the two modes TM^{z}_{100} and TM^{z}_{010} is:

$$\frac{f_{100}}{f_{010}} = \frac{W}{L} \tag{4.8}$$

This mode results in a radiating field along the y-direction, and hence it forms a second source for cross-polarized radiation. However, different cases must be considered here:

1- For rectangular patch antennas: TM^{z}_{010} reaches its maximum radiation efficiency at its resonance frequency f_{010}, which is much higher than the nominal operation frequency f_{100}. TM^{z}_{010} has smaller radiation efficiency at f_{100}.
2- As the ratio W/L gets closer to 1, the second frequency f_{010} gets closer to f_{100}, and hence the cross-polarized mode gets a higher radiation efficiency.
3- When the patch becomes square, the two modes resonate at the same frequency with the same radiation efficiency, but with orthogonal polarizations, which means that the square patch antenna will have two orthogonal polarizations with the same efficiency, even though it has only one feeding port. In fact, this result is true according to the cavity model, as this model does not consider the influence of the position of the feeding point, or in other words, it ignores the reflection efficiency for each mode, and assumes a fully matched patch antenna [90].
4- However, due to the position of the feeding point, TM^{z}_{010} is not matched, and consequently it radiates with smaller efficiency.

As a conclusion, this analysis shows that square patch antennas excite cross-polarized TM^{z}_{010} modes with radiation efficiencies higher than those of rectangular patches. However, for both types, the total efficiency is smaller than the total efficiency of the co-polarized modes, due to the smaller reflection efficiency. The following paragraph studies the reflection efficiency of the TM^{z}_{010} mode.

Further higher-order modes resonate at frequencies much higher than the operation frequency, and thus they have minor efficiencies at it. Therefore, the study will focus only on the first two modes TM^{z}_{100} and TM^{z}_{010}.

Approximated reflection efficiency for TM^{z}_{010}:

Considering feed techniques that use coaxial probes, microstrip lines, or capacitive coupling, a matched rectangular or square patch antenna has a feeding point shifted from the center along either x- or y-direction to provide a 50 Ω matching for the dominant mode, which would eventually excite a radiating field polarized along the same x- or y-direction. Figure 4.2, for example shows a coaxial feeding point shifted along x-direction to match the TM^{z}_{100} mode, and subsequently to result in a relatively strong co-polarized radiation along x-direction and week cross-polarized radiating field along y-direction, as discussed before. In the case of perfect matching, TM^{z}_{100} will radiate with a reflection efficiency of 1 and a total efficiency that equals its radiation efficiency.

In contrast, the orthogonal mode TM^{z}_{010}, responsible mainly for a cross-polarized radiation along y-direction, will not be matched, and therefore it will radiate with a smaller total efficiency produced by multiplying its radiation efficiency by its reflection efficiency.

Having TM^{z}_{100} perfectly matched, with the feeding point placed at coordinates (x = x_f, y = 0, z = h), as presented in Fig. 4.2, the reflection efficiency for TM^{z}_{010} is calculated as following:

The Thevenin equivalent circuit of a single-port antenna is shown in Fig. 4.12, where V_{in} is the input voltage, R_s is the output resistance of the input voltage source, Z_o is the characteristic impedance of the feeding line, Z_{load} is the input impedance of the antenna, V_{av} is the voltage available at the input of the antenna, and S_{11} is input reflection coefficient of the antenna.

The reflection efficiency is defined by:

$$e_r = 1 - |S_{11}|^2 = 1 - \left|\frac{Z_{load} - Z_o}{Z_{load} + Z_o}\right|^2, \tag{4.9}$$

which means that the reflection efficiency is a function of only Z_{load}, assuming Z_o already known (e.g., 50 Ω).

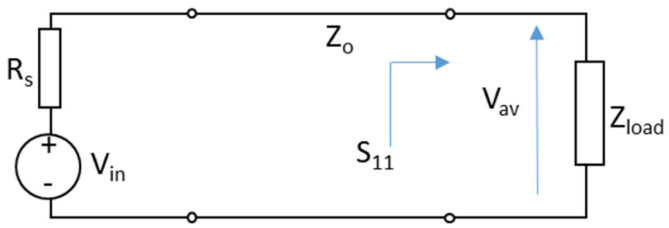

Figure 4.12: The Thevenin equivalent circuit of a single-port antenna

Having the antenna perfectly matched for the mode TM^z_{100}, means that the reflection coefficient satisfies $S_{11} = 0$, and:

$$Z_{load.\,TM^z_{100}}(x = x_f) = Z_o \tag{4.10}$$

For the mode TM^z_{010}, the feeding point is exactly at the center, which means that:

$$Z_{load.\,TM^z_{010}}(y = 0) = 0\,\Omega \tag{4.11}$$

This leads to a reflection efficiency of:

$$e_r = 1 - \left|\frac{0 - Z_o}{0 + Z_o}\right|^2 = 0 \tag{4.12}$$

This result means that the accepted power for the second mode TM^z_{010} is zero, and hence the mode is not excited.

However, this result applies only to a zero-dimension feeding points, which does not exist. Physical feeding points have dimensions, no matter if they are coaxial cables, microstrip lines, capacitive feeds, or other types.

Balanis found in [90] that an input impedance at a position $0 < y_1 < W$ of a patch antenna is real value, and that its relation to another input impedance at a position $0 < y_0 < W$ is:

$$\frac{R_{load}(y = y_1)}{R_{load}(y = y_0)} = \frac{cos^2\left(\frac{\pi}{W}\left(\frac{W}{2} - y_{1)}\right)\right.}{cos^2(\frac{\pi}{W}(\frac{W}{2} - y_0))} = \frac{sin^2(\frac{\pi}{W}y_{1)})}{sin^2(\frac{\pi}{W}y_0))} \tag{4.13}$$

Now, considering $y_0 = y_f$ as the position of the matched feeding point results in:

$$R_{load}(y = y_1) = 50\frac{sin^2\left(\frac{\pi}{W}y_1\right)}{sin^2\left(\frac{\pi}{W}y_f\right)} \tag{4.14}$$

To have a practical example, a patch antenna designed for 1.57542 GHz with 28.4 mm x 15 mm area is considered. The matched feed point for this antenna is at $x_0 = 2.1\,mm$. Feeding is provided through a coaxial cable with an inner diameter of $d_i = 0.7\,mm$. This results in a feed point not exactly at (y = 0) but at y = 0.35 mm (feeding is provided at the

skin of the inner). The skin-depth is ignored as it is too small compared to the inner (less than 2 μm for L-band in copper). This results in an input impedance of:

$$R_{load}(y = 0{,}35mm) = R_{load}(y = y_0)\frac{sin^2\left(\frac{\pi}{W}y_{1)}\right)}{sin^2(\frac{\pi}{W}y_0))} = 5\,\Omega$$

This impedance yields a reflection efficiency of

$$e_r = 1 - \left|\frac{5-50}{5+50}\right|^2 = 0{,}33\ (\text{or } 33\ \%.)$$

This poor efficiency tells how the size of the coaxial cable affects the efficiency of the modes, and stresses the need for compact coaxial cables to feed compact antennas.

However, to be more precise, two different cases must be considered here:

1- The radiation efficiency of the TM^z_{010} mode for the mentioned rectangular patch antennas example is less than 10% at the operation frequency, which results in a total efficiency less than 3.3%, which fortunately reduces the need for the compact coaxial cables for rectangular patch antennas.

2- The problem arises for square patch antennas, which is the case of classical GNSS antennas, where the TM^z_{010} mode has a radiation efficiency that equals the one of the co-polarized mode. Here, the total efficiency of the cross-polarized radiating field will be 33% of the efficiency of the co-polarized field. As suggested before, compact coaxial cables should be considered for these antennas to achieve good cross-polarization discrimination.

Summary:

Besides the co-polarized mode TM^z_{100} that is excited in a patch antenna at the operation frequency f_{100}, other modes TM^z_{mnp} can be excited at their respective frequencies f_{mnp}, with smaller radiation efficiencies at the operation frequency. Matching the first mode leads to smaller reflection efficiencies of the other modes, and hence to smaller total efficiency.

Dimensions of the feeding ports may increase the reflection efficiency of the cross-polarized modes, and hence the total efficiency. This has stronger impact in the case of square patch antennas, such as in classical GNSS antennas, where the first cross-polarized mode has a radiation efficiency that equals the radiation efficiency of the co-polarized mode.

These simplified approximations apply only for regular square or rectangular patch antennas, while they may differ for patch antennas with slits or stubs, where numerical solutions are usually used to determine the cross-polarization efficiency.

4.4 Optimization of polarization purity of GNSS patch antennas

4.4.1 Motivation

The proper design of the single radiating element is a critical step when it is proposed to serve in robust satellite navigation receivers, where the polarization purity is essential not only for the reception at high elevations, but also for interference cancellation, and for the compensation for multipath propagation at low elevations.

The classical design approaches of GNSS patch antennas usually result in a maximized co-polarized gain at the zenith, which eventually results in a good XPD at that direction. However, this does not always give a good XPD at the other directions. Therefore, in addition to the focus on the classical antenna parameters such as the operation frequency, the bandwidth, the maximum gain, the beamwidth, and the co-polarization pattern, the design of the single antenna element must put a strong focus on the XPD pattern of the antenna; especially at directions of strong multipath propagation impact, such as at low elevations, as discussed in this section.

Even though the XPD can be enhanced at some directions using antenna arrays, especially with decoupling and matching networks, the following example underlines the importance of improving the XPD at the level of the antenna element itself. The example shows that the XPD enhancement that can be achieved by improving the design of the single antenna element can be significantly larger than the enhancement that can be achieved by using more radiating elements in an array-based system to enhance the co-polarized gain of its even mode, and eventually its XPD, which gives less than 3dB gain for doubling the number of elements, and hence improves the XPD by less than 3 dB.

This becomes more serious in compact antenna arrays, where XPD patterns show deficient performance at low elevations, due to the mutual coupling, as described in section 4.5. Even though this can be improved by mitigating the coupling using one of the decoupling techniques, the example shows that the XPD enhancement that can be achieved by improving the design of the single element can be much larger than the enhancement that can be achieved by decoupling the elements, which, for example, for a four-element array with element spacing of one quarter of a wavelength, does not enhance the XPD by more than 3 dB for any of the array eigenmodes.

The example, in summary, emphasizes the need for the proper design of the single element before building the array, and before using decoupling techniques to compensate for the influence of mutual coupling.

4.4.2 Simulation-based example

This section considers a study-case of a RHCP square patch antenna that is designed for GNSS applications. The antenna operates at the L1-band (1.57542 GHz) with a bandwidth

larger than 4 MHz and a realized gain larger than 3 dBi. The section discusses the influence of different antenna dimensions on the cross-polarization discrimination of the antenna, and recommends optimized dimensions for improving the suitability of the antenna for robust GNSS receivers.

The antenna is designed using a 5.08 mm thick substrate material of Rogers 3010 (with 10.2 permittivity). The relatively high permittivity is chosen to enable compact antennas, while the large thickness is chosen to enable high radiation efficiencies. The non-standard 5.08 mm thickness is achieved using two 2.54 mm layers with 0.1 mm adhesive material of Rogers 4450F (with 3.52 permittivity).

The excitation of the RHCP pattern is achieved through a single 50 Ω matched feeding port at one principal axis, by trimming the patch edges at one of the corners, as illustrated in Fig. 4.13.

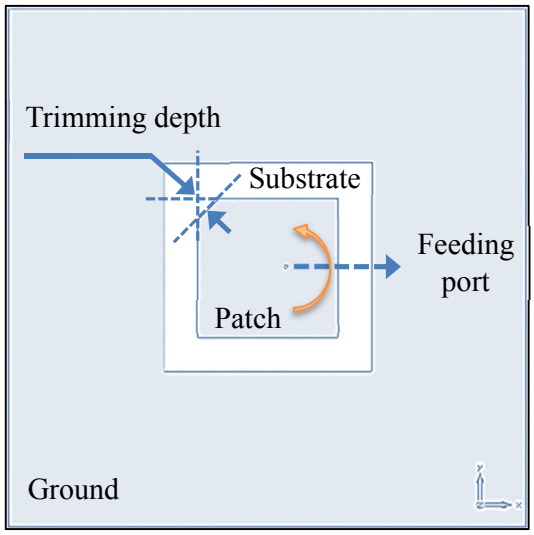

Figure 4.13: General top-view sketch of a GNSS patch antenna element fed and truncated to excite RHCP. The orange arrow, rotating counter clockwise, represents the direction of rotation of the radiated electrical field when looking from top towards the antenna (i.e., from front of the propagating wave)

The truncation breaks the symmetry of the patch allowing not only for the two short edges to radiate with a linear-polarized electrical field, but also for the other two edges to excite an orthogonal polarized field. The final radiated field is nothing but the superposition of both. The truncation was tuned to insure a 90° phase shift between the two polarizations, in order to excite a final radiating electrical field of either right-handed or left-handed circular polarization, with minor cross-polarization. The antenna polarization was optimized in electromagnetic full-wave simulations in CST microwave studio. The

polarization depends on the relative positions of the truncation and the feeding point. The studied design, shown in Fig. 4.13, results in a RHCP.

While, for simplicity, the example focuses on optimizing the XPD for only the RHCP, the same optimization results apply also for the LHCP, or eventually for the dual-polarized antenna, which can easily be achieved by only adding another 50 Ω matched feeding port at the orthogonal principal axis of the patch.

The design process results in an antenna of 26.9 mm x 26.9 mm patch area, with 44 mm x 44 mm substrate, 200 mm x 200 mm ground plane, and a trimming depth of 2.3 mm. The antenna features a realized gain of 6.3 dBi, with a - 22 dB reflection coefficient at the center frequency, a 34 MHz bandwidth, and a 15 dB cross-polarization discrimination at the main beam direction; everything that would be accepted for a classical RHCP GNSS receiver that focuses on the reception from high elevations, and pays no attention for multipath propagation, or jamming interferences.

However, a pure RHCP cannot be achieved for many reasons. A 90° phase shift, if achieved at one frequency at one corner or position, cannot be perfectly guaranteed at each frequency of the bandwidth, as the phase shift depends on the wavelength. It also cannot be guaranteed at each position of the patch, due to its asymmetrical geometry. Therefore, the resulting polarization is in fact a combination of the wanted polarization (here, the RHCP) and the unwanted one (the LHCP).

The purity of the RHCP polarization is tested by calculating the ratio between the RHCP and the LHCP radiated power, i.e., the XPD as defined in (3.3), with RHCP set as the co-polarization. The axial ratio (AR), which is defined as the amplitude ratio between the maximum and minimum components of the electrical field, i.e., for the studied antenna:

$$AR(\theta,\varphi) = \frac{\left|\vec{E}_x(r,\theta,\varphi)\right|}{\left|\vec{E}_y(r,\theta,\varphi)\right|} \tag{4.15}$$

can also be used, keeping in mind that it determines only if the antenna has a pure circular polarization (when AR=1) or not, without specifying if the polarization is right-handed or left-handed.

The XPD is a function of elevation and azimuth. A patch antenna usually has its XPD maximized at the main beam direction and minimized at low elevation, especially at directions pointing from the patch center towards its corners, i.e., at odd multiples of 45° azimuth according to Fig. 4.13.

The designed antenna gives a very good XPD of larger than 15 dB at zenith, and hence it is usually considered as a proper antenna for many applications. However, the antenna gives only 7 dB XPD at elevation of θ=85° and azimuth of φ=0°. This becomes worse at θ=85° and φ=45° where the XPD drops to as low as -2 dB, as depicted in Fig. 4.14, yielding almost a linear-polarized radiation, with the LHCP gain 2 dB higher than the RHCP gain. These poor XPD values at low elevations introduce notable polarization mismatch, and

consequently reduce the efficiency of the receive antenna. This confirms the need for considering the XPD behavior in antennas used for robust GNSS receivers.

The following paragraphs show how the XPD can be enhanced by tuning the different dimensions of the patch antenna, such as the trimming depth, the ground plane area, and the substrate area, while fixing the patch surface to avoid changing the operation frequency.

While the optimization process should consider all the parameters jointly, to find the global optimization solution, because they affect each other, the following study considers optimizing the antenna for the different parameter separately, in order to understand the individual influence of each parameter on the antenna polarization.

A- XPD versus the trimming depth:

Electromagnetic full wave simulations of the antenna were performed for different trimming depths. The relevant XPD values, at different elevation and azimuth angles, are stated in Table 4.1.

Table 4.1: XPD values (dB) at 1.57542 GHz versus the trimming depth (mm), at different directions; for a square truncated patch antenna with a patch size of 26.9 mm x 26.9 mm patch, a substrate of 44 mm x 44 mm, and a ground of 200 mm x 200 mm.

XPD (dB) at 1.57542 GHz		Trimming depth (mm)									
		1.0	1.5	2.0	2.3	2.5	2.7	**2.9**	3.1	3.5	4.0
φ=0°	θ=0°	2.4	5.2	8.3	15.1	20.4	19.8	**33.6**	14.1	11.1	7.8
	θ=45°	1.8	3.7	5.9	12.0	14.6	24.7	**17.4**	22.7	15.2	11.9
	θ=75°	1.4	2.8	4.6	9.2	11.1	16.2	**14.0**	30.1	23.0	15.8
	θ=85°	1.4	2.8	4.6	8.7	10.6	14.7	**13.9**	21.8	26.6	14.9
φ=45°	θ=0°	2.3	5.2	8.3	15.1	20.4	19.8	**33.6**	14.1	11.1	7.8
	θ=45°	-0.5	2.2	5.1	6.6	7.5	6.9	**8.6**	6.4	6.3	4.6
	θ=75°	-4.7	-3.7	-1.7	0.2	0.9	1.3	**1.8**	1.9	2.4	2.0
	θ=85°	-7.1	-7.2	-5.2	-2.3	-1.4	-0.5	**-0.3**	0.4	1.2	1.1
φ=90°	θ=0°	2.4	5.2	8.3	15.1	20.4	19.8	**33.6**	14.1	11.1	7.8
	θ=45°	2.2	5.7	9.6	12.3	13.7	10.8	**14.2**	8.4	7.1	4.4
	θ=75°	2.6	7.0	12.2	13.0	13.1	9.4	**11.7**	6.9	5.6	3.3
	θ=85°	2.8	7.7	13.8	15.5	14.8	10.1	**12.1**	7.3	5.8	3.7

The table shows that trimming depths smaller than 2 mm result is poor cross-polarization discrimination at all directions, meaning that the antenna is close to be linear-polarized, rather than RHCP antenna. Moreover, XPD has a negative value of -7.1 dB at azimuth of φ=45° and low elevation of θ=85° which identifies a LHCP antenna at that direction.

Increasing the trimming depth up to 3 mm enhances the XPD, not only at the main lobe direction (θ=0°) but also at low elevations (θ=75° to 85°) and for all azimuth angles. Nevertheless, it reaches only -0.3 dB at θ=85° and φ=45°, which means that the antenna has changed its polarization at that direction from LHCP to linear, but still not to RHCP. The poor XPD performance at φ=45°, appears along all diagonal directions (i.e., at odd-multiples of φ= 45°), due to the strong cross-polarized electrical field radiated along those directions, as describes in section 4.3.3 and shown in Fig. 4.6. This behavior appears for every trimming depth.

Larger trimming depths up to 4 mm slightly enhance the XPD at low elevations when φ=0°, and φ=45°, but dramatically decreases the XPD at the main lobe direction by about 20 dB, which is not recommended for GNSS signals.

A trade-off looking for a very good XPD (larger than 20 dB) at the main lobe-directions, with an accepted XPD (about 10 dB) at low elevations for azimuth of 0° and 90°, and at least a non LHCP at low elevations for azimuth of 45° ended up with a trimming depth of 2.9 mm. Additional numerical simulations found that this final choice was still valid when changing the side length of the substrate between 30 mm and 50 mm, and of the ground between 60 mm and 200 mm.

The resulting patch antenna is, in fact, what could be achieved through a classical design process, where the trimming depth is tuned to get the best circular polarization purity at the main lobe direction.

B- Influence of the ground plane:

The design, with a trimming depth of 2.9 mm, is now simulated for a ground plane area between 60 mm x 60 mm and 200 mm x 200 mm. The XPD values, presented in Table 4.2 show that designs with ground planes larger than 140 mm x 140 mm provide strong XPDs at the main lobe direction, due to the high directivity. However, they suffer from poor co-polarized gain, and hence poor XPD, at lower elevations.

On the other hand, ground areas smaller than 140 mm x 140 mm give smaller directivity, which results in slightly decreased XPD at the main lobe direction. However, they show notably enhanced XPD at low elevations, for all azimuths including the odd multiples of 45°. A ground planes of 100 mm x 100 mm results in an XPD larger than 12 B at an elevation of θ=85°, and larger than 29 dB at the main lobe direction. These results emphasize the strong influence the ground area has on the co- and cross-polarization of patch antennas. Results show that a proper optimization of the ground area can help to mitigate the cross-polarized fields along the diagonal axes.

However, a ground size as small as 60 mm x 60 mm provides a smaller mirroring effect, and hence a smaller radiation efficiency, resulting in an XPD of only 7 dB at the main lobe direction and 2.4 dB at low elevations.

Table 4.2: XPD values (dB) at 1.57542 GHz versus ground plane size, at different directions; for a square truncated patch antenna with a patch size of 26.9 mm x 26.9 mm patch, a substrate of 44 mm x 44 mm, and a trimming depth of 2.9 mm.

XPD (dB) at 1.57542 GHz		Side length (mm) of square ground plane									
		60	80	90	**100**	110	120	140	160	180	200
φ=0°	θ=0°	7.0	15.7	21.4	**29.6**	23.5	21.4	20.3	19.8	23.6	33.6
	θ=45°	7.4	14.4	17.7	**25.8**	25.6	37.4	16.4	31.2	18.3	17.4
	θ=75°	9.7	14.3	14.7	**17.0**	15.6	15.9	10.7	16.3	17.2	14.0
	θ=85°	10.9	15.6	14.7	**15.6**	13.5	13.0	8.6	12.1	16.4	13.9
φ=45°	θ=0°	7.0	15.7	21.4	**29.6**	23.5	21.4	20.3	19.8	23.6	33.6
	θ=45°	7.4	13.8	16.5	**20.4**	18.0	19.3	14.4	10.3	9.7	8.6
	θ=75°	9.2	12.8	13.7	**14.8**	12.6	12.5	9.1	5.2	2.7	1.8
	θ=85°	9.9	13.0	13.6	**14.2**	11.8	11.5	8.5	4.7	1.3	-0.3
φ=90°	θ=0°	7.0	15.7	21.4	**29.6**	23.5	21.4	20.3	19.8	33.6	33.6
	θ=45°	6.4	16.7	23.1	**20.1**	16.9	15.3	21.5	15.3	20.5	14.2
	θ=75°	4.1	16.3	21.0	**14.0**	11.4	9.6	11.5	10.7	15.2	11.7
	θ=85°	2.4	15.0	20.2	**12.8**	9.9	8.0	8.8	8.8	13.2	12.1

A trade-off between ensuring very good XPD at the main direction and enhancing the poor XPD at low elevations results in an area of 100 mm x 100 mm.

In summary, Table 4.1, and Table 4.2 show that it was possible to transform the polarization of the antenna at low elevations and 45° azimuth form LHCP to linear polarization, by optimizing the trimming depth, resulting in enhancing the XPD by about 7 dB. Thereafter, optimizing the ground plane area was enough to boost the low elevation XPD by about 13 dB, resulting in a RHCP even at the azimuths of odd multiples of 45°.

Note:

To avoid misunderstanding, the size of the ground plane cannot transform the polarization of the antenna from linear to circular if the antenna was not trimmed at first place to introduce the 90° phase shift between its two linear-polarized orthogonal radiation modes. In other words, optimizing the ground plane of a linear-polarized non-truncated patch antenna can only affect its co- and cross-polarized fields resulting in a new linear-polarized superposition field. Going from linear to circular polarization is only possible by introducing a 90° phase shift between two linear-polarized modes, e.g., by means of truncation.

C- XPD versus substrate dimensions:

At this stage, the antenna design was already optimized for its trimming depth and ground plane, considering a substrate of 44 mm x 44 mm. Simulations are run now to finally optimize the substrate size to improve the XPD, with the trimming depth of 2.9 mm and the ground plane are of 100 mm x 100 mm. Simulations will consider substrates between 34 mm x 34 mm and 54 mm x 54 mm.

The dielectric material plays a key role in determining the strength of the electrical fields between the patch surface and the ground, and ultimately the radiated electrical field [90]. Therefore, a substrate slightly larger than the patch area, e.g., 34 mm x 34 mm or smaller, results in a poor radiation efficiency of -11 dB, which gives a realized gain of only -5 dBi at the main lobe direction. Subsequently, this gives an XPD below 3 dB even at the main lobe direction.

The performance improves with larger substrates. A reliable XPD performance is achieved for substrates between 42 mm x 42 mm and 46 mm x 46 mm, as presented in Table 4.3. The best XPD values are achieved for 45 mm x 45 mm.

The XPD performance degrades again for substrates larger than 48 mm x 48 mm. This happens because the trimming depth becomes relatively small, comparing to the substrate size, so that it features smaller influence on the electrical fields that is excited in the large substrate. For designs with such a big substrate, it is probably needed to use larger trimming depths, or even three truncations at three corners of the patch, to retain an influence strong enough to change the field polarization.

Table 4.3: XPD (dB) at 1.57542 GHz versus substrate size, at different directions; for a square truncated patch antenna with a patch size of 26.9 mm x 26.9 mm patch, trimming depth of 2.9 mm and a ground size of 100 mm x 100 mm. Values upper limit is 40 dB.

XPD (dB) at 1.57542 GHz		Side length (mm) of square substrate									
		34	38	40	42	44	**45**	46	48	50	54
φ=0°	θ=0°	2.2	10.3	20.5	27.4	29.6	**> 40**	34.7	19.0	16.1	15.0
	θ=45°	2.7	11.9	24.1	22.2	25.8	**23.0**	26.5	15.2	13.1	12.4
	θ=75°	3.3	13.5	19.0	15.6	17.0	**15.8**	17.0	11.5	10.1	9.6
	θ=85°	3.4	13.6	17.4	14.4	15.6	**14.6**	15.6	10.7	9.5	9.0
φ=45°	θ=0°	2.2	10.3	20.5	27.4	29.6	**> 40**	34.7	19.0	16.1	15.0
	θ=45°	1.5	9.8	17.9	18.3	20.4	**20.8**	21.9	14.4	12.9	12.0
	θ=75°	0.6	8.7	13.9	13.6	14.8	**15.1**	15.6	11.4	10.4	9.7
	θ=85°	0.6	8.5	13.4	13.1	14.2	**14.5**	15.0	11.0	10.1	9.4
φ=90°	θ=0°	2.2	10.3	20.5	27.4	29.6	**> 40**	34.7	19.0	16.1	15.0
	θ=45°	1.8	8.4	15.8	20.6	20.1	**24.2**	21.3	23.1	19.9	18.0
	θ=75°	1.2	6.3	11.6	14.6	14.0	**15.8**	14.6	22.0	27.1	23.8
	θ=85°	1.0	5.7	10.7	13.3	12.8	**14.4**	13.3	19.9	24.8	23.6

4.4.3 Summary

The study shows that an antenna well designed in terms of operational frequency, radiation efficiency, and polarization at the main lobe could be useless for systems that require large XPD values at low elevations, such as robust GNSS receiver. However, a careful optimization may result in up to 16 dB XPD enhancement at low elevations. The main optimization steps of the study are summarized in Fig. 4.14.

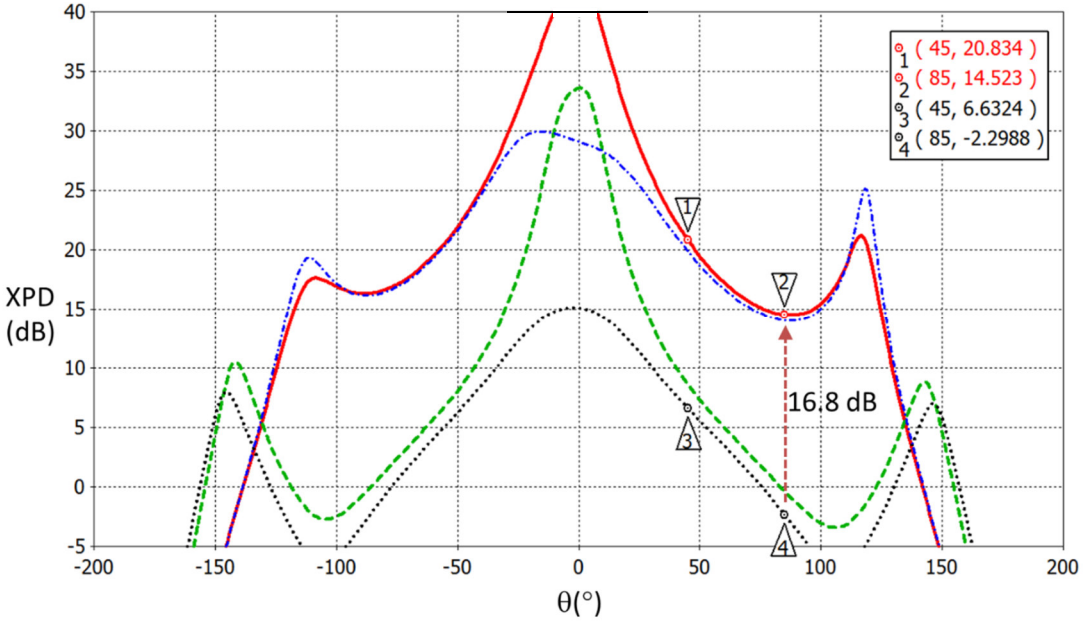

Figure 4.14: Enhancements of XPD patterns versus elevation, for the azimuth of 45°. The black dotted-curve represents the case of the first antenna design (trim depth of 2.5 mm). The green dashed-curve is the XPD of the design recommended by Table 4.1, where the trimming depth is tuned to 2.9 mm. The blue dash-dotted curve represents the design recommended by Table 4.2, where the best size of the ground plane was found (100 mm x 100 mm). The red solid curve is for the design recommended by Table 4.3 when the substrate size is slightly tuned to 45 mm x 45 mm. The asymmetry of the XPD curves around zero elevation is due to the asymmetry introduced by the trimmed patch itself, and not due to the mesh resolution of the simulated designs.

The figure shows that tuning the trimming depth, from 2.5 mm to 2.9 mm, helps mainly to enhance the XPD at the main lobe direction (from black dotted curve to green dashed curve). Moreover, changing the ground plane area from 200 mm x 200 mm to 100 mm x 100 mm reduces the directivity of the antenna and thus the XPD at the main lobe direction, but significantly increases the XPD by about 13 dB at low elevations (from green dashed curve to blue dash-dotted curve). Finally, a further tuning of the substrate size enhances the XPD again at the main lobe direction with minor impact on low elevations, resulting in the red solid curve. This large enhancement confirms that an antenna designed for robust GNSS

receivers must be studied differently, compared to normal antennas designs dedicated for single-polarized or narrow-beam applications.

4.5 Polarization purity in compact antenna array

As mentioned before, array-based receivers that use compact antenna arrays suffer from strong mutual coupling that affects not only its radiation eigenefficiencies, but also the polarization purity of the radiating elements. Therefore, an efficient exploitation of the polarization diversity gives rise to extend the polarization analysis to cover the impact of mutual coupling.

The following study explains how mutual coupling affects the co- and cross-polarizations, and subsequently the cross-polarization discrimination, of the radiating elements in a compact patch antenna array.

To simplify the discussion:

- Antennas with circular polarization are targeted, since this is the case of GNSS antennas, which are the antennas of interest in this thesis.
- Since a circular polarization is nothing but a combination of two linear polarizations with a 90° phase-shift between them, the study considers the linear polarizations at first, to ease the analysis, and the results are generalized to the case of circular polarizations.
- The study is confirmed by numerical simulations for the case of circular polarization, involving an example of a two-element compact patch antenna array.
- Since it is needed, in antenna arrays, to shift the position of the antenna element to allow the other antennas to be added, the influence of this shifting is also considered in this work. This influence is usually ignored in the literature of mutual coupling, even though it is not minor at all, as shown here.
- The study is followed by a quantitative analysis of how the influence of mutual coupling on XPD changes with the distance between the radiating elements.

While coupling effect is usually modeled in literature as a change in the apparent driving impedance of the antenna elements, referred to as “the mutual impedance variation”, as in [86, 90], this model does not consider the geometry of the antenna element, which is the main source behind the unwanted cross-polarized fields, and therefore it is not suitable to be used to study the mutual coupling effect on the cross-polarized fields, or eventually on the cross-polarization discrimination of radiating elements.

The study starts with the case of coupling between two linear-polarized patch antenna elements, where the two antennas are in different parallel E-planes, as shown in Fig. 4.15, where each E-plane is defined by the direction of the relevant electrical field and the direction of the relevant propagation, and passes across the center of the patch surface. The study considers then, the case of the coupling in the same E-plane, as shown in Fig. 4.16.

The following assumptions are considered, for simplicity, and to focus only on the coupling influence on radiation:

- All antennas are matched at the same resonance frequency.
- Distance between the elements $d < \lambda_0/2$.
- Coupling influence on the resonance frequency is ignored. This influence causes minor shifts of the resonance frequency of the antenna, resulting in reducing the co-polarization radiation efficiency at the original frequency, and accordingly the XPD at that frequency. This impact is easily mitigated by retuning the patch length. Therefore, it is ignored here.

4.5.1 Impact of mutual coupling in parallel E-planes

Fig. 4.15 represents a patch antenna array of two elements, which have two parallel E-planes o_1xz and o_2xz. If the antenna Patch 1 is excited then, as described in section 4.3.2, the fundamental mode TM^{z}_{100} dominates in the antenna, and results in a charge distribution as depicted in Fig. 4.2. A simplified top-view illustration of this charge distribution is also presented in Fig. 4.15, where only the x- and y-components of the electrical fields between the patch and the ground are presented, since they correspond to the radiation, while the z-components are ignored.

Patch 1 radiates a co-polarized electrical field $\vec{E}_{x1}$, and a cross-polarized electrical field $\vec{E}_{y1}$, as depicted in Fig. 4.15, and as discussed in 4.3.3. The charge distribution at Patch 1 results in exciting a mutual coupling electrical field, $\vec{E}_{y1,cp1}(x,y,z) + \vec{E}_{z1,cp1}(x,y,z)$ between these charges and the non-charged metallic surfaces of the second antenna Patch 2. The z-component of this field does not influence the far field wave propagation and hence is ignored here. Since $\vec{E}_{y1,cp1}(x,y,z)$ is directed along the oy-axes, it belongs to the cross-polarized electrical fields. Eventually, $\vec{E}_{y1,cp1}(x,y,z)$ results in charging the opposing surface of Patch 2 with opposite charges, as illustrated in the figure.

Since, for the dominant mode TM^{z}_{100}, the electrical field between the patch and the ground forms sinusoidal standing waves along the ox-axis, then the charge distribution on the surface of Patch 1 is sinusoidal as well. Accordingly, the resulting coupling electrical field $\vec{E}_{y1,cp1}(x,y,z)$ forms a sinusoidal standing wave between the two opposing edges of Patch 1 and Patch 2, with zero strength along the principal oyz-plane and maximum strength at the end of the two opposing edges, as illustrated in Fig. 4.15, and as defined by:

$$\vec{E}_{y1,cp1}(x,y,z) = A.\sin\left(\frac{2\pi}{\lambda_g}x\right).\vec{y}, \quad if: -\frac{\lambda_g}{2} \le x \le \frac{\lambda_g}{2}, \tag{4.16}$$

$$\text{where} \qquad A = \max\left|\vec{E}_{y1,cp1}(x,y,z)\right| \tag{4.17}$$

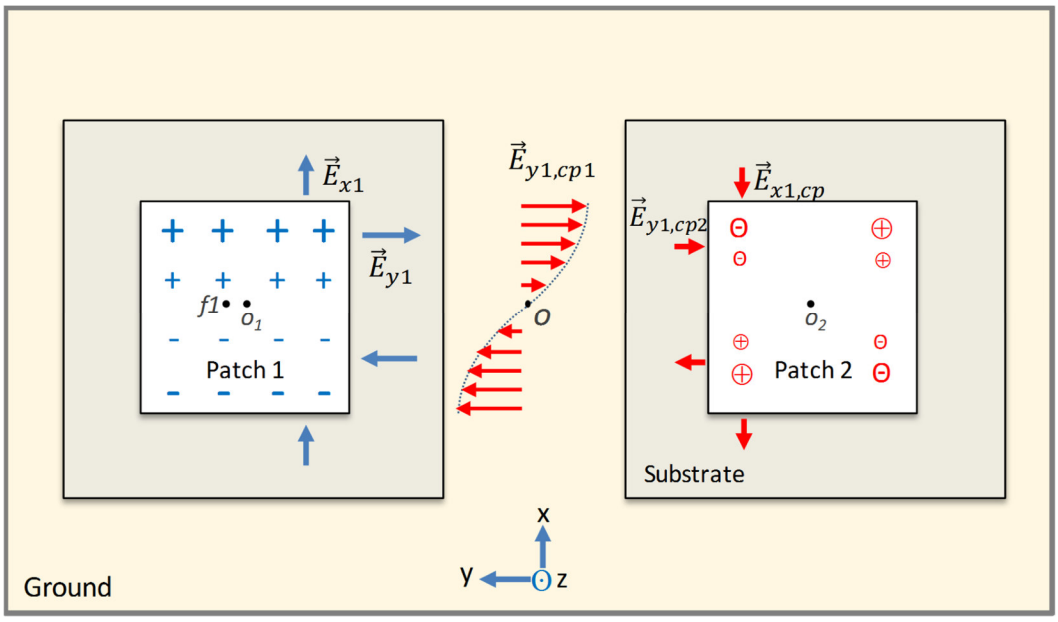

Figure 4.15: A simplified top-view illustration of the charge coupling from patch antenna 1 to patch antenna 2, when the electrical fields are in parallel E-planes. The charges in red circles represent the ones generated due to the mutual coupling. The electrical fields in red represent the coupled fields. The illustration shows only the top-view projection of the excited electrical fields, i.e., only the x- and y-components of the electrical fields, since the z-components do not affect the far field radiation. $f1$ is the feeding port of patch antenna 1.

$\vec{E}_{y1}$, the y-component of the field excited between the patch and the ground, has also a zero strength along the oyz-plane, as discussed in 4.3.3. Eventually, this results in a total cross-polarization electrical field of zero along the oyz-plane, i.e.:

$$\vec{E}_{y1,\text{in array}} = \vec{E}_{y1,cp1} + \vec{E}_{y1} = \vec{0} + \vec{0} = \vec{0}, \quad \text{along oyz} - \text{plane} \tag{4.18}$$

Nevertheless, $\vec{E}_{y1,cp1}$ and $\vec{E}_{y1}$ have non-zero strengths along any plane different from the oyz-plane, and especially near the opposing corners of the two patches.

$$\vec{E}_{y1,cp1} \neq \vec{0} \quad \text{along planes different from oyz} \tag{4.19}$$

$$\vec{E}_{y1} \neq \vec{0} \quad \text{along planes different from oyz} \tag{4.20}$$

Moreover, the coupling field $\vec{E}_{y1,cp1}$ is in phase with the original field $\vec{E}_{y1}$, since both are originated due to the same charge distribution at Patch 1, i.e.:

$$\arg(\vec{E}_{y1,cp1}) = \arg(\vec{E}_{y1}) \tag{4.21}$$

Therefore, these two fields add constructively, resulting in a larger cross-polarized field, comparing to the case of the single antenna element:

$$\left|\vec{E}_{y1,\text{in array}}\right| = \left|\vec{E}_{y1,cp1} + \vec{E}_{y1}\right| = \left|\vec{E}_{y1,cp1}\right| + \left|\vec{E}_{y1}\right| > \left|\vec{E}_{y1}\right| \quad (4.22)$$

Consequently, this results in decreasing the cross-polarization discrimination of Patch 1 in the array $XPD_{1,in\ array}$, comparing to that of the single element case $XPD_{1,single}$, i.e.:

$$XPD_{1,in\ array} < XPD_{1,single} \quad (4.23)$$

On the other hand, the coupled charges on the second patch excite the first dominant mode TM^{z}_{100} in Patch 2, as well, which results in exciting two electrical fields at Patch 2, the co-polarized field $\vec{E}_{x1,cp}(x,y,z)$ and the cross-polarized field $\vec{E}_{y1,cp2}(x,y,z)$, shown in Fig. 4.15.

Since the two antennas are identical, then they have the same cross-polarization discrimination in the single element mode, i.e.:

$$XPD_{1,single} = XPD_{2,single} = \left(\frac{\left|\vec{E}_{x1}(x,y,z)\right|}{\left|\vec{E}_{y1}(x,y,z)\right|}\right)^2 = \left(\frac{\left|\vec{E}_{x1,cp}(x,y,z)\right|}{\left|\vec{E}_{y1,cp2}(x,y,z)\right|}\right)^2 \quad (4.24)$$

The coupled charges at Patch 2 are opposite to those of Patch 1, and thus $\vec{E}_{x1,cp}$ is directed opposite to $\vec{E}_{x1}$. If α^2 represents the coupling ratio between the two patches, then $\vec{E}_{x1,cp}(x,y,z)$ can be written as:

$$\vec{E}_{x1,cp}(x,y,z) = -\alpha.\vec{E}_{x1}(x-d,y,z), \quad (4.25)$$

where d is the element spacing.

Hence, according to (4.24), and considering that $\vec{E}_{y1,cp2}(x,y,z)$ and $\vec{E}_{y1}(x,y,z)$ have the same direction, as shown in Fig. 4.15, $\vec{E}_{y1}(x,y,z)$ can be written as:

$$\vec{E}_{y1,cp2}(x,y,z) = \alpha.\vec{E}_{y1}(x-d,y,z) \quad (4.26)$$

As the element spacing $d < \lambda_0/2$, then the phase difference cause by the distance d is:

$$\phi = \frac{2\pi}{\lambda_0} d < \pi \quad (4.27)$$

which means that the fields $\vec{E}_{x1,cp2}(x,y,z)$ and $\vec{E}_{x1}(x,y,z)$ add destructively in the space, while $\vec{E}_{y1,cp2}(x,y,z)$ and $\vec{E}_{y1}(x,y,z)$ add constructively, i.e.:

$$\begin{aligned}\left|\vec{E}_{x1,total}(x,y,z)\right| &= \left|\vec{E}_{x1,}(x,y,z) + \vec{E}_{x1,cp}(x,y,z)\right| \\ &= \left|\vec{E}_{x1,}(x,y,z) - \alpha.\vec{E}_{x1}(x-d,y,z)\right| \\ &< \left|\vec{E}_{x1,}(x,y,z)\right|, \text{ for } d < \frac{\lambda_0}{2}\end{aligned} \quad (4.28)$$

$$\begin{aligned}\left|\vec{E}_{y1,total}(x,y,z)\right| &= \left|\vec{E}_{y1,}(x,y,z) + \vec{E}_{y1,cp2}(x,y,z) + \vec{E}_{y1,cp1}(x,y,z)\right| \\ &= \left|\vec{E}_{y1,}(x,y,z) + \alpha.\vec{E}_{y1}(x-d,y,z) + \vec{E}_{y1,cp1}(x,y,z)\right| \\ &> \left|\vec{E}_{y1,}(x,y,z)\right|, \quad \text{for} \quad d < \frac{\lambda_0}{2} \end{aligned} \tag{4.29}$$

This means that coupling the second patch results in decreasing the strength of the co-polarized fields and increasing the strength of the cross-polarized fields, resulting in decreasing the cross-polarization discrimination of the antenna element Patch 1.

4.5.2 Impact of mutual coupling in the same E-plane

This case is depicted in Fig. 4.16. The two patch antennas have the same E-plane oxz. Here as well, the charges excited at the first patch excite opposing charges at the other patch, resulting in a coupling electrical field between the two edges, represented by $\vec{E}_{x1,cp1}$.

Apparently, it was shown in the case of parallel E-planes that studying how the fields add constructively and destructively was enough to show how mutual coupling results in increasing the strength of the cross-polarized field and decreasing the cross-polarization discrimination, without involving the loss of power due to coupling or dissipation. However, in contrast to that, it is not straightforward to find the influence of mutual coupling on the XPD patterns in the case of coupling in the same E-plane if the same approach was followed, since both co-polarized fields $\vec{E}_{y1}$ and $\vec{E}_{y1,cp1}$are in phase here, which for the first instance could mean a total co-polarization electrical field of larger strength. Therefore, it must be considered here that coupling does not provide an additional source of energy, and hence, if only Patch 1 is fed, then the total radiated power in case of no mutual coupling is written as:

$$P_{rad,single} = P_{rad,with\ cp} + P_{cp} + P_{diss} \ > \ P_{rad,with\ cp}\ , \tag{4.30}$$

where $P_{rad,\ single}$ is the total power radiated by the single antenna element in the case of no coupling, $P_{rad,with\ cp}$ is the power radiated by the element in the case of coupling, P_{cp} is the power of the coupling field, and P_{diss} is the dissipated power.

Hence, the total radiated power with coupling is always smaller than the one without coupling.

On the other hand, it must be considered that mutual coupling between two patch antennas, which have the same E-plane (Case B), is larger than that of the case of parallel E-planes (Case A). This is because the opposing edges in Case B have uniform charge distributions, as depicted in Fig. 4.16, so that the coupling electrical fields add constructively, while the opposing edges in Case A have sinusoidal charge distributions, as depicted in Fig. 4.15, so that the coupling fields add destructively. As a quantitative example, S-parameter measurements of a four-element GNSS patch antenna array, presented in Chapter 5 in Fig. 5.3, revealed that coupling in Case B was about 10 dB larger than that of Case A for $\lambda_0\backslash 5$

element spacing, and 6 dB larger for $\lambda_0\backslash 4$ element spacing. Since this strong level of coupling happens along the x-direction, it reduces the strength of the co-polarized field $\vec{E}_{x1}$ more than the cross polarized field $\vec{E}_{y1}$, resulting eventually in reducing the cross-polarization discrimination of the antenna.

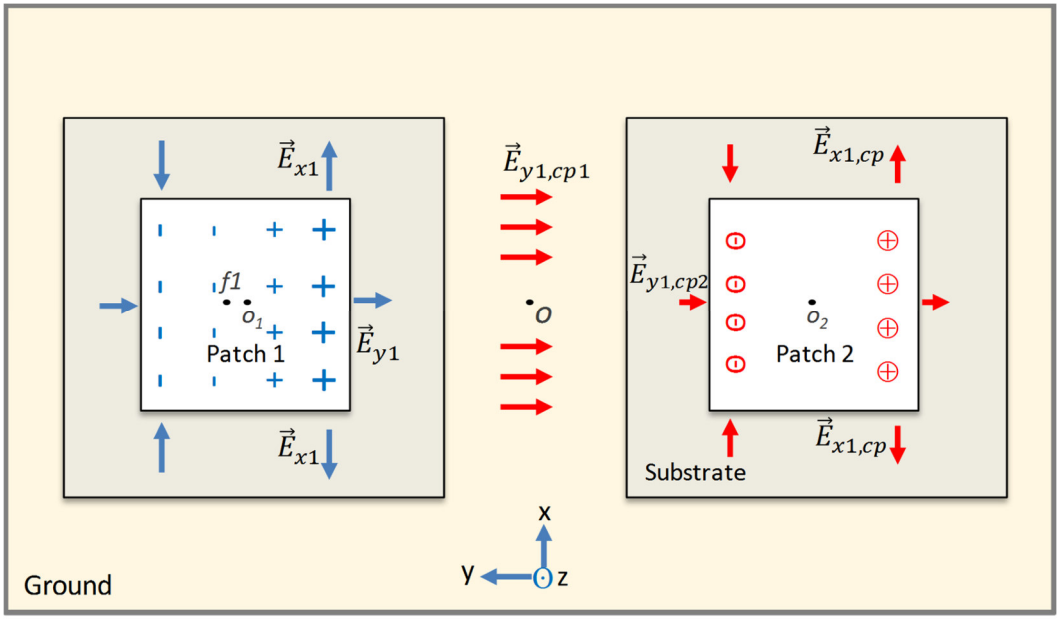

Figure 4.16: A simplified top-view illustration of the charge coupling from patch antenna 1 to patch antenna 2, when the two antennas have the same E-planes oxz. The charges in red circles represent the ones generated due to the mutual coupling. The electrical fields in red represent the coupled fields. $f1$ is the feeding port of patch antenna 1.

4.5.3 Influence of element-shifting

Fig. 4.17 illustrates an example of a two-element RHCP antenna array, operating at the L1-band, with the optimized antenna dimensions found in section 4.4, a common ground plane of 125 mm x 125 mm, and an element spacing of $d = \lambda_0/4$.

The study described in sections 4.3 and 4.4 showed that the excitation of the cross-polarized electrical fields, and subsequently the XPD pattern, are strongly determined by the geometry of the antenna. However, it is needed to extend the study to involve the impact of repositioning the single antenna element on its polarization purity.

Numerical simulations revealed that only shifting the first element away from the center of the ground plane, in order to give the place for the other element, as depicted in Fig. 4.17, significantly increases the cross-polarized gain pattern at all directions, even before introducing the other radiating element. A φ-cut of the cross-polarized gain pattern of the

first antenna element is shown in Fig. 4.18, before and after shifting by $d/2 = \lambda_0/8$. The resulting XPD patterns for the different cases are depicted in Fig. 4.19.

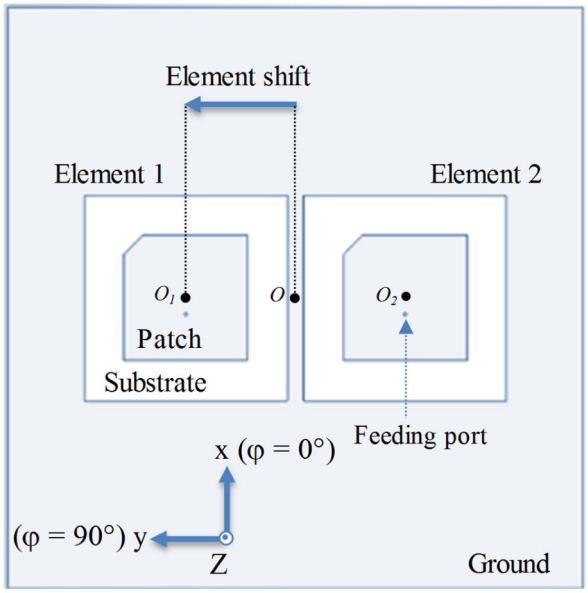

Figure 4.17: Top-view of a two-element RHCP patch antenna array, showing the shifting of the single antenna element away from the array center to give place for the other element.

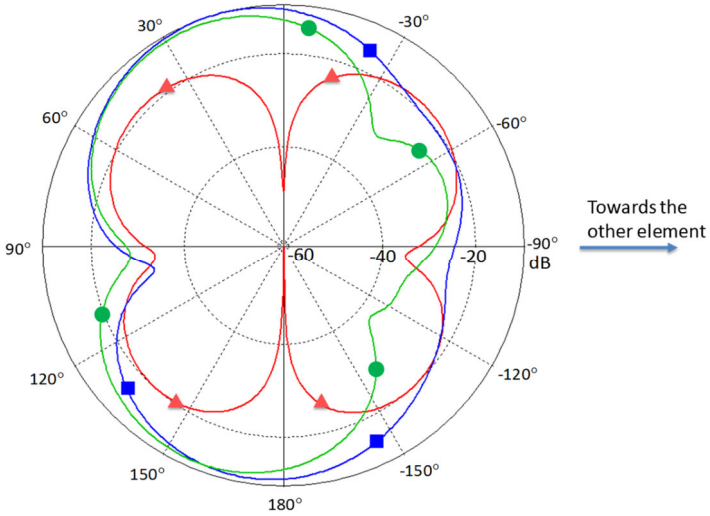

Figure 4.18: φ-cut of the cross-polarized gain pattern of the single antenna element No. 1, at θ=45°, before shifting (red-triangles curve), after shifting (green-circles curve), and after introducing coupling with of the other antenna element (blue-squares curve).

The strong impact of shifting is attributed to the asymmetry it introduces to the ground plane geometry, which reduces the possibility for the cross-polarized electrical fields that rise between the patch surface and the ground to cancel each other. This influence is eliminated only for infinitely large ground planes where shifting does not introduce geometrical differences.

Figure 4.18 reveals that the impact of element shifting on the cross-polarized gain pattern can be even larger than the impact of mutual coupling for some geometries.

Practically, while it is possible to partially mitigate the mutual coupling and reduce its impact, the influence of shifting can be partially reduced by extending the dimensions of the ground plane, which might not be desired for compact antenna systems, or by shaping the ground plane as in [49].

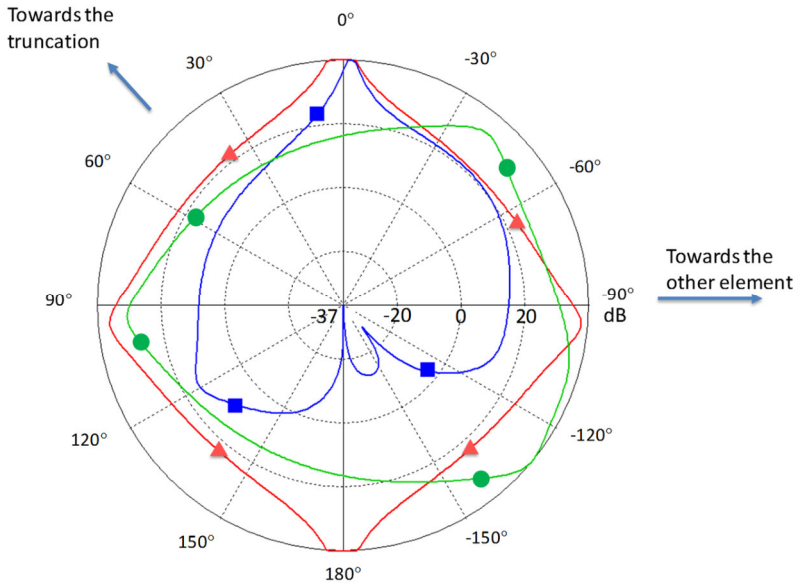

Figure 4.19: φ-cut at θ=45° of XPD patterns of the single antenna element (red-triangles curve), the single antenna after shifting (green-circles curve), and finally the antenna after introducing coupling with the other antenna (blue-squares curve).

4.5.4 Impact of mutual coupling on circular-polarized patch antennas

The two square patch antennas are fed to excite the right-handed circular polarization, or in other words they excite two linear polarizations (oriented along the x- and y-directions) with 90° phase shift. Therefore, the two patch antennas have the same E-plane oyz for the linear polarization that is oriented along the y-direction, and two parallel E-planes o_1xz and o_2xz for the orthogonal linear polarization that is oriented along the x-direction. Hence, the impact of mutual coupling on linear polarizations can be generalized to the case of circular-polarized antennas.

Numerical simulations presented in Fig. 4.18 show a φ-cut of the cross-polarized gain pattern of the Element 1, with and without introducing the mutual coupling with of the other antenna element. The cross-polarized gain pattern increases with coupling along both x-directions (φ= 0°, and φ=180°), and along the y-direction towards the coupling element (φ= -90°). Eventually, this leads to decreasing the XPD at these directions as depicted in Fig. 4.19.

Figure 4.20 and figure 4.21 show how the surface current of the studied RHCP patch antenna changes with mutual coupling. The figures are based on numerical simulations performed in CST microwave studio. At first, the surface current of the single-element mode is illustrated in Fig. 4.20. The animation phase is changed between 0°, 90°, and 180° to give the impression of the rotation.

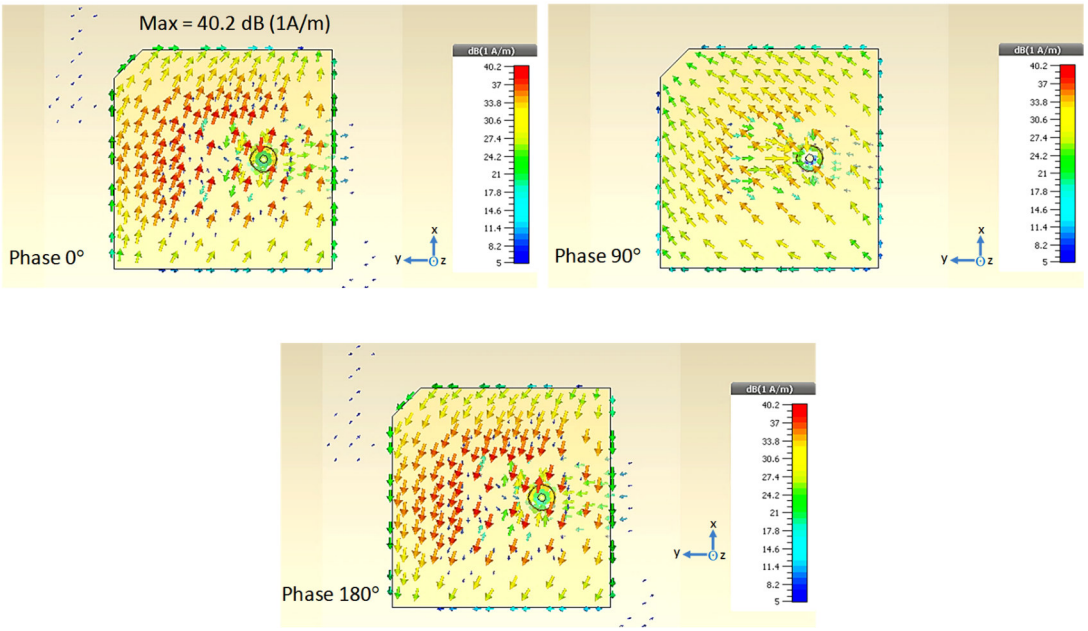

Figure 4.20: Surface current of the single-element RHCP patch antenna, shown at different animation phases, 0°, 90°, and 180° to illustrate the rotation.

Then, the surface current is calculated for the antenna in the array, with element spacing of 〖λ〗_0/4, and presented in Fig 4.21, at the same animation phases. The comparison between the two figures shows that the maximum amplitude of the surface current of Element 1 is reduced by about 3.8 dB in the array mode. Figure 4.21 shows also that the coupled surface current excited at Element 2 is rotating opposite to the original current at Element 1, which means that this current excites the LHCP, i.e., the cross-polarized field,

at the Element 2, resulting in decreasing the cross-polarization discrimination of the Element 1.

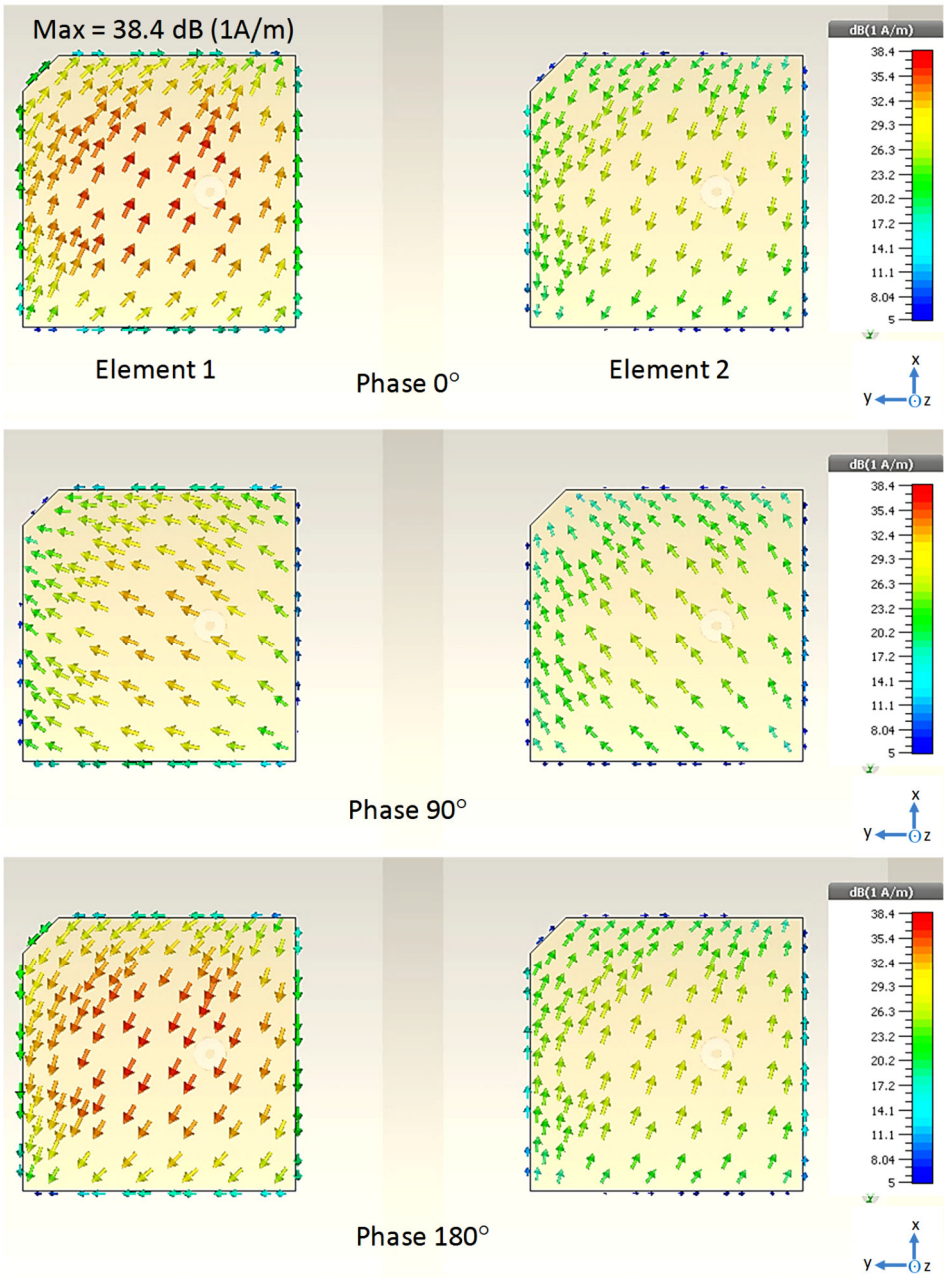

Figure 4.21: Surface current resulting from exciting one patch antenna (the element on left), in a two-element array, with element spacing of λ_0/4, at different animation phase.

Why does coupling result in a LHCP coupled field, from a RHCP original field?

The RHCP co-polarization of Element 1 is achieved by exciting the two co- linear-polarized fields $\vec{E}_{x1}$ that is presented in Fig. 4.15, and $\vec{E}_{y1}$ that is presented in Fig. 4.16, with $\vec{E}_{x1}$ delayed by a phase shift of 90°, i.e.,

$$phase\left(\vec{E}_{x1}\right) = phase\left(\vec{E}_{y1}\right) - 90^\circ \tag{4.31}$$

As seen in Fig. 4.15, $\vec{E}_{x1}$ results in a coupled field $\vec{E}_{x1,cp}$ directed to the opposite direction of $\vec{E}_{x1}$. On the other hand, Fig. 16 shows that $\vec{E}_{y1}$results in a coupled field $\vec{E}_{y1,cp2}$ directed in the same direction of $\vec{E}_{y1}$. Hence:

$$\begin{aligned} phase\left(\vec{E}_{x1,cp}\right) &= phase\left(\vec{E}_{y1,cp2}\right) - 90^\circ + 180^\circ \\ &= phase\left(\vec{E}_{y1}\right) + 90^\circ \end{aligned} \tag{4.32}$$

Hence, the phase delay between and x- and y-components of the electrical field is inverted at the coupled antenna, which results in exciting a LHCP coupled field.

Influence of ground edges:

Numerical simulations revealed that the surface current at the edges of the ground was about 50 dB smaller than the maximum surface current at the patch surface, and therefore it has a minor influence on the cross-polarization discrimination. One reason for that minor influence is that the dimensions of the ground plane in this design were already optimized for maximum cross-polarization discrimination, as described in section 4.4. Hence, a different influence is expected for other ground plane dimensions.

4.5.5 Impact of coupling versus element spacing - Quantitative analysis

A quantitative analysis based on electromagnetic full-wave simulations was performed, using the frequency solver of CST microwave studio, on the two-element antenna array presented in Fig. 4.17, to study the influence of mutual coupling on radiation parameters of the array, and how it changes for different values of element spacing.

The study starts from the design of a single element optimized for the best XPD pattern as recommended by section 4.4. The patch has a 26.9 mm x 26.9 mm patch size, a 45 mm x 45 mm substrate size, a 2.9 mm trim depth, and a 100 mm x 100 mm ground area.

However, with these dimensions, the element spacing between two elements in the array was limited to the interval between $0.24\lambda_0$ (the substrates overlap below this value) and $0.29\lambda_0$ (after which the substrate becomes larger than the ground plane). To enable smaller and larger values of the element spacing, a ground plane of 125 mm x 125 mm, and a

common substrate of the same ground plane size were used. The selected dimensions allow to change the element spacing between $0.15\lambda_0$ and $0.4\lambda_0$.

The antenna with the new dimensions gives, in the single-element mode, an XPD pattern with values greater than 9 dB at all directions, as shown in Table 4.4.

Table 4.4: XPD (dB) versus different directions, at 1.57542 GHz, for a square truncated patch antenna with a trimming depth of 2.9 mm, a ground and substrate size of 125 mm x 125 mm, and a patch size of 26.9 mm x 26.9 mm

	Azimuth φ=0°				φ=45°				φ=90°			
Elevation θ	0°	45°	75°	85°	0°	45°	75°	85°	0°	45°	75°	85°
XPD (dB)	29.6	19.4	12.0	10.0	29.6	14.4	9.7	9.2	29.6	29.3	14.3	11.4

A detailed numerical analysis was performed to quantify the influence of array compactness on resonance frequency, radiation efficiency, and reflection efficiency, realized gain, and XPD. The study involves also the influence of shifting the single element before introducing the other element.

A- Influence of coupling on resonance frequency and radiation efficiency:

The existence of other radiating or passive metallic elements in the vicinity of the radiating element introduces frequency dependent parasitic effects that strongly influence the input impedance of the element, which shifts the resonance frequency of the antenna elements. Numerical results presented in Table 4.5 describe how the effective resonance frequency of one antenna element changes versus different element spacing values in the compact antenna array presented in Fig. 4.17.

Table 4.5: Resonance frequency and reflection coefficient $\mathbf{S_{11}}$ of a RHCP patch antenna, in case of single-element, with/without shifting, and in compact array with different degrees of compactness

	Single element	Single element shifted by $0.2\lambda_0$ from center	Two-element array with different element-spacing					
			$0.4\lambda_0$	$0.35\lambda_0$	$0.3\lambda_0$	$0.25\lambda_0$	$0.2\lambda_0$	$0.15\lambda_0$
Effective resonance frequency (GHz)	1.575	1.591	1.591	1.591	1.595	1.603	1.621	1.639
S_{11} at 1.575 GHz (dB)	-12.0	-6.7	-7.0	-7.0	-6.3	-4.7	-3.3	-1.5
S_{11} at the actual resonance frequency (dB)	-12.0	-9.3	-9.4	-11.1	-12.7	-12.6	-10.6	-13.1

Table 4.5 highlights the need to retune the antenna elements used in compact arrays, to compensate for the frequency shift and restore the loss in the reflection efficiency.

The frequency shift versus the element spacing is highlighted in Fig. 4.22.

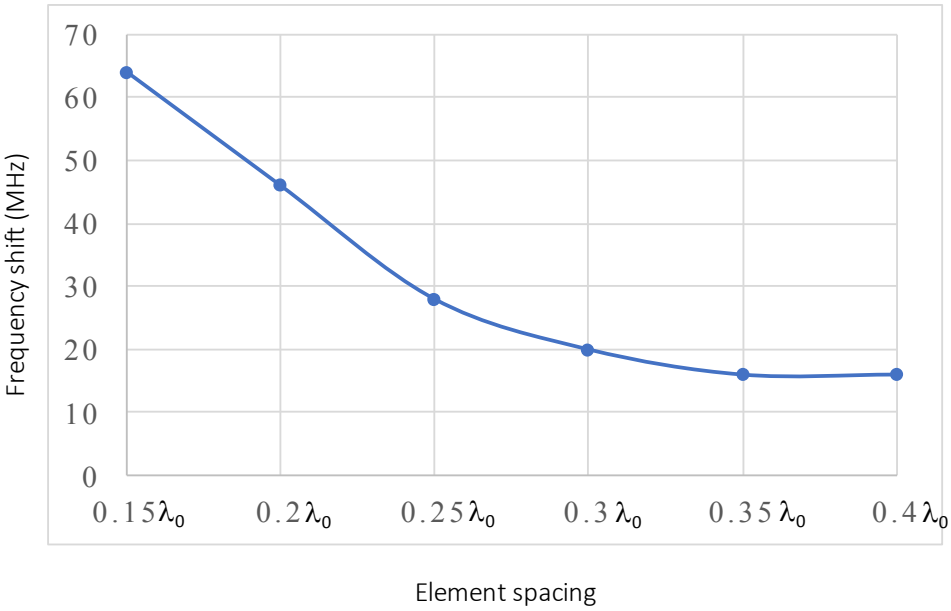

Figure 4.22: Resonance frequency shift versus element spacing, in a two-element patch antenna array at the L1-band.

Subsequently, Table 4.6 presents the influence of compactness on the radiation and reflection efficiencies of the array. The table 4.6 shows that shifting causes a small loss of about 0.7 dB to the radiation efficiency of the antenna element. On the other hand, the reflection efficiency, and thus the total radiation efficiency, were significantly reduced by the mutual coupling, especially for element spacing values below $0.25\lambda_0$.

Table 4.6: Radiation and reflection efficiencies of a RHCP patch antenna, at the nominal resonance frequency of 1.575 GHz, in case of single-element, with/without shifting, and in compact array with different degrees of compactness

	Single element	Single element shifted by $0.2\lambda_0$ from center	Two-element array with different element spacing					
			$0.4\lambda_0$	$0.35\lambda_0$	$0.3\lambda_0$	$0.25\lambda_0$	$0.2\lambda_0$	$0.15\lambda_0$
Radiation efficiency (dB)	-0.54	-0.48	-0.50	-0.53	-0.59	-0.65	-0.77	-0.61
Reflection efficiency (dB)	-0.33	-1.04	-1.05	-1.16	-1.56	-2.43	-3.64	-6.87
Total efficiency (dB)	-0.87	-1.52	-1.55	-1.69	-2.15	-3.08	-4.41	-7.48
Realized gain (dBi)	5.44	4.37	3.84	4.14	4.12	3.81	2.48	-1.10

Since Table 4.6 involves three cases, the single antenna, the shifted single antenna, and the compact antenna array mode, Figure 4.23 is presented to highlight specifically the case of antenna array, showing the influence of element spacing on the antenna efficiencies. The figure confirms similar results found by other works [4, 76].

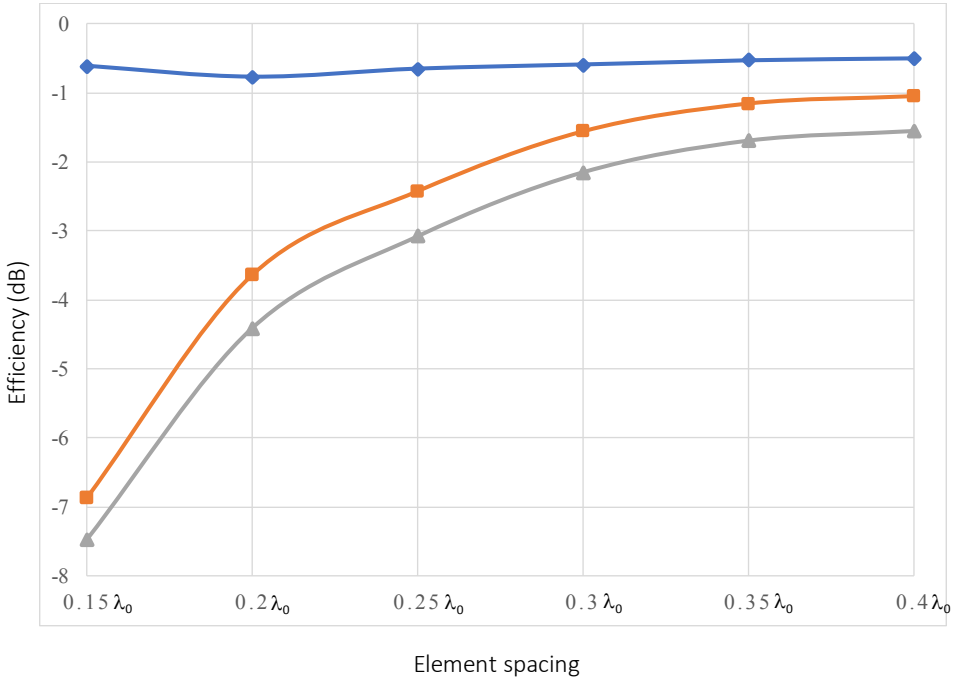

Figure 4.23 Influence of element spacing on the antenna radiation efficiency (blue-diamonds curve), reflection efficiency (orange-squares curve), and total efficiency (grey-triangles curve), of a square patch antenna in a two-element patch antenna array.

B- Influence of coupling on cross-polarization discrimination

At this point, simulations were performed to monitor the XPD pattern of the patch element 1 at the nominal resonance frequency 1.575 GHz, versus different values of element spacing. The achieved results are stated in Table 4.7.

The table shows the following points:

- Shifting has a strong influence on the XPD, mostly in a negative way, especially at directions towards the other element. This is also depicted in Fig. 4.24.
- Mutual coupling has a small impact on the XPD at element spacing larger than 0.3 λ_0, since most of the influence is attributed to the shifting.
- Mutual coupling significantly decreases the XPD values at all directions for element spacing below 0.3 λ_0. This behavior is illustrated in Fig. 4.24.

Table 4.7: XPD values of element 1, at the nominal resonance frequency of 1.575 GHz, versus different values of element spacing.

XPD (dB) at 1.57542 GHz		Single element at center of the ground plane	Single element shifted by $0.2\lambda_0$ from center	Two-element array with different element spacing					
				$0.4\lambda_0$	$0.35\lambda_0$	$0.3\lambda_0$	$0.25\lambda_0$	$0.2\lambda_0$	$0.15\lambda_0$
φ=0° (***oxz***-plane)	θ=85°	10.0	19.2	15.9	16.7	13.3	9.9	5.2	-3.1
	θ=45°	19.4	20.6	15.2	17.0	14.4	13.1	8.2	-2.4
	θ=0°	29.6	16.7	10.9	11.7	10.5	11.5	8.4	-0.8
	θ=-45°	21.8	6.5	4.3	4.4	4.7	7.2	6.3	0.3
	θ=-85°	10.5	-4.2	-5.2	-3.9	-1.7	2.0	3.0	1.3
φ=45°	θ=85°	9.2	12.2	21.4	16.6	11.8	11.5	11.5	-12.2
	θ=45°	14.4	21.8	13.5	14.3	12.9	13.7	12.7	-7.6
	θ=0°	29.6	16.7	10.9	11.7	10.5	11.5	8.4	0.8
	θ=-45°	16.2	5.6	10.0	8.7	6.4	2.6	-2.0	2.7
	θ=-85°	10.5	4.2	8.9	8.0	6.5	2.6	-3.0	3.5
φ=90° (***oyz***-plane)	θ=85°	11.4	16.1	12.4	12.4	13.3	19.8	15.4	-8.7
	θ=45°	29.3	15.7	11.7	13.8	14.8	21.0	22.9	-5.9
	θ=0°	29.6	16.7	10.9	11.7	10.5	11.5	8.4	0.8
	θ=-45°	23.4	8.7	19.9	22.2	18.1	8.4	-8.8	8.4
	θ=-85°	11.2	12.2	14.5	15.5	17.1	13.2	3.8	10.0

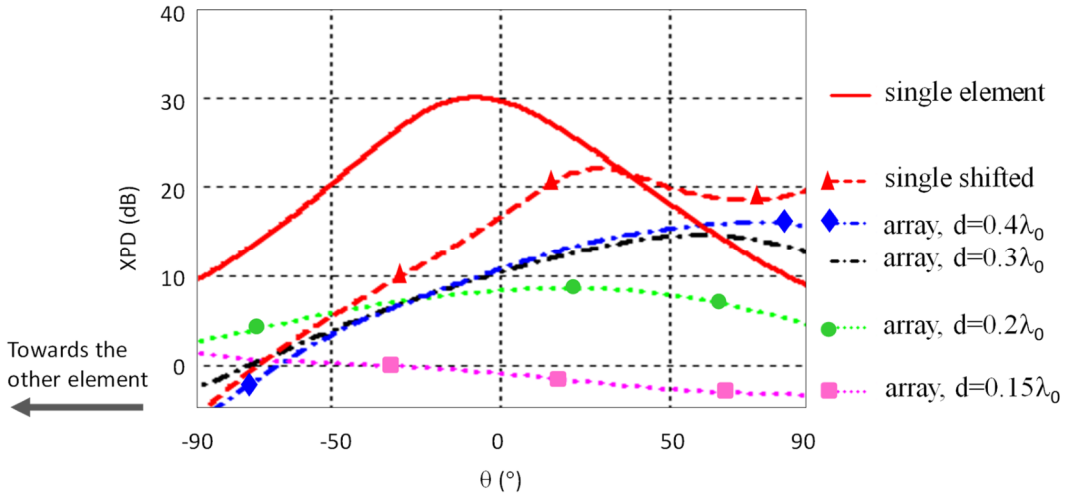

Figure 4.24: θ-cut at φ=0° of the XPD pattern of an antenna element in single-mode and in a compact two-element patch antenna array, showing the influence of mutual coupling on the XPD at the resonance frequency, for element spacing between $0.15\lambda_0$ and $0.4\lambda_0$.

Chapter 5:

Robust Dual-band Dual-polarized Compact GNSS Receiver

5.1 Receiver architecture

This chapter describes the architecture of an array-based dual-band dual-polarized GNSS receiver that features robustness against jamming, spoofing and multipath propagation. This description focuses on the analog part of the receiver, whose block diagram is depicted in Fig. 5.1. Later, the chapter covers the integration with an array-based digital receiver that performs data acquisition and signal processing, and drives the antenna system to apply beamforming and anti-jamming null-steering.

The analog part of the receiver includes in sequence:

1- A compact antenna array, which consists of four dual-band dual-polarized patch antenna elements, resulting in eight RF receive channels, as following:

- Four L1/E1 + L5/E5a dual-band channels, with linear polarization LP1.
- Four L1/E1 + L5/E5a dual-band channels, with linear polarization LP2.

The receiver uses either the single-layer or the multi-layer antenna elements described in Chapter 3.

2- Eight 90° phase-shift hybrid couplers to excite the two circular polarizations RHCP and LHCP. The hybrid couplers provide the following RF channels at their output:

- Four L1/E1 + L5/E5a dual-band channels, with RHCP.
- Four L1/E1 + L5/E5a dual-band channels, with LHCP.

3- Two decoupling and matching networks (DMN), one for each polarization, to mitigate the influence of the mutual coupling in the array, and restore part of the array radiation eigenefficiencies.

4- A calibration network that enables the digital receiver to calibrate the RF output levels after matching.

5- An amplifying and filtering stage, which contains RF low-noise amplifiers and frequency diplexers. The following channels result from the frequency diplexers:

- Four L1/E1 channels, with RHCP.
- Four L5/E5a channels, with RHCP.
- Four L1/E1 channels, with LHCP.
- Four L5/E5a channels, with LHCP.

6- 16-channel RF-IF front-end, to perform RF-IF down-converting, and provide 16 IF channels to the digital receive, as following:

- Four L1/E1–IF down-converted channels, with RHCP.
- Four L1/E1–IF down-converted channels, with LHCP.
- Four L5/E5a–IF down-converted channels, with RHCP.
- Four L5/E5a–IF down-converted channels, with LHCP.

However, due to resource limitations in the FPGA circuit used in the digital receiver, only 12 channels could be processed. Therefore, the four L5/E5a–IF channels with LHCP polarization were omitted. The omitted channels were selected based on the lower importance of the LHCP polarization, considering that the GNSS signal has a RHCP, and based on the quality of service provided at the L1/E1 frequency band.

In summary, the entire receiver is designed to provide access for 12 RF channels, as following:

- Four L1/E1 channels, with RHCP.
- Four L1/E1 channels, with LHCP.
- Four L5/E5a channels, with RHCP.

Hence, dual polarization functionality will be provided only for the L1/E1 frequency band.

The components of the receiver are described in detail in the following sections.

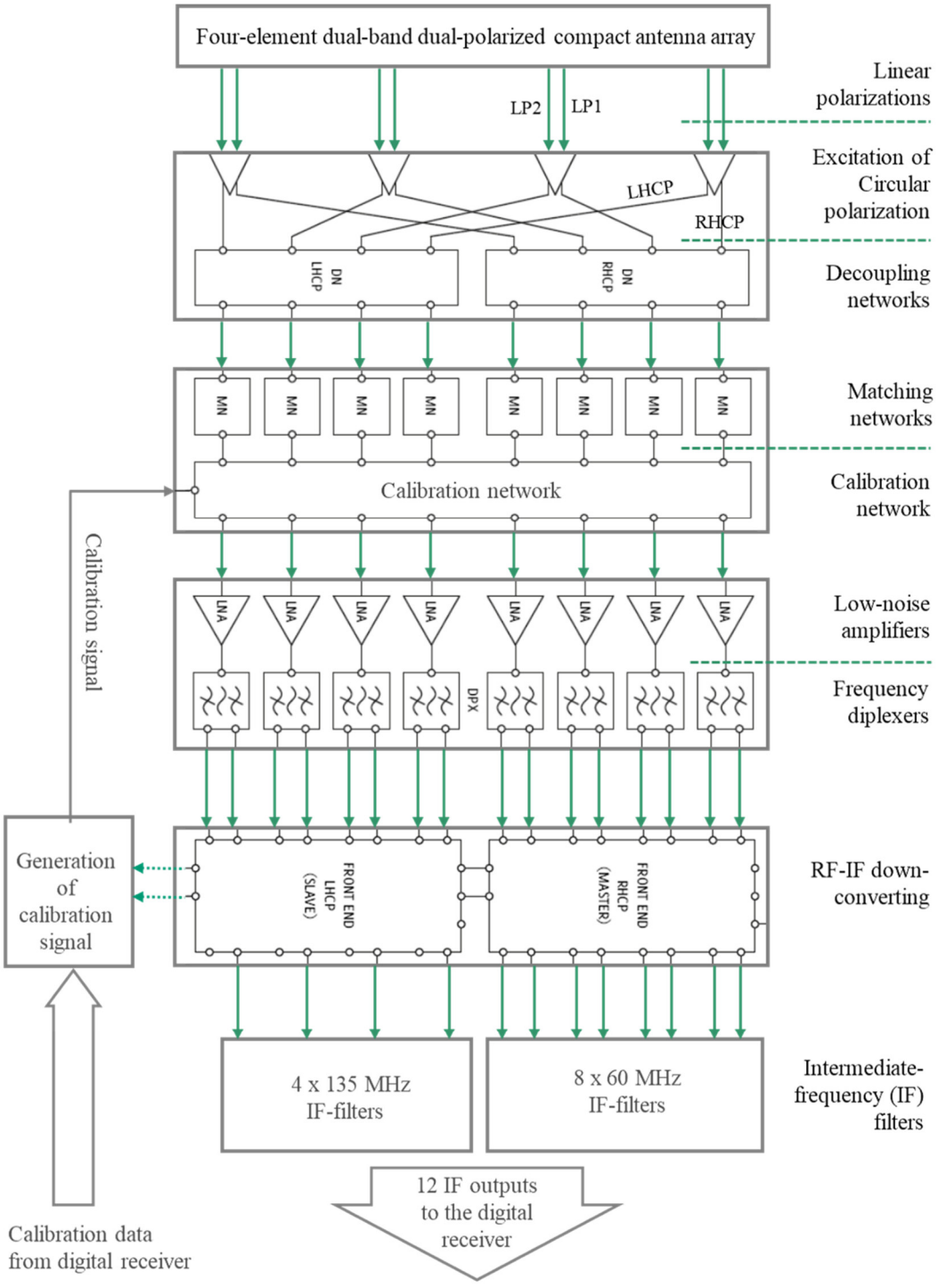

Figure 5.1: Block diagram of the analog part of the receiver architecture, with main components and signal flow.

5.2 Dual-band dual-polarized compact antenna array

5.2.1 Array design

Two different antenna arrays, composed of four dual-band and dual-polarized patch antenna elements, were designed for the GNSS receiver. For the first array, the multi-layer patch antennas described in section 3.2 and in [66] and [67] where used as the radiating elements. For the second arrays, the single-layer stub-loaded patch antenna elements described in section 3.3 and in [51] were used. The arrays are illustrated in Fig. 5.2 and Fig. 5.3.

Both arrays operate at the two frequency bands: L1/E1-band (centered at 1.57542 GHz) and L5/E5a-band (centered at 1.17645 GHz). The arrays operate at bandwidths of about 4 MHz at L1-band and 20 MHz at L5-band, which is required for GNSS data acquisition.

The antennas were built using the high dielectric permittivity (of 10.2) Rogers 3010 laminates [23], to reduce the physical sizes at given frequency, and enable the compact arrangement. Two or three layers of the 2.54 mm thick laminates were used to increase the substrate thickness, in order to enhance the antenna efficiency. The layers were glued together using the adhesive material Rogers 4450F [28]. The total thicknesses of the antennas were 5.18 mm for the single-layer antenna and 7.82 mm to 9.82 mm for the multi-layer antenna.

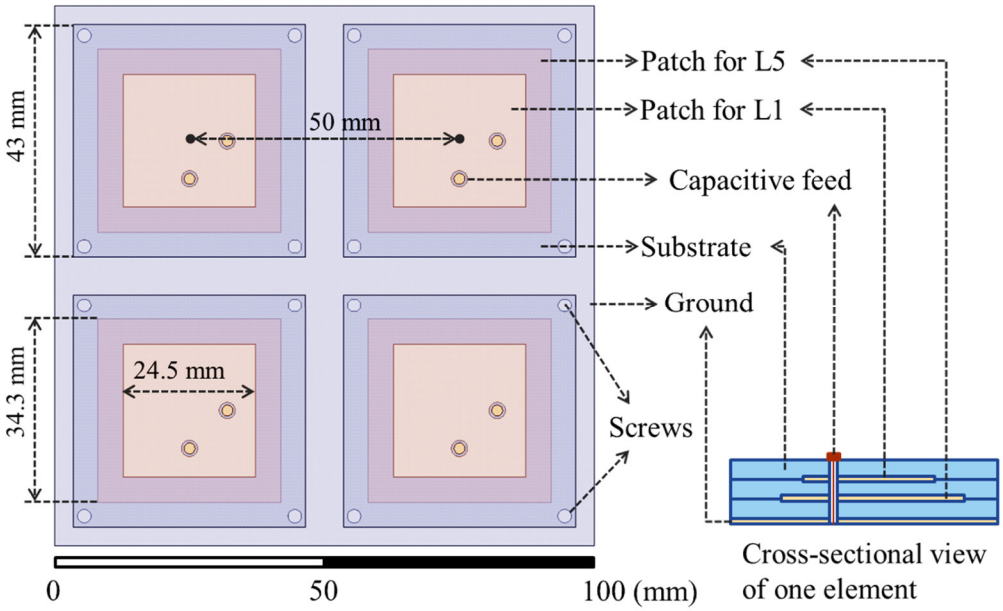

Figure 5.2: A top-view (left) and a side-view (right) of the multi-layer dual-band dual-polarized antenna array (devolved by the German Aerospace Center DLR)

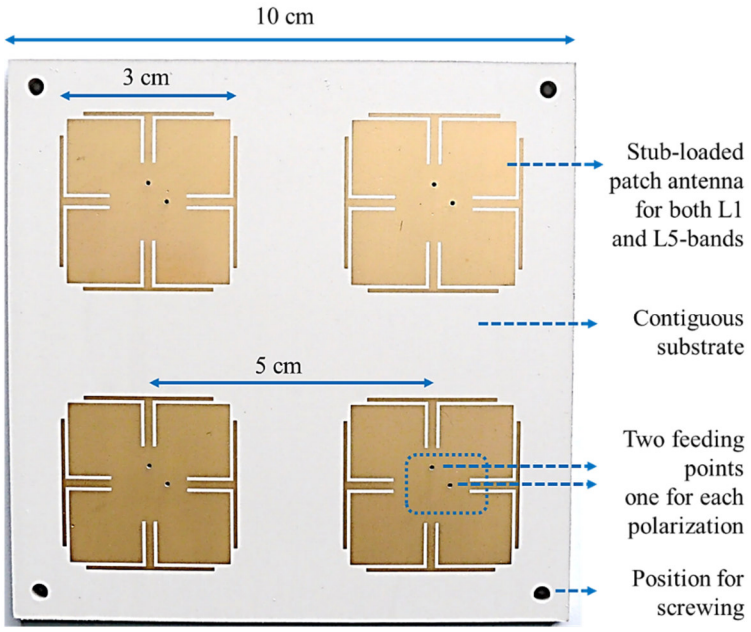

Figure 5.3: A top-view of the single-layer dual-band dual-polarized antenna array, based on stub-loaded patch radiating elements (devolved by TU Ilmenau).

Each array was arranged on an area of 10 cm × 10 cm, making its side-length smaller than 40% of the free-space wavelength λ_0 at the L5-band, and resulting in an element spacing of only $\lambda_0/5$ at the L5-band and $\lambda_0/4$ at the L1-band.

While the multi-layer array is designed with an island structure to reduce the surface-wave mutual coupling between the elements by about 1 dB, as found by numerical simulations, the single layer array uses a common substrate to reduce fabrication costs and ease mass production. Nevertheless, the single layer antenna has a level of mutual coupling smaller by about 1 to 2 dB, due to different parameters such as the smaller substrate thickness, and the less metallic layers.

5.2.2 Array performance with mutual coupling impact

a. Realized gain and radiation efficiency:

Such a degree of compactness, with element spacing of only $\lambda_0/4$ at the L1-band and $\lambda_0/5$ at the L5-band, gives rise to a strong mutual coupling between the radiating elements of both arrays, which measures about -8 dB at the L1-band, and -4 dB at the L5-band, as illustrated in Fig. 5.4.

The strong mutual coupling significantly reduces the realized gain of the antenna elements, in both antenna arrays, from about 2.5 dBi at the L1-band and 4 dBi at the L5-band to about -1 to 0 dBi at both bands; i.e., it reduces the total radiation efficiency of the individual antenna elements by more than 44% at the L1-band, and more than 60% at the L5-band.

b. Array eigenefficiencies:

The influence of mutual coupling can also be seen in terms of eigenefficiencies of the array, i.e., the radiation efficiencies of the array eigenmodes, which is defined for symmetric antenna arrays as following [4, 76, 98]:

If the covariance matrix of an N-element array is $\boldsymbol{R}$, then for a symmetric antenna, $\boldsymbol{R}$ is Hermitian, i.e.,

$$\boldsymbol{R} = \boldsymbol{R}^H \tag{5.1}$$

Hence, the eigen-decomposition of the matrix decomposes it into its eigenvectors and eigenvalues as following:

$$\boldsymbol{R} = \boldsymbol{Q}\,\boldsymbol{\Lambda}\,\boldsymbol{Q}^H, \tag{5.2}$$

where the N columns of the matrix $\boldsymbol{Q}$ form the vector basis $\{v_i, \ldots, v_N\}$of the antenna radiation space, which excite the antenna radiation eigenmodes $\{mode_1, \ldots, mode_N\}$, and Λ is a diagonal matrix that contains the eigenvalues of the covariance matrix, i.e.:

$$\boldsymbol{\Lambda} = diag\,\{\lambda_1, \ldots, \lambda_N\} \tag{5.3}$$

Each element λ_i quantifies the radiation eigenefficiency of the antenna array when its corresponding radiation eigenmode $mode_i$ is excited.

Hence, every antenna pattern is a superpositions of the eigenmode patterns, with a radiation efficiency of:

$$\lambda_{min} < \lambda_1 < \lambda_{max} \tag{5.4}$$

For a four-element antenna array, the eigenmode of maximum efficiency λ_{max} is referred to as the even mode, the eigenmode of minimum efficiency λ_{min} is called the Pi-mode, and the other two modes are called odd-mode 1 and odd-mode 2.

The array eigenmodes were not accessible for far field measurements at this phase of the design, since an eigenmode-based network is needed to excite modes, as described in section 5.5. Hence, the eigenefficiencies were calculated in Matlab using the measured radiation patterns of the antenna elements in the array. This method calculates the upper possible limits of the eigenefficiencies of the fabricated array regardless of the losses introduced by the excitation network.

Calculations revealed a radiation efficiency of about 58% at the L1-band and 24% at the L5-band for the best case, the even mode. The efficiency of the worst case, the Pi-mode, was only about 6% at the L1-band and 2% at the L5-band.

This strong influence of the mutual coupling on the radiation efficiencies of the array forces the need to involve low-loss decoupling techniques, such as the decoupling and matching

networks used in this work, to mitigate the coupling and partially compensate for the reduced radiation efficiencies. More details about this technique are introduced in sections 5.5 and 5.6.

c. Frequency response:

Moreover, numerical simulations of the antenna array revealed a frequency shift of about 30 to 35 MHz at both bands due to the mutual coupling, which was expected as discussed in section 4.6.1.

This shift in frequency was compensated for by simply enlarging all the dimensions of the patch surfaces slightly, and run numerical simulations in the presence of mutual coupling until the dual-band resonance at the required frequencies is achieved.

S-parameter measurements of the fabricated array confirmed that this approach was enough to achieve the resonance with a reflection coefficient below -10 dB at both bands.

d. Cross-polarization coupling:

As described in sections 3.2 and 3.3, the antenna elements were fed at two feeding positions to excite the two orthogonal linear polarizations (LP1, LP2). Measurements of the S-parameters revealed that the multi-layer array featured a cross-polarization decoupling of about 15 dB at the L5-band and 20 dB at the L1-band, between these two ports, as illustrated in Fig. 5.4.

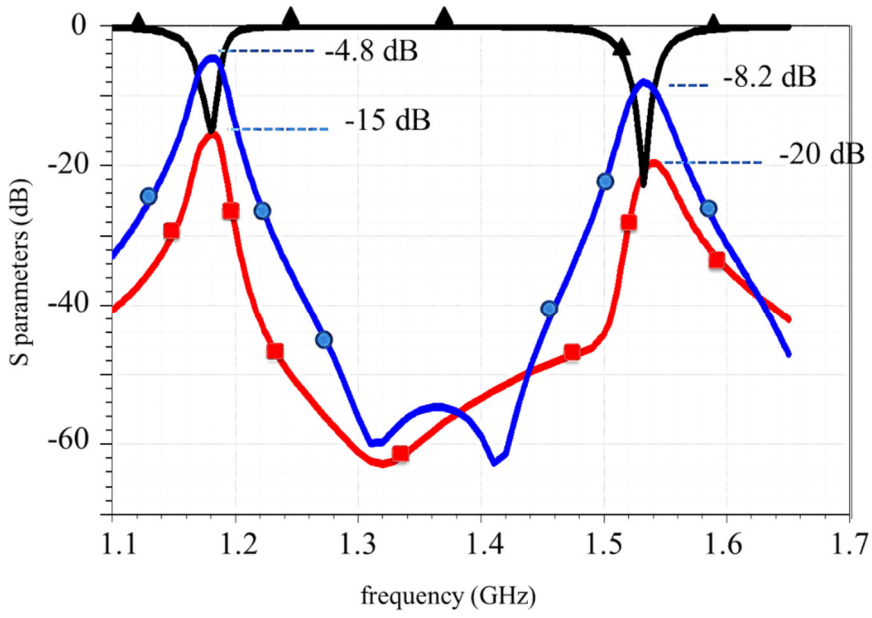

Figure 5.4: Reflection coefficients (black-triangles curve), co-polarized coupling (blue-circles curve), and cross-polarization coupling (red-squares curve), in the multi-layer antenna array.

Likewise, the single-layer array had a cross-polarization decoupling of about 17 dB at the L5-band and 24 dB at the L1-band, as shown in section 3.4.3 in Fig. 3.6.

e. Cross-polarization discrimination:

On the other hand, coupling introduced between the antenna elements decreases the cross-polarization discrimination of each element. Measurements of radiation fields of the single-layer antenna array in the anechoic antenna measurement chamber, and calculations of the cross-polarization discrimination using Matlab revealed a significant reduction of the cross-polarization discrimination of the radiating elements, comparing to the simulated XPD pattern of the single-element, as depicted in Fig. 5.5. Moreover, the 10 dB XPD-beamwidth was reduced from 180° in the single-element mode to about 80° in the array mode, as highlighted also in the figure.

This notable impact of mutual coupling on cross-polarization discrimination adds another reason to use decoupling techniques for the compact antenna array.

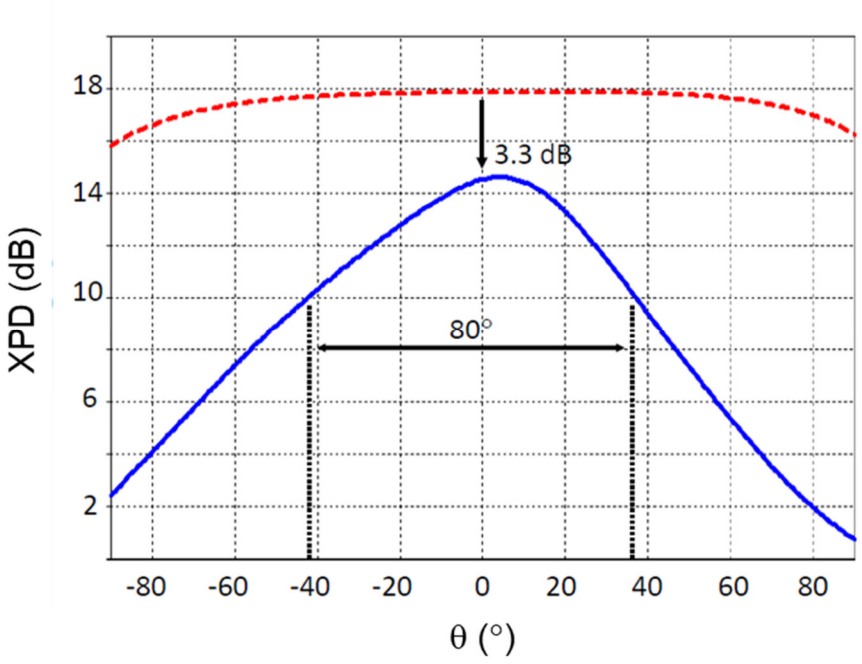

Figure 5.5: Influence of mutual coupling on cross-polarization discrimination of the single-layer GNSS patch antenna element. The figure shows XPD for the single element (red dashed-curve), and of the element in the array (blue curve). 10 dB XPD-beamwidth is highlighted between the two black dotted lines.

5.3 Excitation of the circular polarization

5.3.1 Circuit design

As described before, both the single-layer and multi-layer antenna elements excite two orthogonal linear polarizations. The right hand and left hand circular polarizations were achieved using 90° phase-shifted hybrid couplers, built of the quasi-lumped off-the-shelf integrated circuits QCN-19+ from Mini-Circuits [104], as illustrated in Fig. 5.1. The circuits were added to the bottom layer of the decoupling network board, as described in section 5.1.4.

5.3.2 Cross-polarized coupling

S-parameter measurements revealed that the ports of different polarizations were well decoupled, with a decoupling level larger than 15 dB, before adding the 90° phase-shifted hybrid couplers that generate the circular polarizations.

However, the hybrid couplers operate perfectly for 50 Ω input and output impedances, which is not easy to achieve for dual-band GNSS antennas, where the two bands are too close. Practically, optimization of the designed antenna elements resulted in an output impedance between 30 Ω and 45 Ω, which deteriorates the performance of the couplers, especially at the L5-band, where the impedance was about 30 Ω, resulting in a notable coupling level of about -6 dB between the exited RHCP and LHCP radiation modes.

Nevertheless, due to its source of mismatching, cross-polarized coupling was reduced later by tuning dual-band matching networks, introduced directly after the decoupling networks, as discussed in sections 5.5 and 5.6. Coupling levels were reduced from -3 dB to -6 dB between the RHCP and LHCP Pi modes of the antenna array, and from -7 dB to -12 dB between the RHCP and LHCP even modes of the antenna array.

The other possible solution of adding another layer of matching networks directly after the antennas and before the hybrid coupler was ignored, to avoid adding more design complexity and Ohmic losses.

In general, it is important either to generate the circular polarizations directly at the antennas, which is quite challenging for dual-band antennas, or to match the linear polarizations very well, which is also not easy for too close bands such as with GNSS.

A further study showed the same behavior when an equivalent circuit of transmission lines was used instead of the integrated circuit, which confirms that the reason behind this problem is mismatching, and not a weakness in the off-the-shelf circuits.

5.4 Mitigation of the mutual coupling - State-of-the-art

As mentioned in section 5.2.2, measurements of the antenna array revealed a strong mutual coupling of -4 to -8 dB between the antenna ports of identical polarization, which reduces the radiation efficiencies of the array eigenmodes. This poor efficiency reduces the feasibility of the modes, and hence decreases the diversity gain of the array, or in other words, it limits the use of the four-element compact array, resulting in a system performance comparable to that of a three-element array with $\lambda_0/2$ element spacing. This limitation justifies the importance of using decoupling techniques to decouple the co-polarized ports, and restore part of the radiation efficiency.

There are several approaches to reduce the mutual coupling in compact antenna arrays. Mutual coupling can be reduced at the level of the radiating elements using techniques such as electromagnetic band-gap structures [105-110], and frequency-selective surfaces [111-115]. Some techniques suppress the surface wave coupling by optimizing the antenna dimensions [92, 116], grooving the dielectric [117], or covering the patch by additional dielectric layers [118]. However, these techniques come at the cost of increasing the design complexity and the fabrication costs.

Mutual coupling can also be reduced by changing the structure of the antenna array, e.g., by using spatial tilting [79, 98, 119], which converts the planar structure of the antenna into a 3D structure. This approach, however, increases the fabrication complexity, and reduces the antenna directivity.

Furthermore, coupling can also be reduced at the level of the feed network, using solutions such as eigenmode-based decoupling and matching networks as explained in this thesis.

5.5 Design of the eigenmode-based decoupling networks

Since coupling affects the matching efficiencies of the array more than the radiation efficiencies, as seen in section 4.6.1 in Fig. 4.23, the approach of eigenmode-based decoupling and matching network solves the problem of enhancing the poor eigenefficiencies of the compact array by matching the eigenmodes of the array.

However, to match the eigenmodes of a compact array, it is needed to have access to them at first. Hence, the approach separates the problem into a decoupling stage, and a matching stage. At the decoupling stage, a network is used to excite the eigenmodes of the array, which are decoupled in nature, due to the orthogonality, and therefore the network is called a decoupling network [76, 77, 120, 121]. Then, at the matching stage, separate matching networks are used to match each of the extracted eigenmodes, resulting in enhancing their efficiencies, and eventually the array diversity.

The usability of the decoupling and matching networks was proven in previous works for compact single-band single-polarized GNSS antenna arrays [4, 15, 49, 122]. Therefore, and to keep the fabrication costs at low levels, this approach will be extended in this work for compact dual-band dual-polarized receivers.

5.5.1 Circuit design

Based on the eigenmode analysis described in section 5.2.2, both the multi-layer and the single-layer four-element antenna arrays presented in Fig. 5.2 and Fig. 5.3 have four eigenmodes with eigenvectors as stated in Table 5.1, assuming symmetric ideal structures.

Table 5.1: The array eigenmodes and their relevant eigenvectors of the studied four-element patch antenna arrays, assuming symmetric ideal structures.

Eigenmode	Eigenvectors	Excitation: same amplitude of 1, and different phases at the feeding ports of the antenna elements			
		phases at element1	phases at element2	phases at element3	phases at element4
Even mode	$v_1 = [+1, +1, +1, +1]^T$	0°	0°	0°	0°
Odd mode 1	$v_2 = [+1, -1, -1, +1]^T$	0°	180°	180°	0°
Odd mode 2	$v_3 = [-1, -1, +1, +1]^T$	180°	180°	0°	0°
Pi-mode	$v_4 = [-1, +1, -1, +1]^T$	180°	0°	180°	0°

The design starts with a single 180° phase-shift hybrid coupler [123, 124], which extracts the orthogonal even and Pi-modes of a two-element antenna array, as illustrated in Fig. 5.6, by simply using different lengths of the transmission lines to shift the phases of the signals to achieve:

$$\text{Even mode} = \text{Ant.1+Ant.2} \tag{5.5}$$

$$\text{Pi-mode} = \text{Ant.2-Ant.1} \tag{5.6}$$

where Ant.1 and Ant.2 are the signals at first and second antennas, respectively.

Then, for the four-element antenna arrays, a four-input four-output eigenmode-based decoupling network that excited the array eigenmodes listed in Table 5.1 can be designed using four of the 180° hybrid couplers, cascaded as shown in the block diagram in Fig. 5.7, to feed the four antennas with the relevant eigenvector of each eigenmode.

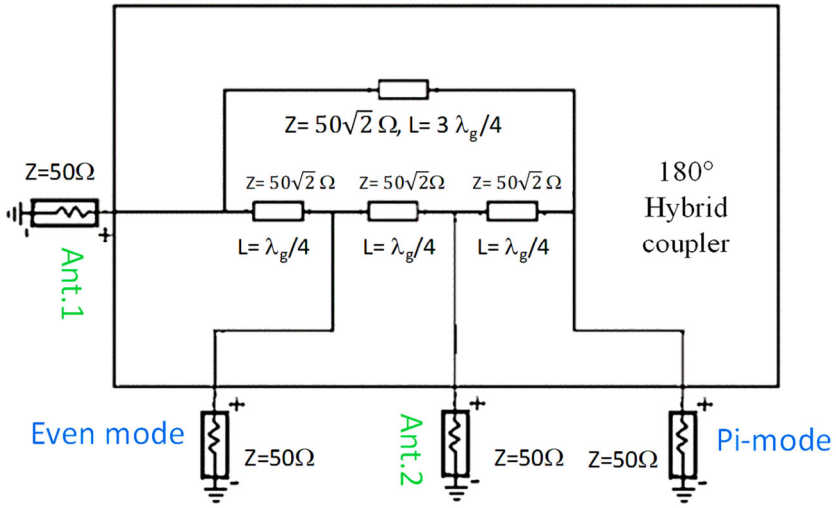

Figure 5.6: The concept a single 180° phase shift hybrid coupler. Z is the characteristic impedance of a transmission line or a port, and L is the length of a transmission line.

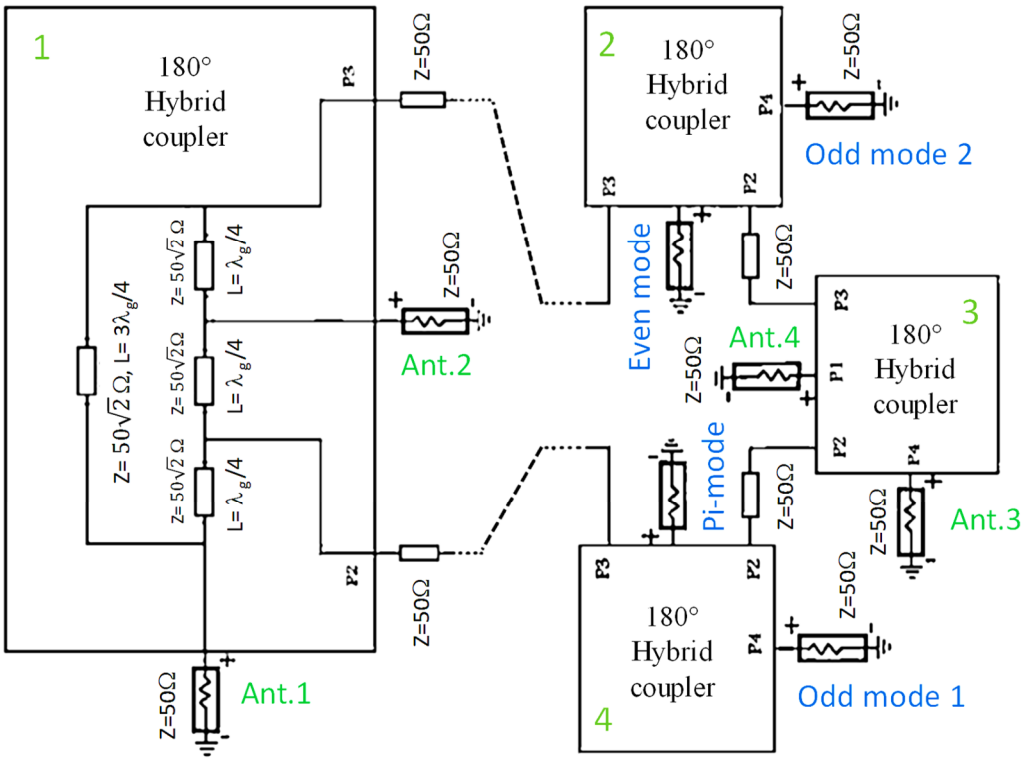

Figure 5.7: The block diagram of one decoupling network designed based on four 180° hybrid couplers. Z is the characteristic impedance of a transmission line or a port, and L is the length of a transmission line.

The decoupling networks were designed using stripline technology, as depicted in Fig. 5.8. The four ports related to each polarization were decoupled separately, using one eigenmode-based decoupling network. Hence, two decoupling networks were needed for the antenna array, one to decouple its RHCP ports, and one for the LHCP ports.

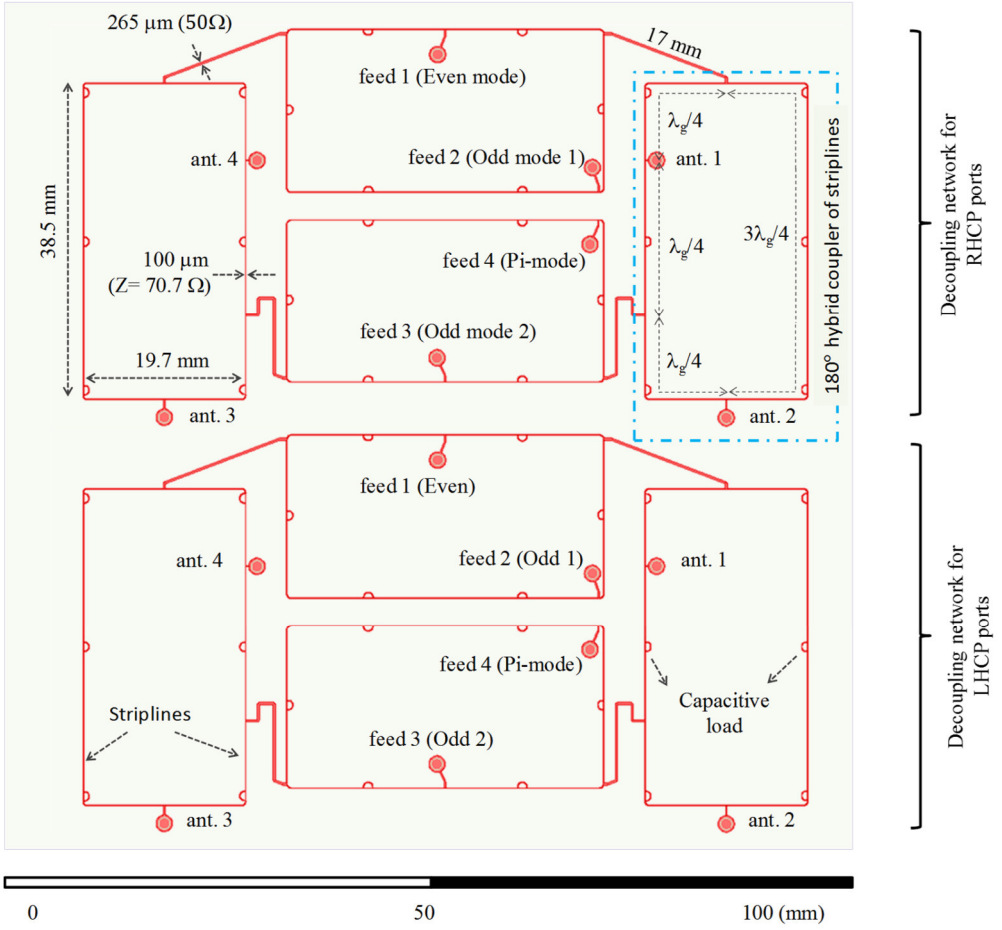

Figure 5.8: The 10 cm x 10 cm stripline-circuit consisting of two eigenmode-based decoupling networks, designed in Keysight Advanced Design System, using Rogers 3010. The antenna elements, related to each polarization, will be connected to the antenna ports 1..4, and the eigenmodes are extracted at the feed ports 1..4.

It was also possible to design decoupling networks for the two linear polarizations excited by the antenna, instead of the RHCP and LHCP. This approach is theoretically equivalent, and it eliminates the need for the hyprid-couplers that excite the circular polarizations, and hence reduces the power losses introduced by them, and avoids the problem of coupling between their outputs. However, since GNSS signals are ideally RHCP, this approach demands the use of both linear polarizations for beamforming algorithms, which increases the complexity of both the RF front-end and the digital receiver. On the contrary, the approach of exciting and decoupling the RHCP and LHCP modes allows beamforming

algorithms to use only the RHCP ports, if sufficient, or additionally selected LHCP ports, depending on feasibility and receiver capability.

The design of the circuit was performed and optimized using the Momentum 3D EM Simulator of Keysight Advanced Design System (ADS) [125].

The adhesive material used to glue the substrate layers together changes the dielectric constant of the substrate, resulting in changing the performance of the stripline-based decoupling networks. However, it was found based on simulations in Momentum that this influence can be mitigated by loading the hybrid-couplers of the networks with capacitive loads in the shape of half circles of 0.5 mm radius, as depicted in Fig. 5.8.

The Rogers 3010 with a dielectric constant of 10.2 and a thickness of 0.635 mm was chosen as the circuit substrate. The high permittivity was selected to improve the compactness, and thus to allow for the placement of the two decoupling networks in the one layer of 10 cm x 10 cm area. The adhesive material Prepreg RO 4450F is used to stick the layers together.

The circuit was integrated in a multilayer printed circuit board, as illustrated in Fig. 5.9, and Fig. 5.10, to ease the integration with the antenna array, and later with the following circuits in the RF front-end. The bottom layer of the printed circuit board contains the calibration and the matching circuits, which will be described later. The entire board is referred to as the decoupling and matching (DMN) board.

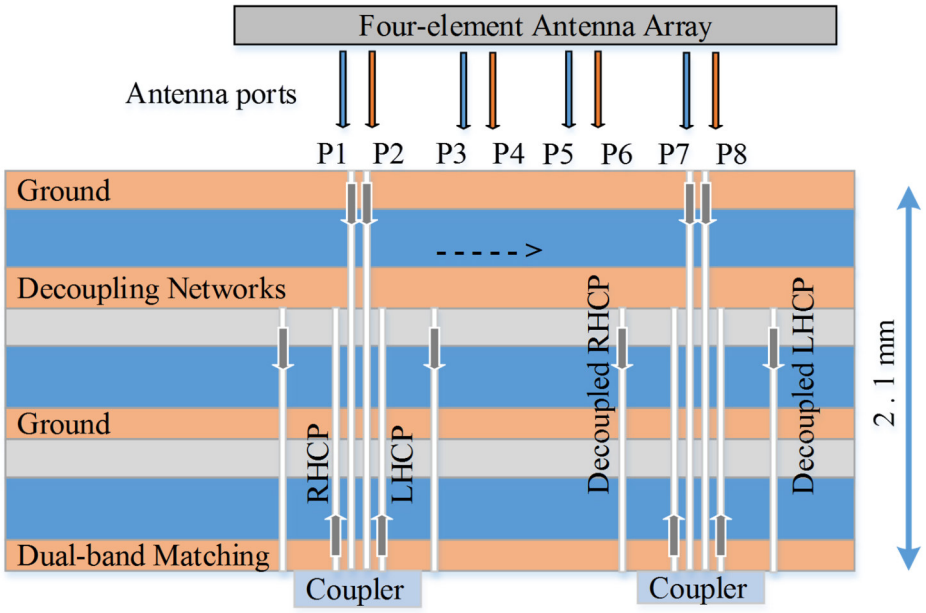

Figure 5.9: A side-view sketch of DMN board layers, brown: metallization, blue: dielectric substrate, gray: adhesive material.

The printed circuit board was designed and fabricated for both the single-layer and the multi-layer antenna arrays, with layout modifications to fit with each antenna.

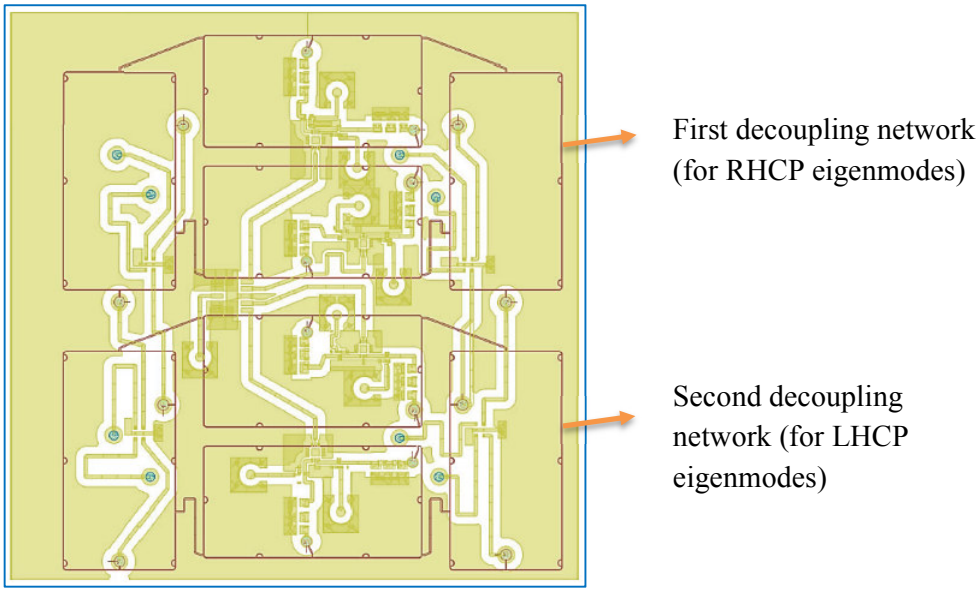

Figure 5.10: A transparent top-view of the 10 cm x 10 cm multilayer DMN board, highlighting the layer of the two decoupling networks (in red), the layer of matching and calibration circuits (yellow), and the vias of the antenna ports (blue circles).

Designs were modified, fabricated, and tested several times between 2014 and 2016, to enhance the decoupling and the matching parameters, by tuning dimensions of the striplines, and to ease the assembly of the calibration and matching circuits. Figure 5.11 shows the top-view of one fabricated board. The figure highlights the antenna inputs, the decoupling network inputs and outputs, and the layout of the matching and calibration circuits.

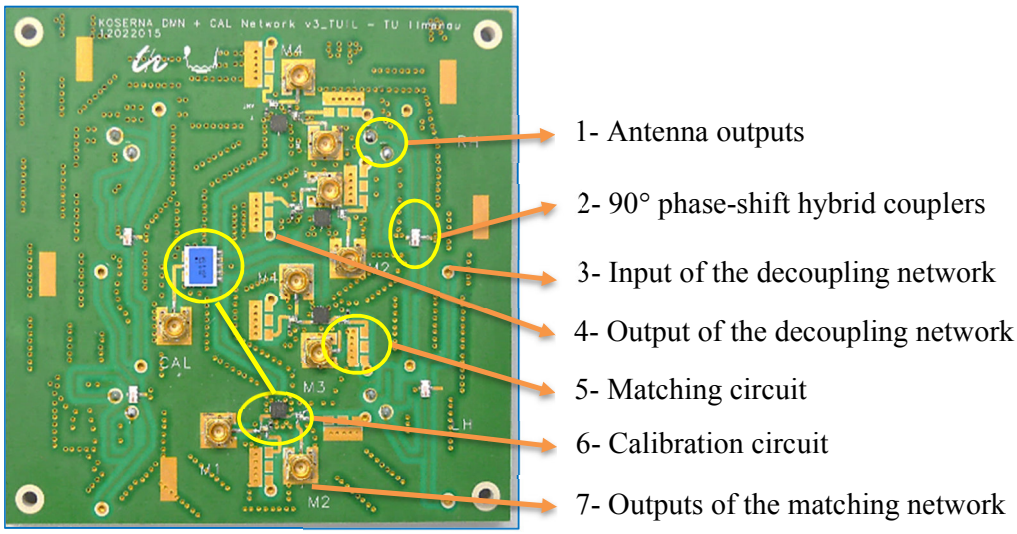

Figure 5.11: Top-view of the fabricated DMN board, with instances of the main functions and ports highlighted. Numbers represent the order of the functions in the signal flow.

Quality of the eigenmode excitation:

S-parameters of the fabricated decoupling networks were measured in order to check if the excitation of the eigenvectors was achievable as listed in Table. 5.1. Results stated in Table 5.2 compare the theoretical excitation phases required to excite the eigenmodes with the measured ones, at the L1-band. The table shows an average shift of about ±13°, due to fabrication limitations, which can be minimized by tuning the lengths of the feeding paths.

Table 5.2: Theoretical (theo.) and measured (msr.) phases between the decoupling network outputs and the related four ports of the antenna array

Array port	Phase							
	Odd mode 1		Pi-mode		Odd mode 2		Even mode	
	theo.	msr.	theo.	msr.	theo.	msr.	theo.	msr.
1	180°	189°	180°	184°	0°	-13°	0°	-12°
2	0°	-13°	0°	-13°	0°	-17°	0°	-19°
3	0°	-1°	180°	183°	180°	172°	0°	-14°
4	180°	196°	0°	29°	180°	168°	0°	-20°

The quality of the eigenmode excitation, and hence the quality of decoupling, can be concluded from computing the non-orthogonality ratio between the actual excitation vectors provided by the network, as following:

Since the scalar product between two vectors $\boldsymbol{a}$, $\boldsymbol{b}$ is defined by:

$$\boldsymbol{a}.\boldsymbol{b} = |\boldsymbol{a}||\boldsymbol{b}|\cos(\theta), \tag{5.7}$$

where θ is the phase between $\boldsymbol{a}$ and $\boldsymbol{b}$, then it is possible to use the amount $\cos(\theta)$ as a measure of non-orthogonality level between $\boldsymbol{a}$ and $\boldsymbol{b}$.

A similar measure can be written for the case of feeding networks, to calculate the non-orthogonality ratio between two excitation vectors, as following:

$$\gamma_{ij} = \frac{1}{N}\sum_{k=1}^{N} \cos(\theta_{ik} - \theta_{jk}), \tag{5.8}$$

where γ_{ij} represents the non-orthogonality between the excitation vector v_i and the excitation vector v_j , N is the number of components, θ_{ik} is the k^{th} phase component of the excitation vector v_i.

This function satisfies that $\gamma_{ij} = 0$ for any two eigenvectors listed in table 5.1. For example, if $v_1 = [1,1,1,1]^T, v_2 = [1,-1,-1,1]^T$, then:

$$\gamma_{12} = \frac{1}{4}(\cos(0) + \cos(180) + \cos(180) + \cos(0)) = 1 - 1 - 1 + 1 = 0$$

It also satisfies $\gamma_{ii} = 1$ which means that any excitation vector v_i is fully non-orthogonal to itself.

Accordingly, Table 5.3 shows the non-orthogonality between the measured excitation vectors. Calculations reveal that the largest non-orthogonality level is about only 6.7%, which gives an indication of the quality of the fabricated decoupling network.

However, the decoupling levels can only be measured after integrating the DMN board with the antenna, which is performed in the following section

Table 5.3: Correlation between the excited (Ex.) modes at the outputs of the decoupling network

Eigenmodes	Ex. Odd mode 1	Ex. Pi-mode	Ex. Odd mode 2	Ex. Even mode
Ex. Odd mode 1	100 %	0.6 %	0.9 %	5.5 %
Ex. Pi-mode	0.6 %	100 %	6.7 %	6.7 %
Ex. Odd mode 2	0.9 %	6.7 %	100 %	0.3 %
Ex. Even mode	5.5 %	6.7 %	0.3 %	100 %

5.5.2 Integration with the antenna array

The DMN board was connected first to the multi-layer antenna array, using surface mount SMA connectors, as illustrated in Fig. 5.12.

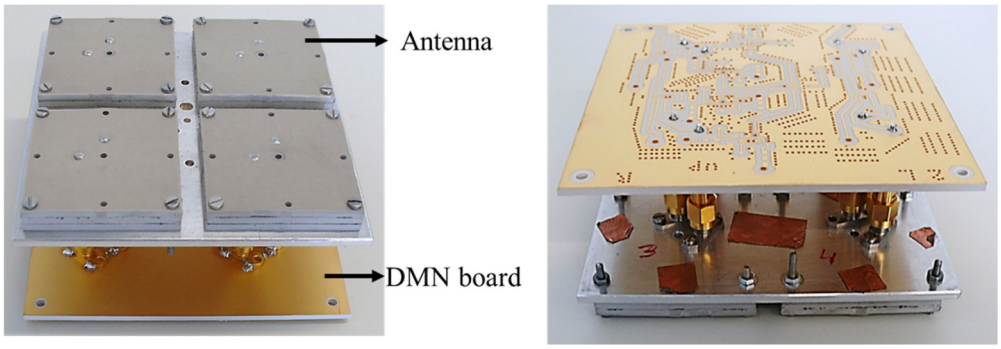

Figure 5.12: Top-view (left), and bottom-view (right) of the multi-layer antenna array connected to the DMN board with 50Ω-SMA connectors.

Four final-version DMN boards were designed and fabricated in December 2015 and January 2016; two for each antenna array. The DMNs boards were assembled, and then glued with their antenna as shown in Fig. 5.13 and Fig. 5.14.

While the two antenna systems (antenna + DMN board) were electrically comparable, the system with the single-layer array featured a smaller thickness of 7.28 mm instead of 12

mm, resulting in a smaller weight, and thus a more stable adhesion between the antenna and the DMN board. Moreover, it costs less as it uses less material.

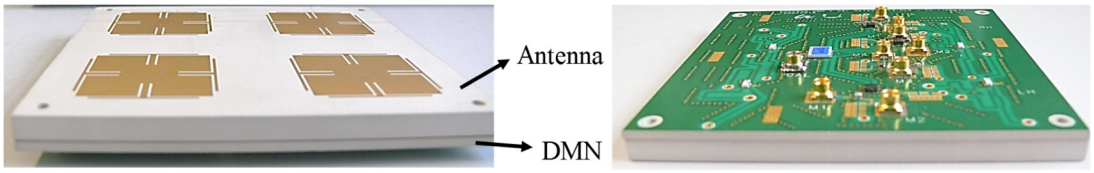

Figure 5.13: Top-view (left), and bottom-view (right) of the single-layer antenna array integrated with the DMN board. Total thickness: 7.28 mm

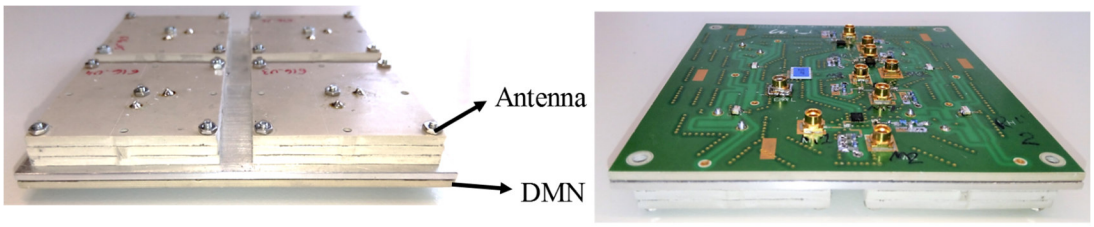

Figure 5.14: Top-view (left), and bottom-view (right) of the multi-layer antenna array integrated with the DMN board. Total thickness about 12 mm.

The evaluation of the decoupling networks was performed after integration with the antennas, by measuring the mutual coupling coefficients between the decoupling network outputs. S-parameter measurements revealed a very small coupling level of below -18 dB at the L5-band and below – 20 dB at the L1-band between any two outputs of the RHCP decoupling network or the LHCP decoupling network, for both antenna systems. Fig. 5.15 shows the mutual coupling levels between the RHCP decoupling network outputs of the single layer antenna system.

These very small coupling values emphasize the very good performance introduced by the decoupling networks, as the mutual coupling between the original antenna elements was about -4 dB at the L5-band and -8 dB at the L1-band. The DMN design and the results were published in [69].

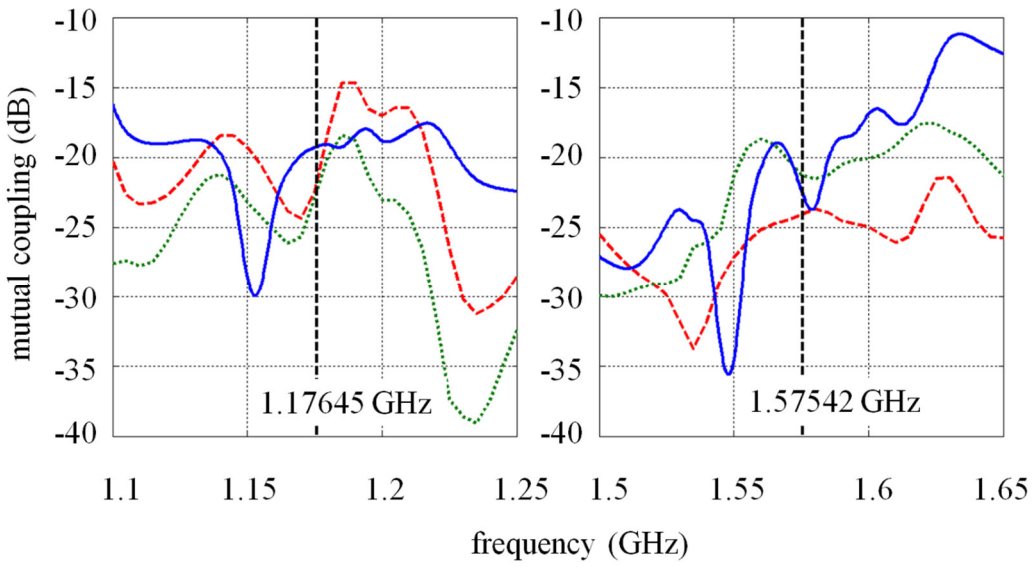

Figure 5.15: Measured mutual coupling between the outputs of the RHCP decoupling network of the single-layer antenna system. The curves show the coupling between the first odd mode and: the second odd mode (dashed red curve), the even-mode (dotted green curve), and the Pi-mode (blue curve).

5.6 Design of the dual-band matching networks

5.6.1 Introduction

The eigen-mode decoupling network, in its best case when it introduces no losses to the circuit, is just a transformation system that converts the coupled radiation modes of the antenna elements into a new set of decoupled modes, which are the eigenmodes of the array. Hence, the influence of mutual coupling on reducing the radiation efficiencies of the antenna elements is reflected again in deteriorating the input impedance of the higher-order eigenmodes of the array, which results in poor reflection efficiencies at the eigenmode ports, and hence poor eigenefficiencies.

In other words, it is possible at this point to reduce the mutual coupling impact by re-matching the eigenmodes of the array. However, due to the losses introduced by the decoupling network, only part of the eigenefficiencies can be restored. Additionally, the need to match the eigenmodes at the two close bands L1 and L5 may rise the need to accept trade-off solutions where some notable mismatching is still introduced, especially for the higher-order eigenmodes which are usually heavily mismatched.

5.6.2 Design approach

So, at this stage, the RHCP and LHCP eigenmodes of the array were matched using dual-band lumped-element matching circuits, added at the outputs of decoupling network. Lumped elements were used, instead of distributed lines, to enable measurement-based tuning, and to save the large area needed by distributed lines for the other circuits that should be placed on the compact board, namely the calibration circuit and the circular-polarization excitation circuits. Eight matching circuits were designed for the four RHCP and four LHCP eigenmodes.

Matching circuits with only two elements could be enough for the matching of single-band ports. Circuits with more elements give better matching in the case of dual-band ports. However, the more elements used the more Ohmic losses and design complexity introduced, and therefore a trade-off number of five lumped elements was selected for each matching circuit.

Considering that the design of the matching circuits is a critical task, which determines the performance of the entire system, intensive simulations and measurement-based optimizations were performed, in order to match the system at both bands, and overcome the challenging high sensitivity of the system at each band to the optimizations at the other band.

5.6.3 Optimization and measurement results

Optimization strategy:

Several approaches can be followed during the optimization process. First, each port can be matched alone, regardless of its influence on the others. This will not work in the presence of coupling, since matching of one element will disturb the already matched elements. However, this partially works in the presented case, due to the decoupling provided by the decoupling network.

On the other hand, matching of one mode in RHCP/LHCP decoupling network may disturb the matching of the similar mode in the other LHCP/RHCP decoupling network, due to the cross-polarized coupling introduced by the hybrid couplers, as discussed in section 5.3.2. This coupling cannot be ignored as it reduces the polarization purity of the eigenmodes, and thus affects the performance of the dual-polarized robustness algorithms.

Based on this discussion, the optimization process was implemented to find the best matching circuit elements for every two cross-polarized coupled ports, jointly and separately from the other ports, i.e., for the RHCP and LHCP even modes, the RHCP and LHCP first odd modes, the RHCP and LHCP second odd modes, and finally the RHCP and LHCP odd modes. Simulations and measurements proved the suitability of this approach comparing to the other approaches.

However, it is still possible theoretically to implement a full design optimization process that tries to match every port and decouple all of them at the same time, but with the fifty elements to tune and at least twelve goals to target, this becomes impractical even in simulations.

Simulation-based optimization:

Simulations of the matching circuits where performed in ADS based on the measured S-parameters of the antenna with the two decoupling networks. Due to the complexity of the design, the ADS-built-in genetic optimization algorithm and the ADS-built-in least-path random optimization algorithm where used, separately, to find the best solution. The algorithm which gave the best solution, with smallest error, for each case was adopted for that case. The optimization goals were set to get:

- Goal 1: -10 dB reflection coefficients for all eigenmodes at both frequency bands.
- Goal 2: -10 dB cross-polarization coupling.

Moreover, it was also noticed that adding the matching circuits reduces the decoupling between the modes, since decoupling levels were measured at first place using 50 Ω cables and connectors directly connected to the decoupling networks, while the matching circuits added to series here provide impedances slightly different from 50 Ω. Therefore, the process of optimizing the matching circuits had to add a new condition of:

- Goal 3: keeping coupling levels between any two outputs of each decoupling network below -10 dB at both frequency bands.

A snapshot of the simulation-based optimization process is illustrated in Fig. 5.16. The figure highlights the approach of finding the best matching circuit for every two cross-polarized coupled ports, jointly and separately from the other ports. It shows also an example of two matching circuits, where each one consists of five lumped elements.

ADS simulations proved the possibility of -10 dB matching for all modes, including the higher-order modes, while keeping coupling levels below -10 dB. However, optimization of the worst-case eigenmode, the Pi-mode, was so challenging, and finally a narrow bandwidth of only 2 MHz at the L1-band was achieved, with a cross-polarization coupling of -6 dB.

Nevertheless, simulation-based circuits showed poor performance when assembled to the system, mainly due to the parasitic effects, which is hard to be measured or modelled in the design. Even though, all microstrip lines in the circuit were accurately involved in the simulation design, and the manufacturer S-parameters of the lumped elements (mainly, from Murata for capacitors [126], and Coilcraft for inductors [127]) were used instead of the standard elements of ADS library, notable differences between ADS simulations and measurement results were revealed. This was not the case for the decoupling networks were no lumped elements were used, which confirms the known limitations the RF design environments have in modelling of lumped elements and parasitic effects.

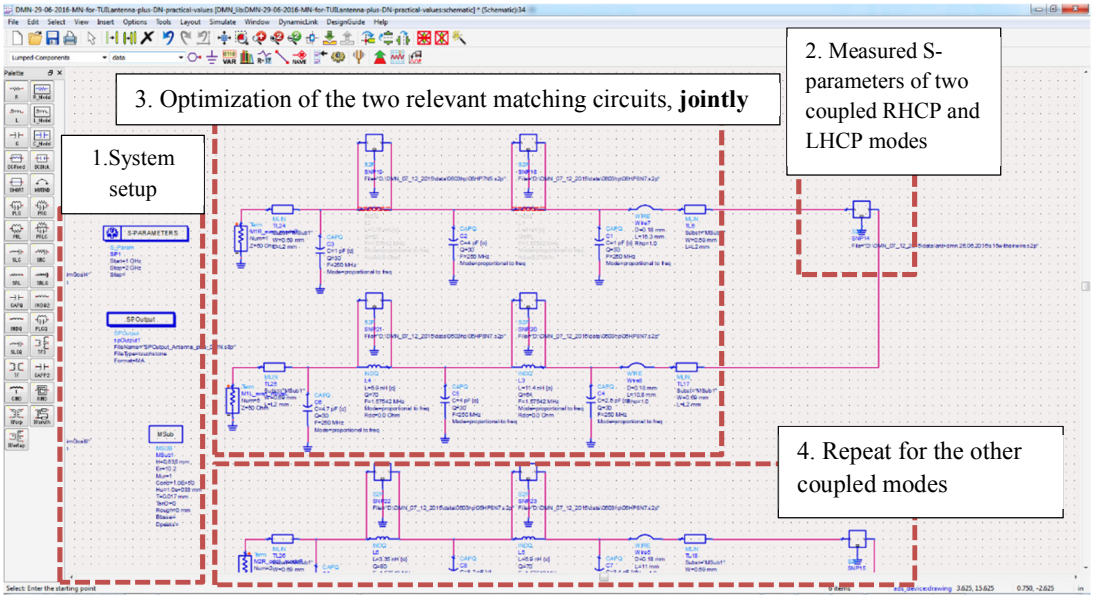

Figure 5.16: A snapshot of part of the simulation-based design and optimization process of the matching networks in ADS. The figure highlights the approach of finding the best matching circuit for every two cross-polarized coupled ports, jointly and separately from the other ports. The figure depicts also the schematic of the relevant matching circuit consisting of five lumped elements, and the modeling of the measurement cables.

Measurement-based optimization:

Considering the limitations found for the simulation-based approach, further measurement-based optimization of the matching circuits was needed. The same optimization strategy was followed here, with optimizing the matching network for every two cross-polarized coupled ports, jointly and separately from the other ports.

However, besides the critical and demanding work of repeated soldering, measuring, and removing the elements, which limits the scanned space of values compared to simulations, measurement-based optimization was also limited by the discrete available values of the lumped elements, in addition to the influence of parasitic effects. Therefore, the values achieved by simulation-based optimizations could not be reached here.

Matching networks optimized for the multi-layer antenna achieved the following results:

- -12 to -15 dB reflection coefficient for the even mode
- -9 to -11 dB for the odd modes
- Poor matching of -4 to -6 dB for the Pi-mode

Matching networks optimized for the single-layer antenna achieved better results of:

- -12 to -15 dB reflection coefficient for the even mode
- -9 dB or below for all the other modes including the Pi-modes

This is probably because of the thinner substrate the single-layer antenna has, which results in smaller surface-wave mutual coupling.

Measurements of the coupling levels after matching networks revealed a coupling level below -15 dB between any two eigenmodes of the array, at both bands, and for both polarizations. Moreover, measurements revealed that, with the use of the decoupling and matching network, the angular width of XPD > 10 dB was increased from about 80° to about 110°. This result is of great importance, since it proves the feasibility of the decoupling and matching networks to partially restore the polarization purity degraded by the mutual coupling.

Further discussion:

A- Matching of the best case (the even modes):

The need for matching the even mode is not imperative in general single-band applications, where the antenna element usually supports almost 50 Ω output impedance to the following 50 Ω circuits [80]. This changes in dual band applications due to the difficulty of providing the 50 Ω output impedance at both bands, as mentioned in section 3.4.2.

However, the optimization process quickly found a solution which matches the RHCP and LHCP even modes while reserve acceptable decoupling between them as illustrated in Fig. 5.17.

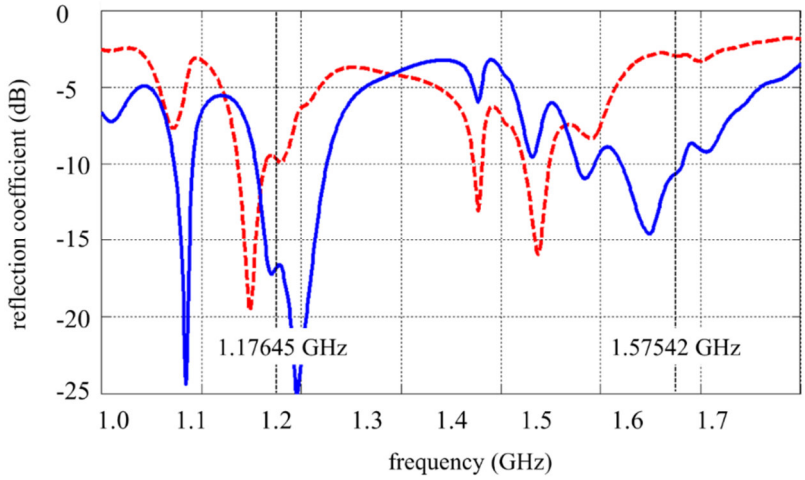

Figure 5.17. Measured reflection coefficient of the RHCP even mode of the antenna system (antenna plus decoupling network) without matching circuit (dashed red curve) and with matching circuit (blue curve).

B- Matching of the worst case (the Pi-modes):

The Pi-mode has the lowest radiation efficiency among the array eigenmodes. Furthermore, its four beams (for a four-element array) are tilted away from the zenith towards low elevations where the polarization purity of the single element is significantly reduced, as

discussed in section 5.2.2. This gives rise to a strong cross-polarization coupling between the RHCP and the LHCP Pi-modes, which is boosted again by the hybrid couplers due to mismatching, as discussed in section 5.3.2. Therefore, the cross-polarization coupling can hardly be reduced below -6 dB in the matching process, even in the simulation-based optimization, especially at the L5-band where mutual coupling is stronger.

5.6.4 Realized eigenmode radiation patterns

The radiation patterns of the RHCP and LHCP eigenmodes of the antenna arrays where measured in the anechoic antenna measurement chamber after integrating with the decoupling and matching network. Far field realized gain patterns of the eigenmodes of the single-layer antenna array at the L1-band, are illustrated in Fig. 5.18. The even mode has a single beam directed towards the zenith. Each of the two odd modes has two beams tilted to about 30° in elevation. The pi-mode should theoretically have four beams. However, due to its poor efficiency, the measurements could not clearly reveal the four beams. The relevant measured realized gains of the eigenmodes as listed in Table 5.4.

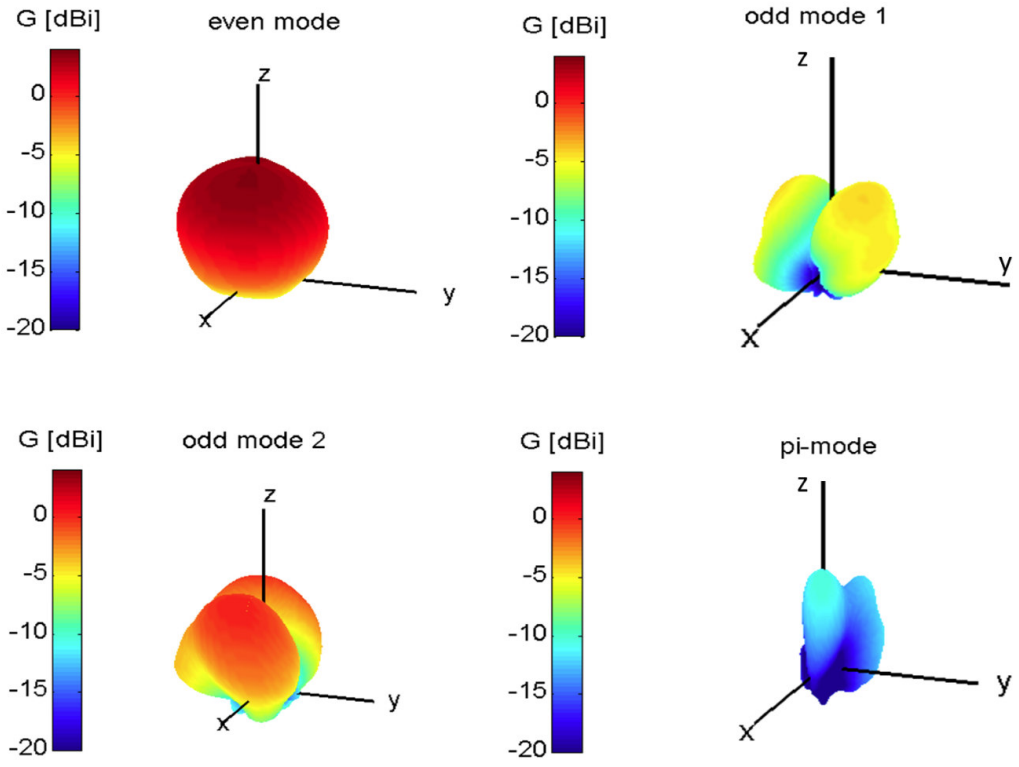

Figure 5.18: 3D-plots of the far field realized gain patterns of the RHCP/LHCP eigenmodes of the single-Layer antenna array, at the L1-band, after decoupling and matching.

Table 5.4: Realized gains of the RHCP/LHCP eigenmodes of the single-layer antenna array after decoupling and matching.

	Realized gain at the L1-band	Realized gain at the L5-band
Even mode	7 dBi	4 dBi
Odd mode 1	0 dBi	-1 dBi
Odd mode 2	2 dBi	0 dBi
Pi-mode	-2 dBi	-5 dBi

Apparently, the higher-order modes have smaller realized gains at the L5-band, due to the stronger mutual coupling. The multi-layer antenna features similar patterns with slightly different gain values.

The eigenefficiency of the best case, the even mode, was enhanced from 58% at the L1-band and 24% at the L5-band, before decoupling and matching networks, to about 65% at the L1-band and 48% at the L5-band after decoupling and matching. The efficiency of the worst case, the Pi-mode, was enhanced from 6% at the L1-band and 2% at the L5-band, to about 10% at the L1-band and 4% at the L5-band after matching.

These eigenmode radiation patterns determine the system performance. An array-based system that uses only the even mode performs well mostly at the zenith, which is similar to the case of the single element system, but probably with higher gain. In contrast, a system that uses the higher order modes shifts its coverage area to lower elevations. Obviously, a system that covers both the zenith and low elevation directions needs to use a superposition of several radiation modes. This is to be discussed in detail in the next chapter.

5.7 Design of calibration circuits

The proposed receiver was empowered with a calibration network[1] built of eight directional couplers, to enable the digital receiver to calibrate the RF output levels after matching. The couplers were also driven by eight identical calibration signals, to enable off-line calibration. These eight signals were achieved from one calibration signal divided equally using two stages of power dividers.

The calibration signal was generated and up-converted to each of the two RF frequency bands in a separate signal-generator board2, as illustrated in Fig. 5.19.

The calibration network was miniaturized using off-the-shelf components, and then integrated with the DMN board as mentioned in section 5.5.1, and as depicted in Fig. 5.11. Insertion loss measurements found that the calibration circuit introduced an insertion loss below 0.5 dB.

[1] Designed by Dr.-Ing. Safwat Irteza who was at TU Ilmenau. Later, Dr.-Ing. Kurt Blau from TU Ilmenau and me were responsible for assembly, testing, and system integration.
[2] Designed by Dr.-Ing. Kurt Blau.

5.8 RF-IF front-end

5.8.1 Preamplifier stage[3]

The resulting dual-band decoupled, matched, and calibrated LHCP and RHCP modes were then amplified in a pre-amplifier stage of eight low-noise amplifiers, and then separated into L1-band and L5-bands using eight frequency diplexers. These functions were integrated in one PCB, depicted in Fig. 5.20.

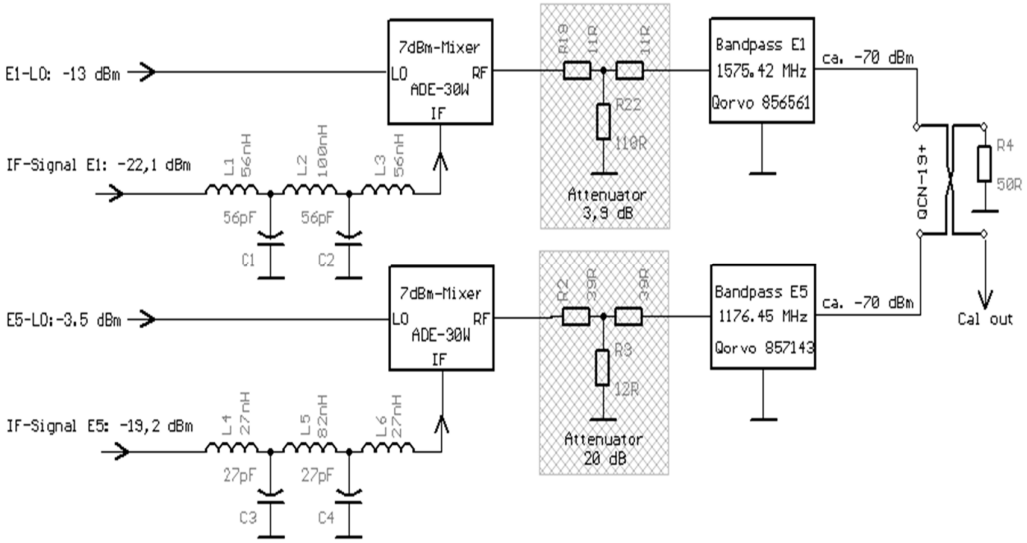

Figure 5.19: Realization of the calibration signal-generator at both the L1/E1-band and the L5/E5a-band, consisting of two RF signal generators at both bands, two IF-signals, two mixers, two attenuators, and two bandpass filters.

Sixteen signals were achieved at the end, eight RHCP and eight LHCP, as stated in section 5.1. However, due to the aforementioned digital receiver limitations, only the following 12 channels where passed to the following circuits:

a. Four L1/E1 channels, with RHCP.
b. Four L1/E1 channels, with LHCP.
c. Four L5/E5a channels, with RHCP.

[3] Designed mainly Dr.-Ing. Irteza. Later, Dr.-Ing. Kurt Blau and me were responsible for testing and system integration.

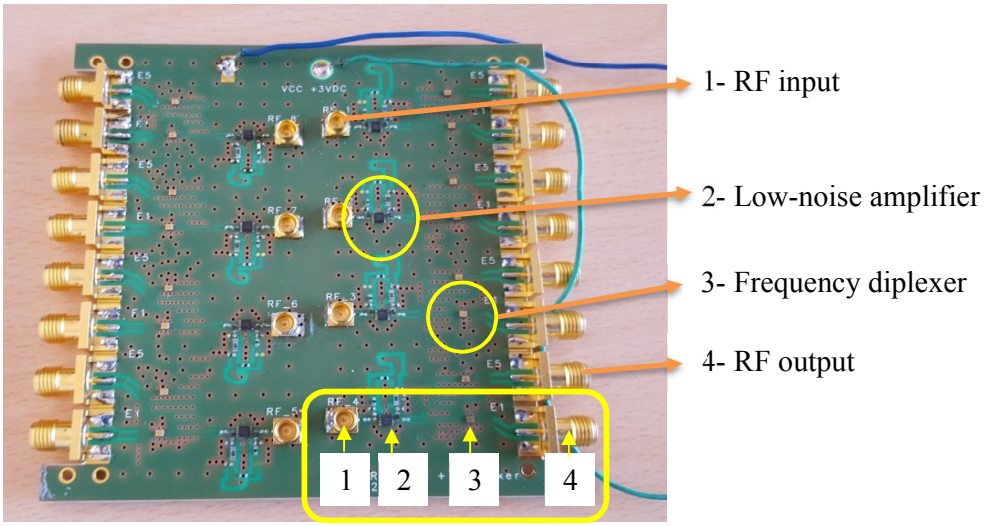

Figure 5.20: The pre-amplifier stage, consisting of eight low-noise amplifiers, and eight frequency diplexers, using off-the-shelf components

5.8.2 RF-IF down-converting

The resulting RF signals from the preamplifier stage were delivered to an RF-IF down-converting circuit, which down converts the RF signals from the L1- an L5-bands to the two IF bands at 60.42 MHz and 133.55 MHz, respectively.

The circuit combined a coherent phase-locked loop with two local oscillators at 1.515 GHz and 1.310 GHz, driving eight mixers and eight reconfigurable IF-amplifiers with band-pass filters of 30 MHz bandwidth. These functions were realized in an Application-Specific Integrated Circuit (ASIC) chip, with eight RF-channels manufactured in a 180 nm United Microelectronics Corporation (UMC) technology. This technology allows for building compact RF-IF front-ends for the array-based GNSS receivers, despite the multi RF channels.

The integrated chip (named D1027A-ASIC) was placed on an evaluation board using "Chip-on-Board" technology, bonded to the PCB with 25 µm gold wires. The 8-channel chip and its PCB were developed by IMMS GmbH in cooperation with Technische Universität Ilmenau[4]. Two PCBs were needed for the twelve channels. More details about the design are in the IMMS report [128].

A block diagram that highlights the functions of the RF-IF front-end is presented in Fig. 5.21. The fabricated PCBs are illustrated in Fig. 5.22.

[4] From the side of TU Ilmenau: Dr.-Ing. Safwat Irteza was responsible for the design phase, and later Dr.-Ing. Kurt Blau and me were responsible for phases of testing, system integration, and system evaluation.

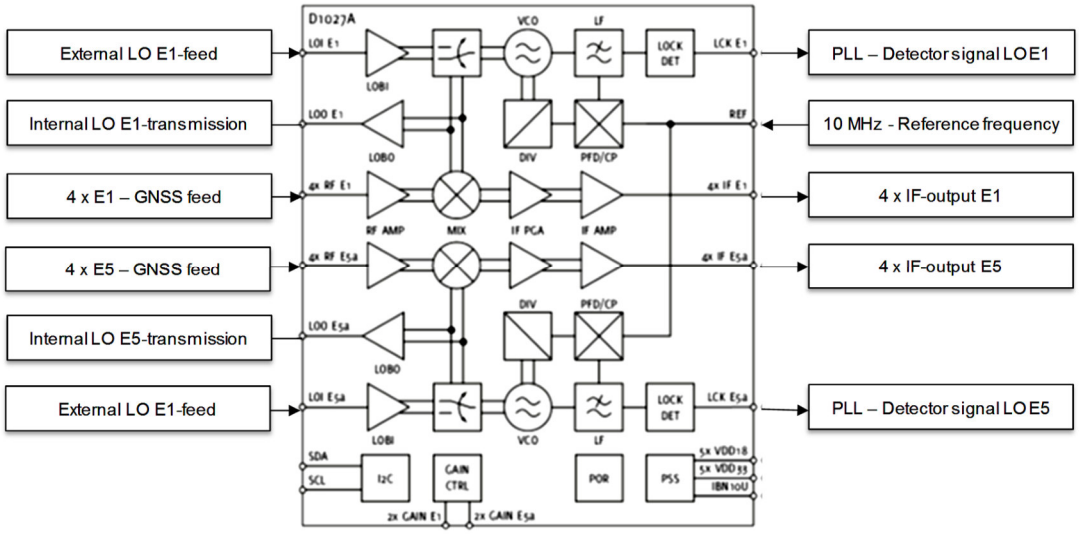

Figure 5.21: A block diagram that highlights the main functions of the RF-IF front-end.

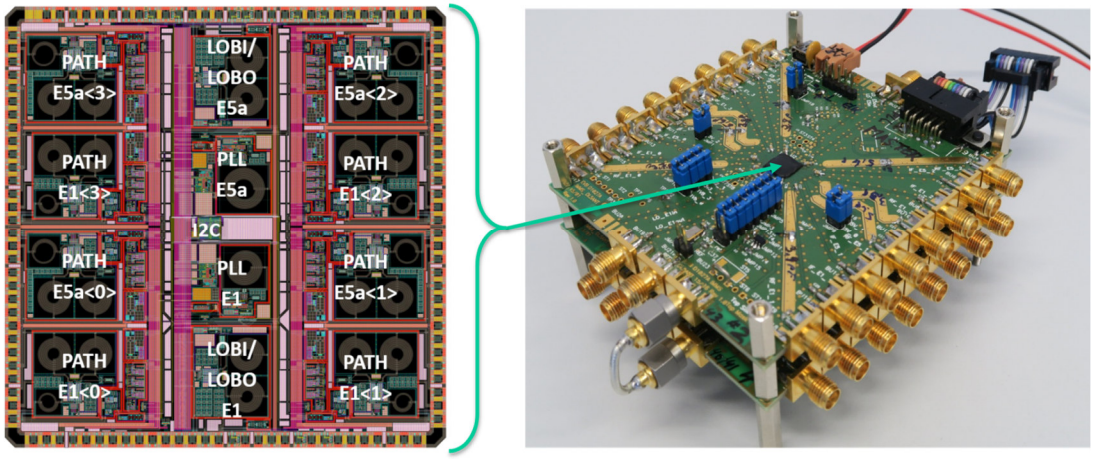

Figure 5.22: (Right): perspective-view of the two 8-channel RF-IF front-end PCBs, with main functions integrated in ASIC chips manufactured in UMC technology. (Left): layout of the 5 mm × 5 mm D1027A-ASIC chip.

The amplification measured for the entire RF-IF chain of the front-end was approximately 89 dB, with a noise-figure of 1.25 dB. This gain was controlled in the proposed design, using dual in-line package (DIP) switches, to ensure similar power levels of the different channels, and to avoid saturation of the front-end, especially in the presence of jamming interferers, as will be discussed in the next chapter.

The IF channels were finally filtered by external stand-alone SMA-SMA filters at 60.42 MHz for the L1-band and at 133.55 MHz for the L5-band.

A photograph of the entire analog receiver, combining the antenna, the DMN, and the RF-IF front-end, and the other circuits, is presented in Fig. 5. 23.

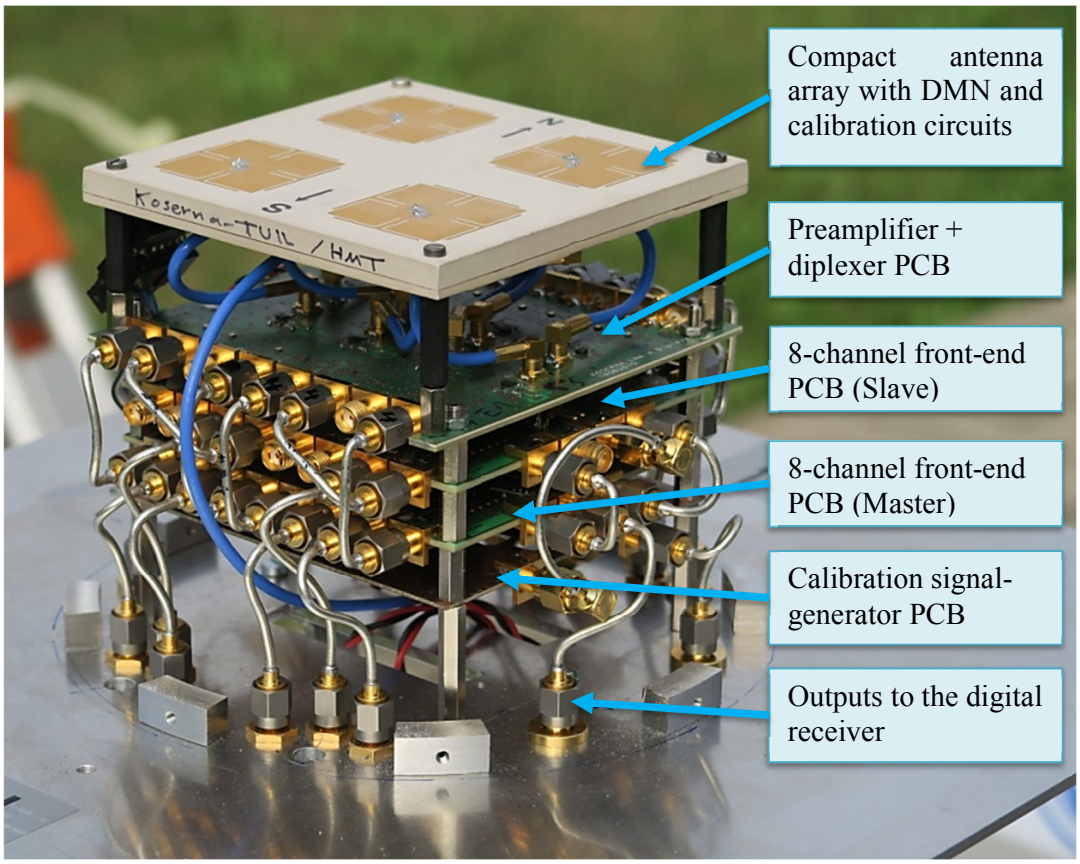

Figure 5.23: Top-view of the innovative sixteen-channel dual-band dual-polarized analog GNSS receiver, combining the antenna array, the DMN and calibration board, the preamplifier + diplexer board, the two RF-IF front-end boards, and the calibration signal-generator board. The receiver is mounted on a supporter to enable assembly and measurement on either a tripod or a car-roof.

5.9 Integration with the digital receiver

The digital receiver was developed at the Chair of Electrical Engineering and Computer Systems (EECS) at RWTH Aachen University, in cooperation with the German Aerospace Center (DLR/IKN). Beside its essential functions such as data acquisition and tracking, the receiver incorporates direction-of-arrival estimation, adaptive beamforming, and null-steering algorithms, to enable robustness against jamming and spoofing.

Jammers are initially suppressed using a pre-whitening approach. If jamming is still detected, i.e., in case of strong jamming levels, then it is suppressed using the approach of subspace-projection scheme [129, 130]. In contrast to conventional algorithms, which assume identical gains of the individual radiating elements, the used anti-jamming algorithms were optimized for the different gains of the eigenmodes of the array, which may vary by up to 10 dB.

The receiver circuit was built using field-programmable-gate-array (FPGA) technology. Results were collected and presented by a graphical user interface (GUI) run on a personal computer. The GUI displays information incorporates position, velocity, and time (PVT) of the receiver, the carrier-to-noise ratio (CNR), beamforming weights of the eigenmode patterns, antenna beam pattern, direction-of-arrival estimations, actual directions of the satellites, and altitude estimation.

Chapter 6:

Automotive-related Testing and System Performance Evaluation

6.1 Introduction

Several measurement campaigns were carried out to test and evaluate the receiver performance, with a special focus on its robustness against jamming and multipath propagating. Four main campaigns, with their dates and goals, are stated in Table 6.1.

Table 6.1. The main measurement campaigns, for testing and evaluating the system performance

Measurement Campaign	Goals of the Campaign
Ilmenau 1, Sep. 2016.	Proof-of-concept for principle of antenna array diversity: feasibility of higher-order RHCP eigenmodes
	Proof-of-concept for principle of dual polarization diversity: feasibility of LHCP eigenmodes
Ilmenau 2, Sep. 2016	First-time integration with digital receiver. Check of analog receiver functions with integration
	Proof of functionality of digital receiver algorithms with integration
	Static tests with/without one jamming interferer, with antenna on tripod.
Aldenhoven, Oct. 2016	Static and dynamic tests without interferers, with antenna on car.
	Static and dynamic tests with one to three interferers, with antenna on car
Ilmenau 3, Nov. 2016	Static tests with/without one to three interferers
	Investigation of car influence on system performance

The term of system robustness can be seen from different perspectives. A discussion about the used robustness figure-of-merits will follow to help understanding the term before starting describing the measurement setups and results.

6.2 Robustness figure-of-merit

A GNSS receiver is considered operating when it can track enough number of satellites with good Geometric Dilution of Precision (GDOP) to compute the correct position with a specified accuracy.

Moreover, it is considered robust against jamming sources when it can block the directions from which jamming signals arrive, and track the needed number of satellites with good GDOP at the other directions. The degree of robustness depends on many parameters, such as:

- The number and direction of GNSS satellites available in the sky-view.
- The number and direction of jamming sources.
- The maximum jamming-to-signal ratio (JSR) bearable by the receiver before it stops functionality.
- The propagation channel and impact of multipath.
- The receive antenna (number of radiating elements, radiation patterns, radiation eigenefficiencies, spatial diversity, polarization diversity, frequency diversity, etc.).
- The beamforming capability to desensitize the receiver at directions of jamming sources, involving the antenna array, the feeding network, and the signal processing algorithms used for beamforming, jamming detection and signal acquisition.

Furthermore, the degree of robustness depends on the RF-IF full chain gain of the front-end. Saturation of the front-end due to high-power jamming signals can be avoided by decreasing the RF-IF gain, which comes at the cost of losing the sensitivity to the wanted GNSS signals.

Even though positioning accuracy is the main criterion to evaluate the performance of the entire GNSS receiver, the number of satellites tracked by the system was found to be the most suitable figure-of-merit for describing the robustness of the analog part of the receiver, since it is the most important indicator of the best potential performance of the system regardless of the tunable front-end full gain or the different signal processing algorithms used by the digital part.

Nevertheless, for an anti-jamming receiver, the maximum jamming-to-signal ratio bearable by the receiver, before stopping providing correct positioning solutions, is more meaningful for describing the overall robustness of the system for a specific set of digital algorithms and a fixed front-end gain, which is more interesting for industry.

The jamming-to-signal ratio is defined as:

$$JSR = \frac{P_{jam}}{P_s}, \tag{6.1}$$

where P_{jam} is the average power, measured at the receiver input, of the jamming signals in the operation frequency band (L1 or L5), and P_s is the average power, measured at the receiver input, of the GNSS signals in the operation frequency band (L1 or L5).

The maximum bearable JSR is defined as the jamming-to-signal ratio at which the receiver tracks three GNSS satellites or less, since at least four GNSS satellites are needed to find the position in GNSS systems.

Accordingly, the maximum bearable JSR is the main parameter used to measure the system robustness in this work. The number of trackable satellites is additionally used, when needed, to indicate the potential enhancements of the performance if the front-end gain was retuned or if the signal processing algorithms were enhanced.

6.3 Measurement campaign Ilmenau 1 – Proof-of-concept

6.3.1 Measurement set-up

The IF output signals of the analog receiver should be carried to the digital receiver to perform decoding, tracking, beamforming, null-steering, etc. However, for this campaign, the analog part of the receiver was connected to the GNSS receiver of a commercial mobile phone, to check the feasibility of each of the RHCP and LHCP eigenmodes of the antenna array, independent of the developed digital receiver.

Real-scenario tracking of the GNSS signals was performed at L1-band. GPS, GLONASS, and BeiDou satellites were tracked. The mobile phone was kept in a shielded environment to avoid reception from its built-in antenna, and thus to rely totally on the signal acquired with the developed GNSS front-end.

In order to check the performance of the entire analog chain, RF signals were fed through the RF-IF front-end as in the realistic situation, and then up-converted again to the L1-band using an additional circuit. Resulting RF signals were transmitted again using a separate antenna, to be received by the built-in GNSS antenna of the mobile. The signal power level was adjusted by the programmable amplifiers of the front-end.

To adapt to the single-input receiver, the performance of each of the eigenmodes of the array was measured separately. Measurements focused on positioning accuracy and the number of satellites tracked by each eigenmode, as the two main evaluation criteria, to

measure the performance of each mode. However, since positioning accuracy can be enhanced later by signal processing, e.g., using the advanced carrier-phase smoothing algorithm [131, 132], or the real time kinematic techniques [133, 134], or the precise point positioning [135, 136], hence the number of tracked satellites was considered as the main evaluation criterion.

This approach helps, particularly, to specify which RHCP and LHCP eigenmodes are more useful for the dual-polarized beamforming algorithms, especially for cost-efficient receivers where including more modes is not affordable, since it means more RF-IF channels in the front-end and more hardware/software complexity in the digital receiver. This case applies for the proposed design, where it was found that only six channels can be processed simultaneously by the digital receiver.

6.3.2 Feasibility of the higher-order and cross-polarized eigenmodes

Figure 6.1 shows screenshots taken by the software "AndroiTS GPS Test" [137], for the system positioning performance, using each of the RHCP eigenmode.

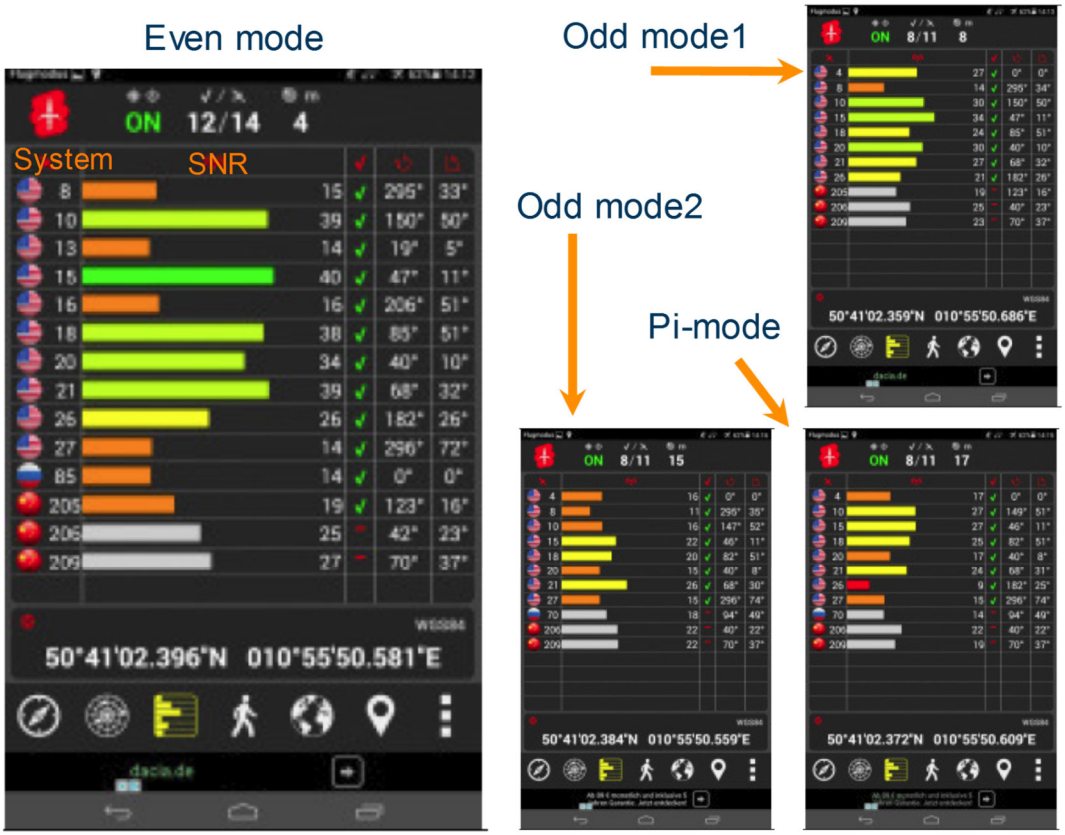

Figure 6.1: Screenshots of "AndroiTS GPS Test" for each RHCP eigenmode. Color bars refer to the signal-to-noise ratio (SNR), grey bars refer to unusable satellites, the flags refer to the systems tracked (American flag for GPS, Russian flag for GLONASS, and Chinese flag for BeiDou).

The results are summarized in Table 6.2. The table shows the number of satellites detected, the number of satellites used for tracking, and the positioning accuracy achieved, using each RHCP and LHCP mode.

TABLE 6.2: Eigenmode performance, focusing on the number of satellites detected/tracked, and the positioning accuracy achieved.

Polarization	Eigenmodes	Number of satellites detected (GPS, GLONASS, BeiDou)	Number of Satellites tracked	Positioning Accuracy
RHCP	Even mode	14 (10, 1, 3)	12	4 m
	Odd mode 1	11 (8, 0, 3)	8	8 m
	Odd mode 2	11 (8, 1, 2)	8	15 m
	Pi-mode	11 (8, 1, 2)	8	17 m
LHCP	Even mode	6 (5, 0, 1)	5	35 m
	Odd mode 1	7 (6, 0, 1)	6	10 m
	Odd mode 2	9 (6, 0, 3)	7	11 m
	Pi-mode	6 (5, 0, 1)	5	50 m

The results reveal that the RHCP modes are, in general, better than the LHCP modes, which is expected from the fact that the GNSS signals are RHCP. The RHCP even mode performs the best because, as illustrated in Fig. 6.2, its single beam is directed towards the zenith with a realized gain higher than any other mode. The LHCP even mode has a pattern like the RHCP one, but with a larger polarization mismatch with the RHCP GNSS signal, and therefore it performs worse.

Each of the two RHCP odd modes has two beams tilted to about $\theta=\pm30°$ in elevation, and therefore they perform better than the even mode at such low elevations. Measurement data and analysis show that they could track eight satellites and acquire a positioning accuracy between 8 m and 15 m. They started to detect satellites at elevations below 40°. These results confirm the potential of using these modes to increase the view-angle of the receiver.

Moreover, the multipath propagation has larger influence on the RHCP GNSS signal at low elevations, giving rise to a stronger LHCP component, as explained in detail in [2, 7, 16, 17]. This would result in a performance drop if only RHCP antennas were used, and therefore the proposed system uses both RHCP and LHCP odd modes to receive from these directions. Measurements revealed that LHCP modes started to detect satellites at elevations below about 60°. The results in Table1 show that an accuracy of about 10 meters was achievable using any of the LHCP odd modes, which is close to the performance attained with the RHCP odd modes. This proves the feasibility of using the LHCP odd modes to compensate for the polarization mismatch at low elevations, caused by the multipath propagation.

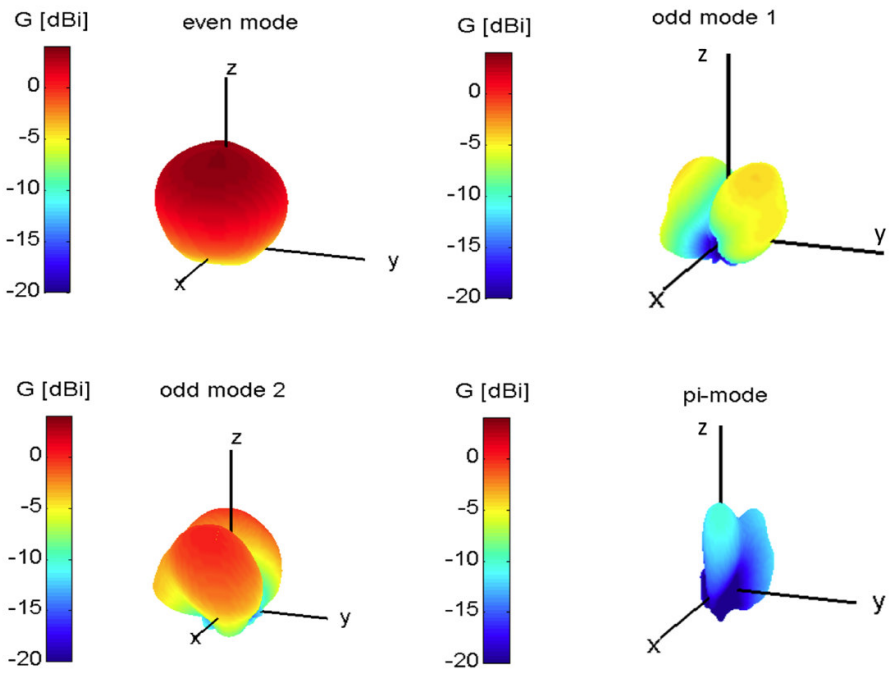

Figure 6.2 (repeat of Fig. 5.17, as it is essential for the discussion): 3D-plots of the far field radiation patterns of the RHCP/LHCP eigenmodes of the single-Layer antenna array, after decoupling and matching.

Finally, the Pi-mode has four beams directed also at about 30° elevation, with about -2 dB realized gain. Such a small gain would result in poor performance of the mode if used alone. The RHCP Pi-mode could achieve a positioning accuracy of about 17 m, while an accuracy of only 50 m was possible using the LHCP Pi-mode. However, this mode remains to be very useful for beamforming, especially for RHCP.

6.3.3 Conclusions

The analog part of the diversity dual-band and dual-polarized compact GNSS receiver was evaluated by a real GNSS test scenario. Measurement results confirmed the feasibility of the higher-order RHCP eigenmodes that could achieve reasonable accuracies of 8 m to 17 m. Results confirmed also the possibility of using the LHCP modes to compensate for the polarization mismatch caused by multipath propagation at elevations below 60°. For this purpose, the use of the LHCP odd modes was found to be more beneficial, due to their radiation lobes pointing to lower elevations compared to the even mode, and their reasonable realized gains compared to the Pi-mode.

The achieved results are promising, especially for the case of compact powerful array-based receivers, were several modes can be exploited jointly, by beamforming, to enhance the robustness against polarization impurity, and extend the coverage to low elevations.

In summary, we have presented the proof-of-concept for the compact array-based dual-band dual-polarized GNSS receiver. These results were published in [48].

6.4 Measurement campaign Ilmenau 2 – Full system integration

6.4.1 System integration with the digital receiver

This measurement campaign followed the first-time full system integration of the analog system with the digital receiver. Therefore, the first phase of this campaign was to check and validate some operation-critical functions in the RF-IF chain such as the IF filters, the 10 MHz reference signal, and the 10 to 30 dB switchable gain amplifiers. The functionality of the digital receiver was also controlled and approved.

Afterwards, static tests were performed with and without one jamming interferer, to check to the system robustness. The antenna, at this point, was mounted in a tripod, and thus no car influence was involved.

6.4.2 Static performance evaluation without interferers

The second phase of the campaign was to run static tests without interferers. The analog GNSS receiver was mounted on a tripod and connected to the digital receiver, as shown in Fig. 6.3. Static tests were performed while tracking real GNSS satellites, involving GPS and Galileo systems.

Tests confirmed the functionality of the system at both the L1-band and L5-band, with positioning accuracy of 30 cm to 3 m at the L1-band depending on the acquisition algorithms used by the digital receiver. Positioning solutions depending only on the L5-band were not possible, because there were only two Galileo satellites operating at that band in the sky-view, since the L1-band is still the most popular band used by GNSS satellite systems. However, the two satellites were enough to prove the capability of the system to track and decode Galileo signals, which was tested for the first time for this project.

6.4.3 Static performance evaluation with one jamming interferer

System performance was tested with existence of one self-made jamming source. The jammer was built with a continuous wave (CW) signal generator of maximum output power of 9 dBm, and a horn antenna of 13 dBi gain. The antenna was placed about 30 m away from the receive antenna, at about 11° elevation, with a line of sight to the receiver, as illustrated in Fig. 6.4.

With this setup, it is possible to jam the receiver with a jamming-to-signal ratio up to 85 dB (measured value).

Figure 6.3: Measurement-setup in the measurement campaign Ilmenau 2, with the antenna system mounted on a tripod.

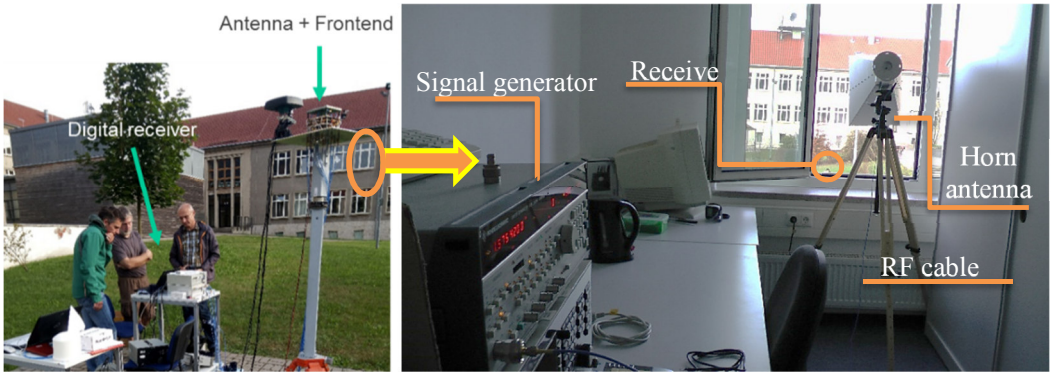

Figure 6.4: Setup of the continuous wave jamming source, about 30 meters far from the receive antenna, at 11° elevation.

Evaluation tests showed that the system was correctly operating up to a JSR of about 70 dB, when using the four RHCP eigenmodes, which fulfills the targeted objectives of the system.

In another perspective, measurements confirmed the feasibility of the dual-polarized systems to compensate for multipath propagation impact on the GNSS polarization. Two more low-elevation satellites were trackable when using the LHCP modes in addition to the RHCP modes. These two satellites give the antenna more degrees-of-freedom, either to enhance the positioning accuracy or to form its radiation pattern to block possible jamming sources and track enough satellites for positioning. Measurements revealed that the system was robust for a JSR up to 85 dB, when using the two LHCP odd eigenmodes in addition to the four RHCP eigenmodes. This was the most important result of this campaign. With such a result, the developed system outperforms the state-of-the-art systems described in [3, 6, 26-28], where a JSR-tolerance between 25 dB, for a single antenna receiver, and 60 dB, for an array-based receivers, was provided. The system also outperforms the single-polarized array-based receiver designed under the preceding project "KOSERNA", where a JSR-tolerance of about 55 dB was achieved, and the enhanced KOSERNA receiver, with front-end gain-control, where 70 dB JSR-tolerance was reachable.

6.5 Measurement campaign ATC-Aldenhoven – On-car tests

6.5.1 Measurement setup

The main goal of this campaign was to check the system performance when the antenna system is installed on the car roof as shown in Fig. 6.5.

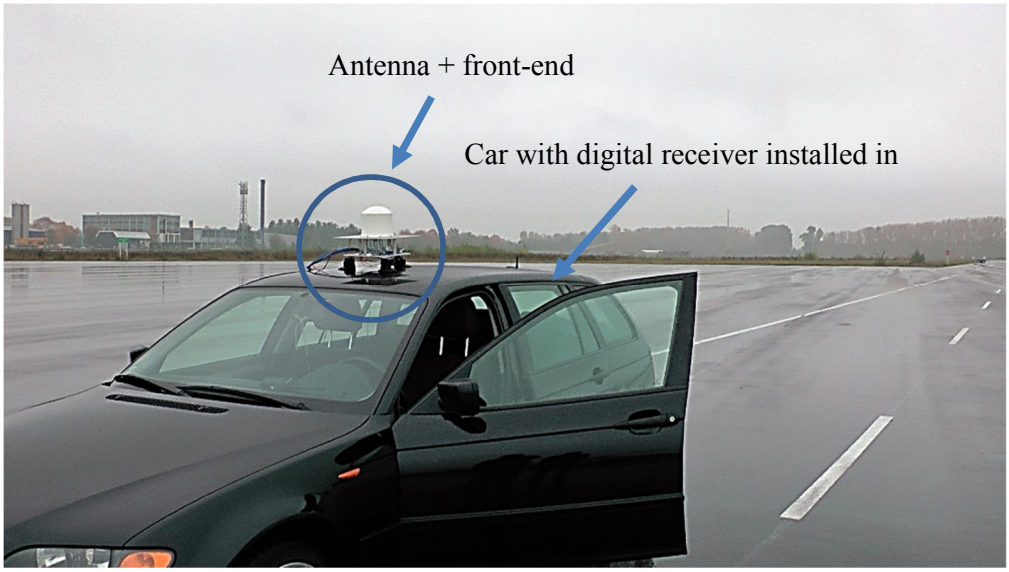

Figure 6.5: Mounting of the RF-IF receiver on the car roof, with the digital receiver installed inside.

The antenna was protected from weather conditions using a radome designed in TU Ilmenau[5]. Numerical simulations and far field measurements confirmed a minor influence of the radome on the radiation patterns and the resonance frequencies of the antenna array. A detailed study of the effect of the radome on the receiver performance, or a comparison between performance with Radome and performance without it was not performed at this stage of the work.

The receiver was tested for static and dynamic scenarios, with/without one to three jamming sources, as illustrated in Fig. 6.6, Fig. 6.7, and Fig. 6.8. The jamming interferers were generated with three different interferer models:

- Continuous wave signal.
- Noise-modulated signal.
- Pulse signal (generated usually by airport radar systems with, for example, 10 μs length and 5% duty-cycle).

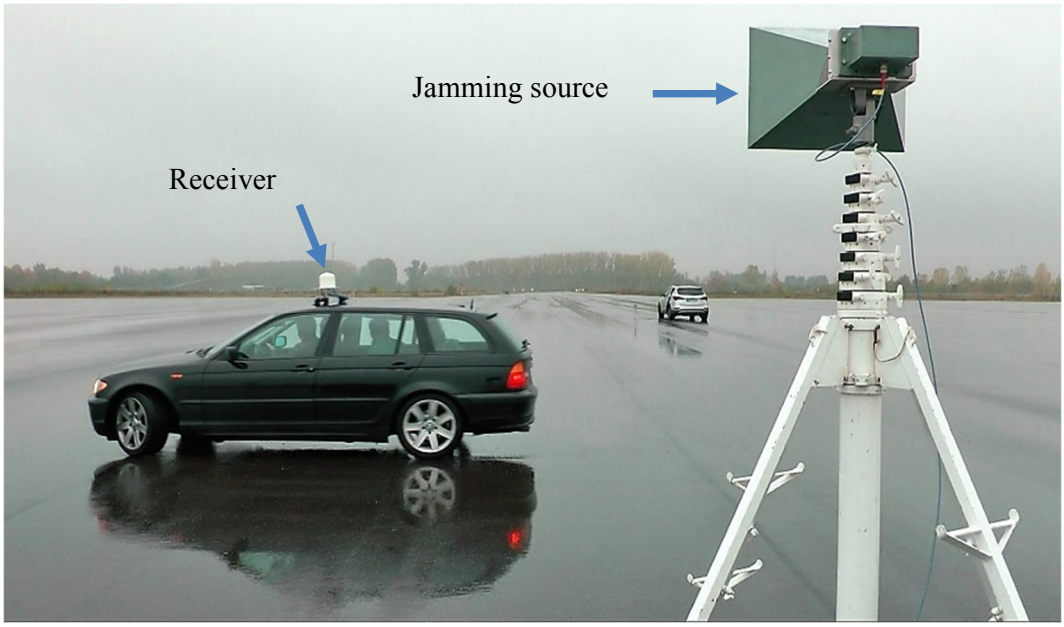

Figure 6.6: Setup of static tests with one jamming source, while the RF-IF receiver is placed on car roof.

Each jamming signal was carried on an RF signal at the L1-band, and radiated through a horn antenna. The jamming sources were placed on low elevations (5° and 16°) and different azimuths to simulate a realistic scenario. An example of the realized noise-modulated jamming source is illustrated in Fig. 6.9.

[5] By Dr.-Ing. Safwat Irteza who was at TU Ilmenau, within the framework of the preceding project KOSERNA.

Figure 6.7: Snapshots of the dynamic tests with one jamming source.

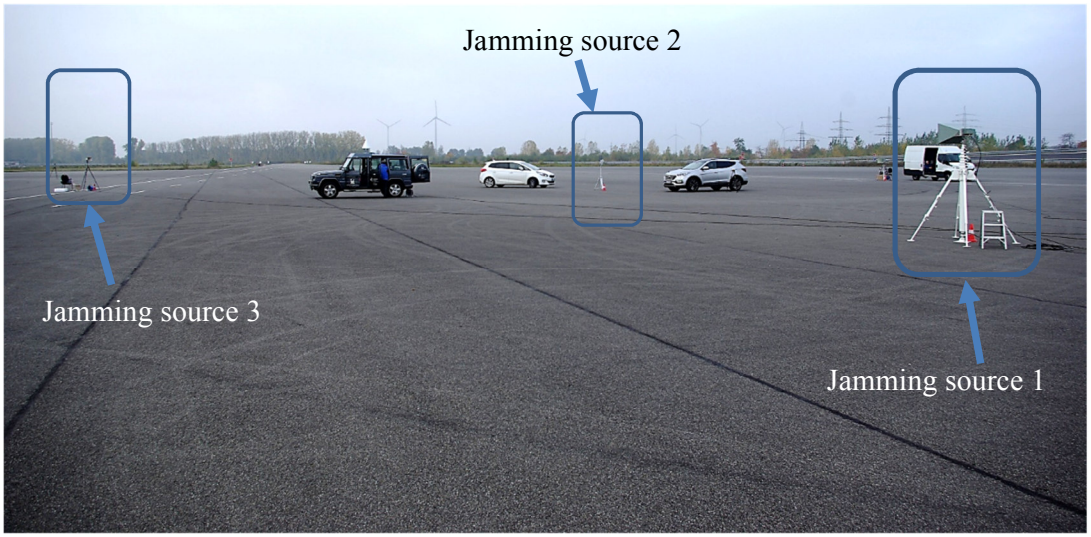

Figure 6.8: Installation of three jamming source for static and dynamic tests.

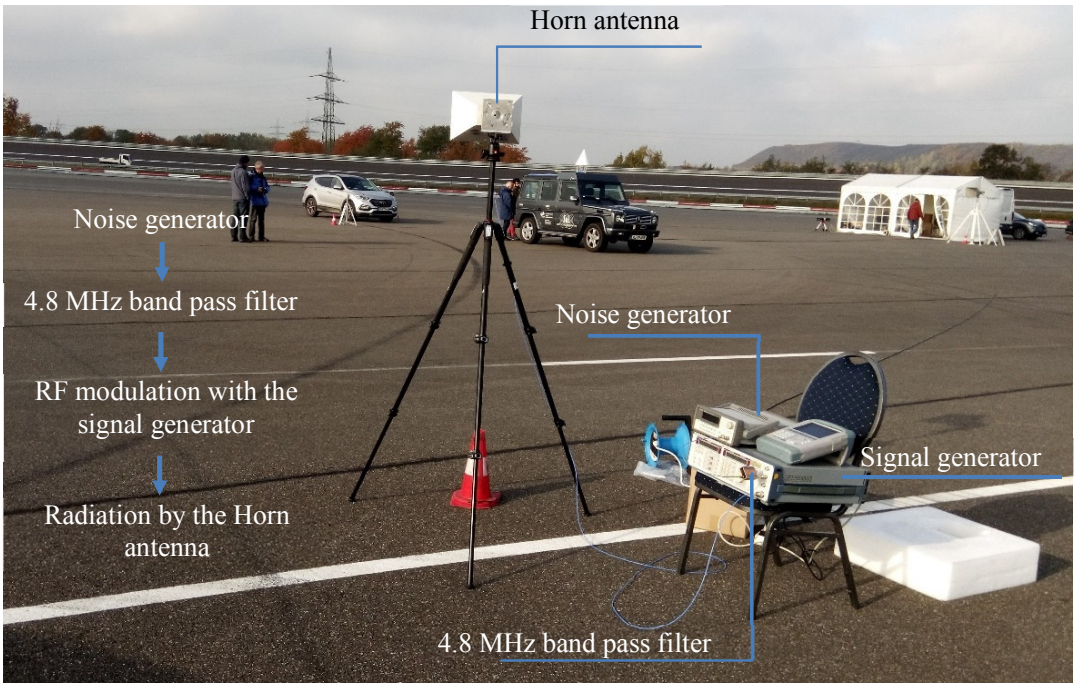

Figure 6.9: In-field installation of the noise-modulated jamming source, with a noise signal bandwidth of 4.8 MHz, modulated to the L band (in-band or out-of-band), and transmitted using a horn antenna with line-of-sight to the receiver.

6.5.2 System robustness against one jamming interferer

A- Robustness due to array diversity

When only the four RHCP eigenmodes were used, static tests confirmed the robustness of the receiver against one CW jamming source for a jamming-to-signal ratio up to:

- 75 dB, for the interferer at the elevation $\theta=5°$.
- 65 dB, for interferer elevation of $\theta=16°$.

These results, together with the relevant result from the second measurement campaign (70 dB JSR-tolerance, for the interferer at the elevation $\theta=11°$), show that the system robustness depends on the elevation of the jamming sources. In other words, the receiver features a better robustness against lower-elevated jammers, as illustrated in Fig. 6.10. This result is attributed to the gain pattern of the antenna, which rapidly decreases at lower elevations resulting in reduced levels of the received jamming power.

This feature of the antenna pattern, in spite of its influence on the reception of low-elevation GNSS signals, is essential for robustness against jamming sources. The result shows that metallic walls can be used to surround future antenna arrays to enhance their immunity to jamming sources, if enough number of GNSS satellites with good GDOP is guaranteed at higher elevations. However, this is still not the case for recent applications, since GNSS

satellites are still limited in number, and therefore reception with wide field-of-view is needed for better performance.

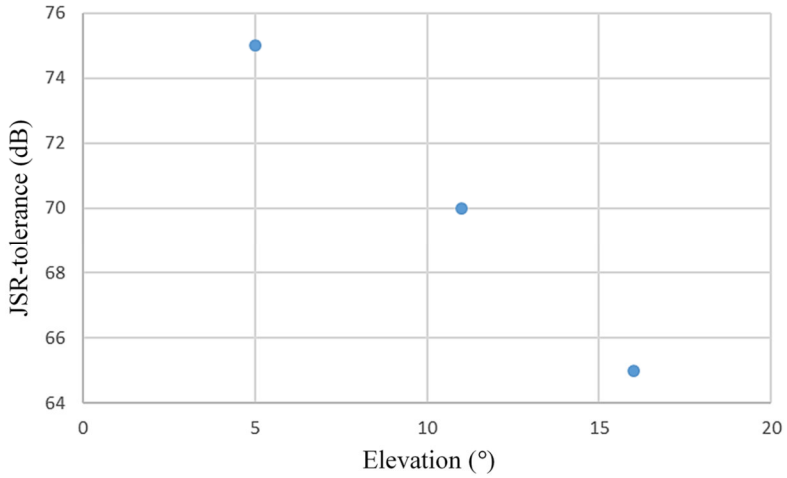

Figure 6.10: Maximum JSR bearable by the system, for different elevations of the jamming sources.

The same JSR-tolerance levels were achieved against a noise-modulated jamming signal, since the main jamming parameters, which are the power level and the frequency band, are similar to those of the CW jamming signal.

This was not the case for the pulse jamming signals where a JSR-tolerance ratio up to 95 dB was achieved, because the pulses were too short to force the receiver to lose its tracking state.

B- Robustness due to polarization diversity:

Measurements did not observe a notable JSR gain when using the LHCP modes in addition to the RHCP ones. This observation is quite interesting, because it is attributed to the fact that the multipath influence in ATC was weaker than that of Ilmenau. Measurements in ATC were held in an open area with few buildings 400 m away at one single direction, while tests were held in Ilmenau in a semi-closed yard of 75 x 30 m^2 area, surrounded by buildings at almost all directions, which gives rise to stronger multipath effects, and hence better feasibility of dual polarization diversity.

6.5.3 Robustness against two and three jamming sources

This was the point to test the system robustness against two or three jamming interferers, which highly depends on the antenna beamforming capability. However, measurements revealed poor beamforming flexibility, due to an internal CW distortion signal at the IF band of 60 MHz. The distortion signal was caused by unwanted harmonics of the reference

signal of 10 MHZ, and was about 20 dB higher than the data signal. Additionally, measurements observed spurious at 55 MHz and 65 MHz, due to mixing. These signals were about 10 dB higher than the signal.

Due to these distortions, beamforming algorithm was misled, resulting in a gain depression at some directions, as illustrated in Fig. 6.11, and yielding a performance close to that of the two-element antenna array. Therefore, this test was postponed to the following campaign, where the internal distortions should have been eliminated.

The internal distortions were possible to be filtered out in the digital receiver. However, due to limitation in the digital resources, only the 60 MHz distortion was cancelled by software, while the 55 MHz and 65 MHz signals were filtered out using 4.8 MHz bandpass filters.

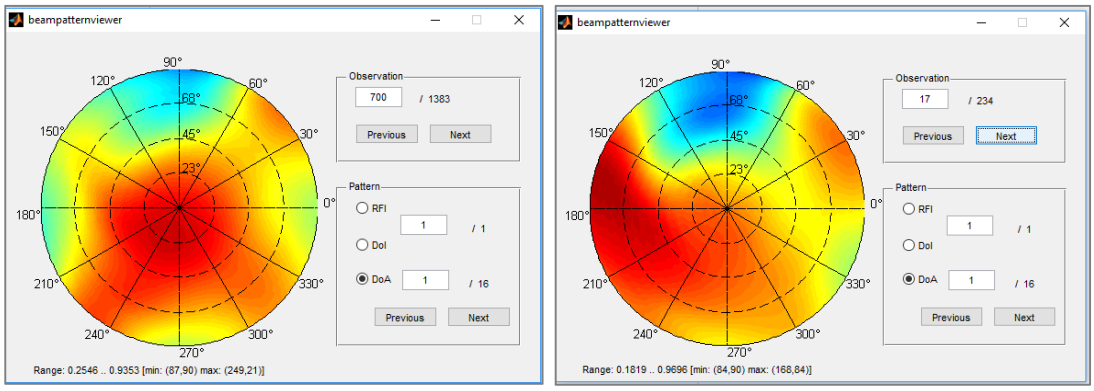

Figure 6.11: Impact of the IF signal distortions on the antenna patterns resulting from beamforming algorithms. The two examples here show a fixed gain depression at north.

6.5.4 Dynamic tests

Dynamic tests were performed for speeds up to 30 km/h. Measurements did not show a notable influence of the movement of the car on the receiver performance at theses speeds.

Tests at higher speeds were not performed due to the technical problems regarding the internal distortions. However, dynamic tests for the predecessor project KOMPASSION showed that the system maintains robustness up to at least 120 km/h. With the advantage of exploiting dual-polarization, a better robustness is expected for the recent receiver KOSERNA.

6.6 Measurement campaign Ilmenau 3 – Complete system evaluation

This final campaign was held after filtering the internal distortions out as described in section 6.5.3. Due to capacity, only static tests were run. Only the RHCP modes of the array were involved in the following test.

Three jamming sources (two CW and one noise-modulated) were built, to evaluate the system robustness against two or three jammers. The jammers were distributed at three different directions, 15 to 30 meters away from the antenna, as illustrated in Fig. 6.12.

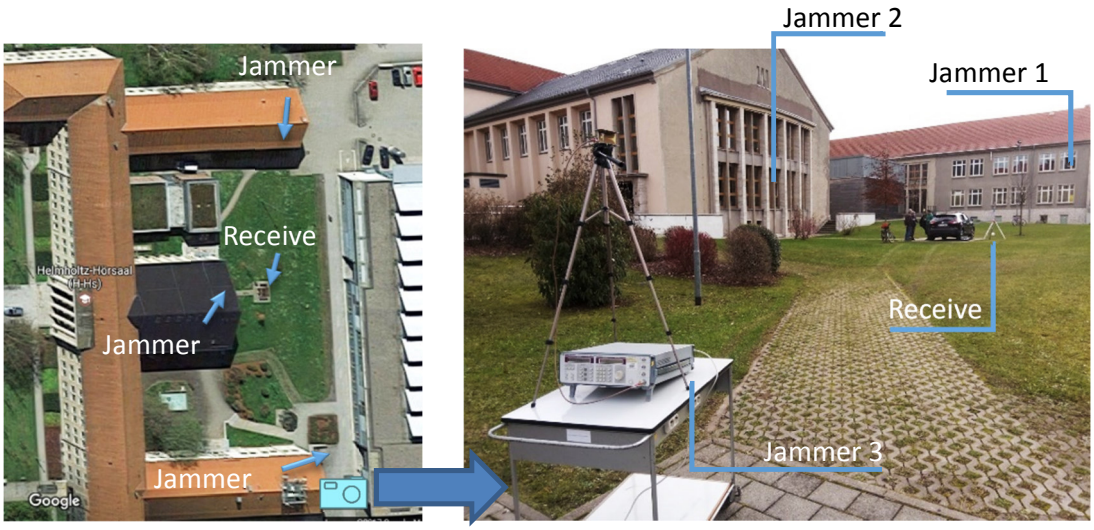

Figure 6.12: Top-view (left) and side-view (right) of the setup of the "measurement campaign Ilmenau 3", with antenna placed either on a tripod or on the car roof. The test was performed in a 75 m x 30 m yard surrounded by buildings. Three jamming sources at three different directions were used.

6.6.1 Robustness against one jamming source

System evaluation started with testing the receiver robustness against one CW jamming interferer "Jammer 1" at elevation of 11º, as represented in Fig. 6.12.

For this test, the antenna was mounted on a tripod. Measurements proved the system robustness up to a JSR of 70 dB, which confirms the results achieved in the second measurement campaign Ilmenau 2 (section 6.4.3).

The same result was achieved when using the noise-modulated jamming source "Jammer 2", which confirms the results achieved in the third measurement campaign at ATC-Aldenhoven (section 6.5.2).

6.6.2 Influence of car-body on anti-jamming robustness

The same robustness test against one jamming source was repeated with the antenna on a car roof, instead of the tripod, in order to get a quantitative measure of the car influence on the system robustness.

Measurements revealed that the system mounted on the car roof was robust against jamming up to JSR = 65 dB, which is 5 dB less than the case without car. This is due to the impact of the car body on the radiation pattern of the antenna array, as the car reduces the gain at zenith and increases it at low-elevation directions where the jamming source is.

While this result gives an indication of the car influence on the robustness of GNSS receivers, it must be considered that the estimation may depend also on the scenario case and the distribution of satellites in the sky-view. Reliable estimations of the car influence may need further investigations in the future.

6.6.3 Robustness against two jamming sources

Having the internal distortions filtered out, the robustness of the receiver against two or three jamming sources was tested for the first time. One CW jamming source "Jammer 1" and one noise-modulated jamming source "Jammer 2" were built and positioned at two directions with 90° azimuth difference (almost south and east), and 11º elevation, as illustrated in Fig. 6.12.

First measurements were run while Jammer 1 was producing a fixed jamming-to-signal ratio of JSR1 = 45 dB, which is too small compared to the 70 dB JSR-tolerance in case of one jamming source (at 11º elevation). Jammer 2 was tuned up to a maximum level of JSR2 = 75 dB. Measurements revealed that the GNSS receiver was saturated when the second jamming source was at level of JSR2 = 68 dB or higher, which is comparable to the case of one jamming signal (where JSR-tolerance =70 dB). This impact of the second source is scenario-dependent and may change depending on the distribution of the satellites in the sky, the relative directions of both jamming sources, the radiation pattern of the antenna array, and the used beamforming and anti-jamming techniques.

In the second measurement scenario, both jamming sources were tuned to achieve close jamming-to-signal ratios at the receiver. It was found that increasing the power level of Jammer 1 to produce a JSR1 of 55 dB forced the need to decrease the power level of Jammer 2 to produce a JSR2 of only 60 dB, instead of 68 dB, to keep the receiver capable of finding the positioning solutions.

6.6.4 Robustness against three jamming sources

At this stage, both Jammer 1and Jammer 2 were placed as described in the previous section, and a new CW jamming source "Jammer 3" was added at elevation $\theta = 0°$, at a direction close to north, as also illustrated in Fig. 6.12.

All jamming sources were tuned together to produce the same JSR level at the GNSS receiver. Measurements found that the system was robust against a jamming-to-signal ratio up to JSR1 = JSR2 = JSR2 =50 dB.

These results achieved through the described automotive-related measurement campaigns are published in [138].

Chapter 7:

Conclusions

This thesis describes the design and evaluation of a fully operational dual-band dual-polarized GNSS receiver that exploits array-diversity and polarization diversity to enhance its robustness against signal distortions such as jamming and multipath propagation.

The designed receiver included a four-element dual-band dual-polarized antenna array (using two different versions of the radiating elements, stub-loaded single-layer patch antenna elements, and multi-layer patch antenna elements), integrated with its decoupling and matching networks, and followed by a calibration network, a preamplifier and frequency diplexer stage, and an RF-IF front-end, in addition to an eigenmode-based and anti-jamming digital receiver that exploits the array- and polarization-diversity of the antenna array to detect and block one to three jamming sources, and enhance the system robustness.

The thesis studied different aspects that affect the array-diversity and the polarization-diversity of the antenna array. This involved the sources of mutual coupling in compact antenna arrays, the influence of mutual coupling on radiation efficiency, the sources of cross-polarized radiating fields in patch antenna elements, and the influence of mutual coupling in compact patch antenna arrays on the cross-polarization discrimination. Moreover, the work described the approach of eigenmode-based decoupling and matching networks, and how it helps to mitigate the influence of mutual coupling on the radiation efficiency and the cross-polarization discrimination.

The designed system demonstrator was installed on either a tripod or a car roof, and evaluated for its robustness against scenarios highly related to safety-critical and automotive applications, including static and dynamic tests with one to three jamming sources of different types.

The performance evaluation confirmed the feasibility of the higher-order RHCP eigenmodes, particularly at elevations below 40°, which helps to extend the coverage area of the receiver to track more satellites and enhance the positioning accuracy.

Moreover, measurements proved the feasibility of the LHCP mode, especially the odd modes, to compensate for the multipath propagation at elevations below 60°, and enhance the anti-jamming robustness of the system at these directions.

Quantitatively, for the antenna on the tripod, when only the RHCP modes were sued, the system was proved to be robust against one to three jamming sources with:

- JSR up to [65 dB to 75 dB], for a single jamming source at 5° to 16 ° elevation.
- JSR between 55 dB and 60 dB, for two jamming sources, at 11° elevation.
- JSR up to 50 dB, for three jamming sources, at 5°, 11° and 11° elevations.

The use of the LHCP odd modes added a gain of 10 to 15 dB to the maximum JSR-tolerance level.

The impact of the car on the JSR-tolerance level was estimated by about 5 dB loss, for the tested scenarios.

The designed receiver outperforms the state-of-the-art systems described in several literatures [3, 6, 26-28].

The main conclusions of this dissertation can be summarized in the following points:

- Array diversity enhances the signal-to-noise ratio of global navigation satellite system receivers, and enables beamforming to enhance the receiver robustness against multipath propagation, atmospheric impact, jamming, and spoofing.

- Polarization diversity compensates for the influence of multipath propagation, and helps to enhance the robustness against jamming sources.

- Compact array-based receivers suffer from mutual coupling between the radiating elements, which degrades the eigenefficiencies of the array, and subsequently its diversity gain.

- Mutual coupling decreases the cross-polarization discrimination (XPD) of the radiating patch antenna elements across the entire upper half-sphere, and especially at low elevations.

- Decoupling and matching networks partially restore the radiation eigenefficiencies and the polarization purity.

- In compact antenna arrays, the XPD gain achieved by proper optimization of the single antenna element can be significantly larger than the XPD gain restored by introducing decoupling techniques to reduce the influence of the mutual coupling, which stresses the importance of the fine tuning of the single antenna element regarding its XPD.

- Array-based receivers that use adaptive beamforming outperform receivers that use uniform beamforming and do not consider the different gains of the array eigenmodes.

- Gain-control of the RF front-end of the GNSS receiver helps to enhance the anti-jamming robustness level of the receiver at the cost of reducing its sensitivity to the useful navigation signals. A trade-off between the anti-jamming robustness level and the signal sensitivity is essential for automotive-dedicated GNSS receivers.

- Realistic implementation of a robust dual-band dual-polarized array-based GNSS receiver, with decoupling and matching networks, adaptive beamforming, and gain-control was possible. The receiver outperforms several single-element and array-based anti-jamming receivers, described in literature, in term of anti-jamming robustness level.

References

[1] J. Coffed, “The Threat of GPS Jamming, The Risk to an Information Utility,” Exelis Inc., 2014. [Online]. Available: http://gpsworld.com/wp-content/uploads/2014/02/ThreatOfGPSJamming_FEB14.pdf. [Accessed 2017].

[2] P. Closas and C. Fernández-Prades, “A Statistical Multipath Detector for Antenna Array Based GNSS Receivers,” *IEEE Transactions on Wireless Communications,* vol. 10(3), pp. 916 – 929, 2011.

[3] A. Brown, “Performance and jamming test results of a digital beamforming GPS receiver”, Proceedings of Joint Conference on Navigation, pp. 1-11, May 6–9, 2002.

[4] S. Irteza, “Compact adaptive planar antenna arrays for robust satellite navigation systems,” Dissertation, TU Ilmenau, 2016.

[5] Y. Fan, Z. Zhang, M. Trinkle, A. D. Dimitrovski, J. B. Song and H. Li, “A Cross-Layer Defense Mechanism Against GPS Spoofing Attacks on PMUs in Smart Grids,” *IEEE Transactions on Smart Grid,* vol. 6, no. 6, pp. 2659-2668, 2015.

[6] Ö. C. Dabak, F. Erdem, T. Sönmez, L. Alatan and S. S. Koç, “Interference suppression in a GPS receiver with 4 element array design and implementation of beamforming algorithms,” in *IEEE/ION Position, Location and Navigation Symposium (PLANS)*, Savanna, 2016.

[7] B. M. Hannah, K. Kubik and R. A. Walker, “Propagation Modelling of GPS Signals,” in: E.W. Grafarend, F.W. Krumm, V.S. Schwarze (eds) *Geodesy-The Challenge of the 3rd Millennium*, Springer-Verlag Berlin Heidelberg, 2003, pp. 69-77.

[8] D. Hambling, “GPS chaos: How a 30 dollars box can jam your life,” *NewScientist Magazine,* no. 2803, 2011. [Online]. Available: https://www.newscientist.com/article/dn20202-gps-chaos-how-a-30-box-can-jam-your-life/. [Accessed Jan. 2018].

[9] D. S. D. Lorenzo, “Navigation Accuracy And Interference Rejection For Gps Adaptive Antenna Arrays,” Dissertation, Stanford University, 2007.

[10] S. Daneshmand, N. Sokhandan, M. Zaeri-Amirani and G. Lachapelle, “Precise Calibration of a GNSS Antenna Array for Adaptive Beamforming Applications,” *Sensors,* vol. 14, pp. 9669-9691, 2014.

[11] J. A. L´azaro, “GNSS Array-based Acquisition: Theory and Implementation,” Dissertation, Universitat Politècnica de Catalunya, 2012.

[12] A. J. O’Brien, “Adaptive Antenna Arrays for Precision GNSS Receivers,” Dissertation, The Ohio State University, 2009.

[13] A. Dreher, N. Basta, S. Caizzone, G. Kappen, M. Sgammini, M. Meurer, S. Irteza, R. Stephan, M. A. Hein, E. Schäfer, M. A. Khan, A. Richter, B. Bieske, L. Kurz and T. G. Noll, "Compact adaptive multi-antenna navigation receiver," in *ION GNSS*, Nashville, TN, USA, 2012.

[14] K. Park and J. Seo, "Adaptive null steering method using a dual polarized antenna to mitigate GPS RHCP interference," in *European Navigation Conference*, Bordeaux, France, April. 2015.

[15] S. Irteza, E. Schaefer, R. Stephan, A. Hornbostel and M. A. Hein, "Compact antenna array receiver for robust satellite navigation systems," *International Journal of Microwave and Wireless Technologies,* 2014.

[16] T. Kos, I. Markezic and J. Pokrajcic, "Effects of multipath reception on GPS positioning performance," in *Proceedings ELMAR-2010*, Zadar, pp. 399-402., 2010.

[17] B. M. Hannah, "Modelling and Simulation of GPS Multipath Propagation," Dissertation, Queensland University of Technology, 2001.

[18] L. Shuangxun, W. Zhan, L. Shengqiang and Z. Yonghong, "GPS Anti-Jamming Utilizing Dual-Polarized Antenna," in *Cross Strait Quad-Regional Radio Science and Wireless Technology Conference (CSQRWC)*, Harbin, China, 2011.

[19] M. Zhang, L. Wang, S. Xu and Y. Wang, "GPS Signal Anti-jamming Based on Dual-polarized Antenna Array," in *Signal Processing, Communications and Computing (ICSPCC)*, Xi'an, China, 2011.

[20] R. Fante and J. J. Vaccaro, "Wideband cancellation of interference in a GPS receive array," *Aerospace and Electronic Systems,* vol. 36, no. 2, pp. 549-564, 2000.

[21] A. Anghel, A. Astilean, T. Letia and A. Komjathy, "Near Real-Time Monitoring of the Ionosphere Using Dual Frequency GPS Data in a Kalman Filter Approach," in *EEE International Conference on Automation, Quality and Testing, Robotics (AQTR)*, 2008.

[22] D. Sunehra, "Real-Time estimation of ionosphric delay using dual frequency GPS observations," *European Scientific Journal,* vol. 9, no. 15, 2013.

[23] M. V. T. Heckler, M. Cuntz, A. Konovaltsev, L. A. Greda and M. Meurer, "Development of robust safety-of-life navigation receivers at the German Aerospace Center (DLR)," in *IEEE MTT-S Int. Microwave Symp*, Digest, 2010.

[24] "Galileo Antenna Demonstrator," German Aerospace Center (DLR), 2006-2020. [Online]. Available: http://www.dlr.de/kn/en/desktopdefault.aspx/tabid-4306/6938_read-9224/. [Accessed Oct. 2017].

[25] "Compact Adaptive Terminal Antenna for Interference-Free Satellite Navigation (KOMPASSION)," German Aerospace Center (DLR) et al, 2010-2013. [Online]. Available: http://www.dlr.de/kn/en/desktopdefault.aspx/tabid-4309/3222_read-30553/admin-1/. [Accessed Oct. 2017].

[26] M. Jones, "Protecting GNSS Receivers from Interference and Jamming," *Inside GNSS*, pp. 40-49, 2011.

[27] S. Rounds, "Jamming protection of GPS receivers, part II: antenna enhancements," *GPS world*, pp. 38-45, 2004.

[28] F. Boynton, P. F. MacDoran, M. B. Mathews and M. O. Davies, *Webinar: GNSS Interference Detection and Mitigation for UAV Navigation,* Loctronix Corporation in cooperation with GPS World Magazine, 2014. [Online]. Available: https://www.gpsworld.com/gnss-interference-detection-and-mitigation-for-uav-navigation/. [Accessed June. 2017]

[29] "How GPS Works," Integrated Mapping Ltd, [Online]. Available: https://www.maptoaster.com/maptoaster-topo-nz/articles/how-gps-works/how-gps-works.html. [Accessed May 2017].

[30] J. G. McNeff, "The global positioning system," *IEEE Transactions on Microwave Theory and Techniques,* vol. 50, pp. 645-652, 2002.

[31] "What is GPS?," Garmin International, Inc., [Online]. Available: http://www8.garmin.com/aboutGPS/. [Accessed June 2017].

[32] C. J. Hegarty and E. Chatre, "Evolution of the Global Navigation SatelliteSystem (GNSS)," *in Proceedings of the IEEE,* vol. 96, no. 12, pp. 1902-1917, 2008.

[33] A. S. Zaidi and M. R. Suddle, "Global Navigation Satellite Systems: A Survey," in *2006 International Conference on Advances in Space Technologies*, Islamabad, 2006.

[34] Z. Dai, R. J. Watson and P. R. Shepherd, "A propagation modeling approach to urban navigation," in *the 11th European Conference on Antennas and Propagation (EuCAP),* Paris, 2017.

[35] A. Martellucci and R. P. Cerdeira, "Review of tropospheric, ionospheric and multipath data and models for global navigation satellite systems," in *3rd European Conference on Antennas and Propagation*, Berlin, 2009.

[36] J. A. Shrawankar and K. D. Kulat, "A study of influence of fast fading on the performance of mobile communication system," in *International Conference on Microwave, Optical and Communication Engineering (ICMOCE)*, Bhubaneswar, 2015.

[37] C. Schneider, M. Ibraheam, S. Hafner, M. Kaske, M. A. Hein and R. S Thoma, "On the reliability of multipath cluster estimation in realistic channel data sets," in *the 8th European Conference on Antennas and Propagation (EuCAP),* The Hague, 2014.

[38] A. Hornbostel, A. Konovaltsev, H. Denks and F. Antreich, "Simulation of Multi-Element Antenna Systems for Navigation Applications," *IEEE Systems Journal,* vol. 2, no. 1, pp. 7-20, 2008.

[39] Y. Kubo, Y. Muto, S. Kitao, C. Uratani and S. Sugimoto, "Ambiguity resolution for dual frequency carrier phase kinematic GPS," in *TENCON*, Chiang Mai, Thailand, 2004.

[40] J. Coffed, J. Rolli and C. Slutsky, “Detecting and Locating GPS Jamming,” in *Proceedings of the ION 2015 Pacific PNT Meeting, pp. 484 - 492*, Honolulu, Hawaii, April 20 - 23, 2015.

[41] A. Thiel and M. Ammann, “Anti-Jamming techniques in u-blox GPS receivers,” U-blox AG, White Paper, Oct. 2009. Available: https://www.u-blox.com/sites/default/files/products/documents/u-blox-AntiJamming_WhitePaper_%28GPS-X-09008%29.pdf. [Accessed May 2020].

[42] NovAtel, “Mitigating the threat of GPS jamming, Anti-jamming technology,” NovAtel, White Paper, 2012. Available: https://pdfs.semanticscholar.org/7db2/55ef62381a86b7bc9f22cc288656f7ab649f.pdf?_ga=2.111869828.1417101045.1588664460-607257795.1588664460. [Accessed May 2020].

[43] Z. Haider and S. Khalid, “Survey on effective GPS spoofing countermeasures,” in *Sixth International Conference on Innovative Computing Technology (INTECH)*, Dublin, 2016.

[44] X. Fan, L. Du and D. Duan, “Synchrophasor Data Correction under GPS Spoofing Attack: A State Estimation Based Approach,” *IEEE Transactions on Smart Grid,* no. no. 99, pp. pp. 1-1., 2017.

[45] J. Moon and Y. Kim, “Antenna Diversity Strengthens Wireless LANs,” *Communication Systems Design,* pp. 15-22, 2003.

[46] L. Jin, L. Li and H. Wang, “Investigation of different types of array for smart antennas,” in *International Conference on Microwave and Millimeter Wave Technology ICMMT 2008*, Nanjing, China, 2008.

[47] J. Carl B. Dietrich, Adaptive Arrays and Diversity Antenna Configurations for Handheld Wireless Communication Terminals, dissertation, Virginia Polytechnic Institute and State University, 2000.

[48] M. Ibraheam, B. Bieske, K. Blau, E. Schäfer, A. Jäger, S. Butt, R. Stephan and M. A. Hein, “Feasibility of Dual-polarized Antenna Arrays for GNSS Receivers at Low Elevations,” in *11th European Conference on Antennas and Propagation (EuCAP)*, Paris, 2017.

[49] S. Irteza, M. Ibraheam, T. Harz, Y. Bulbin, R. Stephan and M. A. Hein, “Compact Satellite Navigation Antenna Array using Off-the-Shelf Ceramic Patch Antennas,” in *9th European Conference on Antennas and Propagation (EuCAP)*, Lisbon, 2015.

[50] S. Irteza, C. Bornkessel, M. Ibraheam, R. Stephan, F. Wollenschläger, A. Dreher, L. Kurz, M. Meurer, T. Harz, Y. Bulbin and M. A. Hein, “Feld- und Labortests robuster und kompakter Satellitennavigationsempfänger für künftige Fahrautomatisierungen,” in *POSNAV*, Berlin, 2016.

[51] M. Ibraheam, S. Irteza, R. Stephan and M. A. Hein, “Dual-band Dual-polarized Stub-loaded Patch Antenna for Robust GNSS Receivers,” in *The 10th European Conference on Antennas*, Davos, 2016.

[52] S. Irteza, E. Schafer, M. Sgammini, R. Stephan and M. A. Hein, "Impact of polarization impurity on compact antenna array receiver for satellite navigation systems," in *European Microwave Conference (EuMC)*, 2013.

[53] S. Döbrich, "The Future of Automotive Navigation Systems," 2016. [Online]. Available: https://jugsaxony.org/wp-content/uploads/2016/11/The_Future_of_Automotive_Navigation_System.pdf. [Accessed 6 11 2017].

[54] A. DAVIES, "TURNS OUT THE HARDWARE IN SELF-DRIVING CARS IS PRETTY CHEAP," *Wired, https://www.wired.com/2015/04/cost-of-sensors-autonomous-cars/,* 2015.

[55] NovAtel, "High-Precision GPS for Autonomous Vehicles," [Online]. Available: http://www.novatel.com/industries/autonomous-vehicles. [Accessed 10 04 2017].

[56] Google, "Waymo self driving car," 2016. [Online]. Available: https://www.google.com/selfdrivingcar/. [Accessed 06 11 2017].

[57] "Ekinox2-N: INS/GPS," SBG-Systems, [Online]. Available: https://www.sbg-systems.com/products/ekinox-n-ins-gps. [Accessed 2017].

[58] "VN-200 SMD," VectorNav Technologies, 2017. [Online]. Available: http://www.vectornav.com/products/vn-200.

[59] N. P. Somasiri, X. Chen and A. A. Rezazadeh, "Neural network modeller for design optimisation of multilayer patch antennas," *in IEE Proceedings - Microwaves, Antennas and Propagation,* vol. 151, no. 6, pp. 514-518, 2004.

[60] S. Chen, G. Liu, X. Chen, T. Lin, X. Liu and Z. Duan, "Compact Dual-Band GPS Microstrip Antenna Using Multilayer LTCC Substrate," *IEEE Antennas and Wireless Propagation Letters,* vol. 9, pp. 421-423, 2010.

[61] P. K. Deb, T. Moyra and P. Bhowmik, "Dual band multilayer E-shape microstrip patch antenna for C-band and X-band," in *2nd International Conference on Signal Processing and Integrated Networks (SPIN)*, Noida, 2015.

[62] S. Maci, G. B. Gentili, P. Piazzesi and C. Salvador, "Dual-band slot-loaded patch antenna," *IEEE Proc.-Microwaves, Antennas and Propagation,* vol. 142, no. 3, 1995.

[63] S. Maci and G. B. Gentili, "Dual-Frequency Patch Antennas," *IEEE Antennas and Propagation Magazine,* vol. 39, no. 6, 1997.

[64] M. Al-Joumayly, S. Aguilar, N. Behdad and S. Hagness, "Dual-Band Miniaturized Patch Antennas for Microwave Breast Imaging," *Antennas and Wireless Propagation Letters, IEEE,* vol. 9, pp. 268-271, 2010.

[65] K. P. Yang and K. L. Wong, "Dual–band circularly–polarized square microstrip antenna," *IEEE Transactions on Antennas and Propagation,* vol. 49, no. 3, 2001.

[66] *High Frequency Laminates, RO3000 Series Circuit Materials,* USA: RO3010, ROGERS corporation.

[67] S. Caizzone, "Compact E5a/E1 antenna array for GNSS applications," in *10th European Conference on Antennas and Propagation (EuCAP)*, Davos, 2016.

[68] S. Caizzone, "Miniaturized E5a/E1 Antenna Array for Robust GNSS Navigation," *IEEE Antennas and Wireless Propagation Letters,* 2016.

[69] M. Ibraheam, S. Irteza, S. Caizzone, A. Dreher, R. Stephan and M. A. Hein, "Compact dual-band dual-polarized antenna array for robust satellite navigation receivers," in *the 9th European Conference on Antennas and Propagation (EuCAP)*, Lisbon, 2015.

[70] T. Fujimoto, D. Ayukawa, K. Iwanaga and M. Taguchi, "Dual-band circularly polarized microstrip antenna for GPS application," in *IEEE Antennas and Propagation Society International Symposium*, 2008.

[71] Rogerscorp, "RO3000® Series Circuit Materials, RO3003™, RO3006™, RO3010™ and RO3035™ High Frequency Laminates," [Online]. Available: https://www.rogerscorp.com/documents/722/acs/RO3000-Laminate-Data-Sheet-RO3003-RO3006-RO3010-RO3035.pdf. [Accessed 01 06 2017].

[72] *RO4400 Series Bondply,* RO4450F, ROGERS corporation, USA.

[73] *CST Microwave Studio 2013,* CST GmbH, Darmstadt, Germany. After 2017: Dassault Systèmes, Vélizy-Villacoublay Cedex, France.

[74] V. Sokol, "Optimization Techniques in CST STUDIO SUITE," [Online]. Available: https://www.cst.com/Content/Events/Downloads/eugm2011/Talk_6-1-4_CST_UGM_2011.pdf. [Accessed June 2017].

[75] M. Melanie, An Introduction to Genetic Algorithms, Cambridge, Massachusetts • London, England: A Bradford Book The MIT Press, 1999.

[76] C. Volmer, Compact antenna arrays in mobile communications, A quantitative analysis of radiator coupling, Dissertation, TU Ilmenau, 2010.

[77] C. Volmer, J. Weber, R.Stephan, K. Blau and M. A. Hein, "An Eigen-Analysis of Compact Antenna Arrays and Its Application to Port Decoupling," *IEEE Transactions on Antennas and Propagation,* vol. 56, no. 2, pp. 360-370, 2008.

[78] S. Irteza, E. Schäfer, M. Sgammini, R. Stephan and M. A. Hein, "Four-Element Compact Planar Antenna Array for Robust Satellite Navigation Systems," in *IEEE European Conference on Antennas and Propagation (EuCAP)*, Gothenburg, Sweden, 2013.

[79] M. Ibraheam, A. Krauss, S. Irteza and M. A. Hein, "Reduction of Mutual Coupling in Compact Antenna Arrays Using Spatial Tilting," in *the 8th German Microwave Conference, GeMiC*, Aachen, 2014.

[80] S. Irteza, N. Murtaza, S. Caizzone, R. Stephan and M. A. Hein, "Compact planar L-band antenna arrays with optimal diversity performance," in *IEEE-APWC* , Turin, 2011.

[81] N. Behdad, M. Li and M. Al-Joumayly, "Biologically Inspired Electrically Small Antenna Arrays With Enhanced Directional Sensitivity," *IEEE Antennas and Wireless Propagation Letters,* 2011.

[82] N. Behdad, M. Li and M. Al-Joumayly, "Biologically-inspired antenna arrays based on the hearing mechanism of the parasitoid fly Ormia Ochracea," in *Antennas and Propagation (APSURSI), IEEE International Symposium*, 2011.

[83] M. C. Pralon, Compact Antenna Arrays for Efficient Direction of Arrival Estimation, Dissertation, TU Ilmenau, 2016.

[84] M. G. Pralon, D. Schulz and R. S. Thomä, "An eigen-analysis of a compact L-quad antenna array for direction finding," in *IEEE-APS Topical Conference on Antennas and Propagation in Wireless Communications (APWC)*, Palm Beach, 2014.

[85] J. C. Coetzee and Y. Yu, "Port Decoupling for Small Arrays by Means of an Eigenmode Feed Network," *IEEE Transactions on Antennas and Propagation,* vol. 56, pp. 1587-1593, June 2008.

[86] J. L. Allen and B. L. Diamond, "Mutual Coupling in Array Antennas," Technical Report, EDS-66–443, Lincoln Lab., MIT, 1966.

[87] M. MALKOMES, "Mutual coupling between microstrip patch antennas," *ELECTRONICS LETTERS,* vol. 18, no. 12, pp. 520-521, 1982.

[88] E. PENARD and J. P. DANIEL, "Mutual coupling between microstrip antennas," *ELECTRONICS LETTERS,* vol. 18, no. 14, pp. 605-607, 1982.

[89] R. E. Collin, Foundations for microwave engineering, New York, NY, USA: McGraw-Hill, 1992.

[90] C. A. Balanis, ANTENNA THEORY ANALYSIS AND DESIGN, THIRD EDITION, Hoboken, NJ, USA: A JOHN WILEY & SONS, INC., PUBLICATION, 2005.

[91] G. Kumar and K. P. Ray, Broadband microstip antennas, Norwood, MA, USA: Artech House, 1996.

[92] M. A. Khayat, J. T. Williams, D. R. Jackson and S. A. Long, "Mutual coupling between reduced surface-wave microstrip antennas," *IEEE Transactions on Antennas and Propagation,* vol. 48, no. 10, pp. 1581-1593, 2000.

[93] A. K. Bhattacharyya, D. R. Jackson, J. T. Williams and R. Smith, "Microstrip patch designs which do not excite surface waves," Antennas and Propagation Society Symposium 1991 Digest, London, 1991.

[94] A. Đorđević and M. N. Nikolić, "Physical causes of strong mutual coupling among microstrip patch antennas," School of Electrical Engineering, University of Belgrade., Belgrade, 2004. 12th Telecommunications Forum Telfor, Nov. 2004, Belgrade, Serbia, Nov. 2004.

[95] M. M. Nikolic´, A. R. Djordjevic´ and A. Nehorai, “Microstrip Antennas With Suppressed Radiation in Horizontal Directions and Reduced Coupling,” *IEEE TRANSACTIONS ON ANTENNAS AND PROPAGATION,* vol. 53, no. 11, 2005.

[96] N. Murtaza, M. A. Hein and E. Zameshaeva, “Reconfigurable decoupling and matching network for a cognitive antenna,” in *41st European Microwave Conference (EuMC)*, 2011.

[97] Y. Cai and Y. Guo, “A reconfigurable decoupling and matching network for a frequency agile compact array,” in *the 5th European Conference on Antennas and Propagation (EUCAP)*, Rome, 2011.

[98] M. Ibraheam, S. Irteza and M. A. Hein, “Enhancing the radiation efficiency of compact antenna arrays using spatial tilting,” in *The 8th European Conference on Antennas and Propagation (EuCAP)*, The Hague, 2014.

[99] J. Weber, C. Volmer, R. Stephan and M. .. Hein, “Eigenmode decoupling of miniaturised diversity antennas using compact quasi-lumped networks,” in *Antennas and Propagation Conference, LAPC*, Loughborough, 2008.

[100] Perturbation_theory. [Online]. Available: https://en.wikipedia.org/wiki/Perturbation_theory. [Accessed June 2018].

[101] A. G. Derneryd, “A Theoretical Investigation of the Rectangular Microstrip Antenna Element,” *in IEEE Transactions on Antennas and Propagation,* vol. 26, no. 4, pp. 532-535, 1978.

[102] A. H. Mohammadian, N. M. Martin and D. W. Griffin, “A Theoretical and Experimental Study of Mutual Coupling in Microstrip Antenna Arrays,” *IEEE TRANSACTIONS ON ANTENNAS AND PROPAGATION,* vol. 37, pp. 1217-1223, 1989.

[103] T. Huynh, K. F. Lee, S. R. Chebolu and R. Q. Lee, “Mutual coupling between rectangular microstrip patch antennas,” in *IEEE Antennas and Propagation Society International Symposium Digest*, Chicago, IL, USA, 1992.

[104] QCN-19+, “Hybrid couplers,” Mini-Circuits, datasheet available on: https://www.minicircuits.com/pdfs/QCN-19+.pdf.

[105] H. F. Shaban, H. A. Elmikaty and A. A. Shaalan, “STUDY THE EFFECTS OF ELECTROMAGNETIC BAND-GAP (EBG) SUBSTRATE ON TWO PATCHES MICROSTRIP ANTENNA,” *Progress In Electromagnetics Research B,* vol. 10, pp. 55-74, 2008.

[106] P. KOVÁCS and T. URBANEC, “Electromagnetic Band Gap Structures: Practical Tips and Advice for Antenna Engineers,” *RADIOENGINEERING,* vol. 21, no. 1, 2012 .

[107] J. Sandora, “Isolation Improvement with Electromagnetic Band Gap Surfaces,” *LINCOLN LABORATORY JOURNAL,* vol. 19, no. 1, 2012.

[108] COMSOL, “Antenna Decoupling using an Electromagnetic Band Gap Meta-Material,” 2012. [Online]. Available: www.comsol.com/model/antenna-decoupling-using-electromagnetic-band-gap-ebg-metamaterial-12045.

[109] S. D. Cheng, R. Biswas, E. Ozbay, S. McCalmont, G. Tuttle and a. K.-M. Ho, “Optimized dipole antennas on photonic bandgap crystals,” *Applied Physics Letters,* vol. 67, p. 3399–3401, 1995.

[110] R. Coccioli and T. Itoh, “Design of photonic band-gap substrates for surface waves suppression,” in *IEEE MTT-S International Microwave Symposium Digest*, Baltimore, MD, USA, , 1998.

[111] Y. Erdemli and e. al., “Frequency-selective surfaces to enhance performance of broad-band reconfigurable arrays,” *IEEE Transactions on Antennas and Propagation, ,* vol. 50, no. 12, pp. 1716-1724, 2002.

[112] D. Singh, A. Kumar, S. Meena and V. Agarwala, “ANALYSIS OF FREQUENCY SELECTIVE SURFACES FOR RADAR ABSORBING MATERIALS,” *Progress In Electromagnetics Research B,* vol. 38, p. 297–314, 2012.

[113] M. Ghaderi and N. C. Karmakar, “Frequency Selective Surface for reducing mutual coupling in antenna arrays,” in *Asia-Pacific Microwave Conference*, Melbourne, VIC, 2011.

[114] R. Karimian, A. Kesavan, M. Nedil and T. A. Denidni, “Low-Mutual-Coupling 60-GHz MIMO Antenna System With Frequency Selective Surface Wall,” *IEEE Antennas and Wireless Propagation Letters,* vol. 16, pp. 373-376, 2017..

[115] P. Kuravatti and T. S. Rukmini, “Mutual Coupling Reduction Antenna Arrays using Periodic Structures,” *International Journal of Engineering Research & Technology,* vol. 5, no. 5, 2016.

[116] D. R. Jackson, J. T. Williams, A. K. Bhattacharyya, R. L. Smith, S. J. Buchheit and S. A. Long, “Microstrip patch designs that do not excite surface waves,” *IEEE Transactions on Antennas and Propagation,* vol. 41, p. 1026–1037, 1993.

[117] J.-G. Yook and L. Katehi, “Micromachined microstrip patch antenna with controlled mutual coupling and surface waves,” *IEEE Transactions on Antennas and Propagation,* vol. 49, p. 1282–1289, 2001.

[118] N. G. Alexopoulos and D. R. Jackson, “Fundamental superstrate (cover) effects on printed circuit antennas,” *IEEE Transactions on Antennas and Propagation,* Vols. AP-32, p. 807–816, 1984.

[119] Y. Pang, B. Wu, X. Jiang, D. B. Vigneron and X. Zhang, “Tilted Microstrip Phased Arrays With Improved Electromagnetic Decoupling for Ultrahigh-Field Magnetic Resonance Imaging,” *Medicine (Baltimore),* vol. 93(28), 2014.

[120] X. Tang, K. Mouthaan and J. C. Coetzee, “Tunable Decoupling and Matching Network for Diversity Enhancement of Closely Spaced Antennas,” *IEEE Antennas and Wireless Propagation Letters ,* 2012.

[121] C. Volmer, M. Sengul, J. Weber, R.Stephan and M. A. Hein, “Broadband Decoupling and Matching of a Superdirective Two-Port Antenna Array,” *IEEE Antennas and Wireless Propagation Letters,* vol. 7, pp. 613-616, 2008.

[122] S. Irteza, E. Schäfer, M. Ibraheam, B. Bieske, R. Stephan and M. A. Hein, “Beamforming in Compact Antenna Arrays for Robust Satellite Navigation,” in *International Conference on Electromagnetics in Advanced Applications ICEAA*, 2014.

[123] D. M. Pozar, Microwave Engineering, 4th Edition, USA: John Wiley & Sons, Inc., 2011.

[124] G. Luzzatto, “A General 180-Degree Hybrid Ring,” *IEEE Transactions on Broadcasting,* Vols. BC-14, no. 1, pp. 41-43, 1968.

[125] ADS, “Advanced Design System (keysight, formerly Agilent),” Keysight Technologies Inc. (NYSE: KEYS), [Online]. Available: http://www.keysight.com/en/pc-1297113/advanced-design-system-ads?cc=DE&lc=ger. [Accessed 01 09 2017]

[126] Murata, “Murata's products lineup,” Murata, [Online]. Available: https://www.murata.com/en-us/products?intcid5=com_xxx_xxx_cmn_nv_xxx. [Accessed 01 09 2017].

[127] Coilcraft, “Ceramic Chip Inductors,” Coilcraft, [Online]. Available: https://www.coilcraft.com/. [Accessed 01 09 2017].

[128] IMMS-GmbH, “IMMS KOSERNA Annual Report 2016,” [Online]. Available: http://www.imms.de/fileadmin/redaktion/downloads/jahresbericht/fachartikel/2016_IMMS_KOSERNA_AnnualReport_EN_DE.pdf. [Accessed 06 2017].

[129] M. Sgammini, F. Antreich, L. Kurz, M. Meurer and T. G. Noll, “Blind Adaptive Beamformer Based on Orthogonal Projections for GNSS,” in *Proceedings of the 25th International Technical Meeting of The Satellite Division of the Institute of Navigation (ION GNSS 2012)*, Nashville, TN, 2012.

[130] L. Kurz et al., “An architecture for an embedded antenna-array digital GNSS receiver using subspace-based methods for spatial filtering,” in *6th ESA Workshop on Satellite Navigation Technologies (Navitec 2012) & European Workshop on GNSS Signals and Signal Processing*, Noordwijk, 2012.

[131] J.-M. Lim, J. W. Park, K.-J. Lee, H. J. Im, Y.-J. Cho and T. K. Sung, “A precise trajectory estimation method using carrier-smoothed GPS for mobile robots,” in *9th International Conference on Ubiquitous Robots and Ambient Intelligence (URAI)*, Daejeon, 2012.

[132] Z. Xiuqiang, Z. Xiumei and C. Yan, “Implementation of carrier phase measurements in GPS software receivers,” in *International Conference on Computational Problem-Solving (ICCP)*, Jiuzhai, 2013.

[133] B. Falkenberg, P. Fenton, M. E. Cannon and G. Lachapelle, “Precise real-time kinematic differential GPS using a cellular radio modem,” in *IEEE PLANS 92 Position Location and Navigation Symposium Record*, Monterey, CA, USA, 1992.

[134] P. Henkel and A. Sperl, “Real-time kinematic positioning for unmanned air vehicles,” in *2016 IEEE Aerospace Conference,* , Big Sky, MT, 2016.

[135] J. M. Juan et al., “Enhanced Precise Point Positioning for GNSS Users,” *IEEE Transactions on Geoscience and Remote Sensing,* vol. 50, no. 10, pp. 4213-4222, 2012.

[136] P. J. G. Teunissen, “A-PPP: Array-Aided Precise Point Positioning With Global Navigation Satellite Systems,” *IEEE Transactions on Signal Processing,* vol. 60, no. 6, pp. 2870-2881, 2012.

[137] A. Bonetti, “AndroiTS GPS Test Free,” Alessandro Bonetti , [Online]. Available: https://play.google.com/store/apps/details?id=com.androits.gps.test.free&hl=en. [Accessed 2017].

[138] M. A. Hein, R. Stephan, K. Blau, M. Ibraheam and S. Irteza-Butt, “Kompakte Satellitenempfangssysteme für robuste Navigationsanwendungen - KOSERNA : Schlussbericht der TU Ilmenau zum F&E-Verbundvorhaben,” 2017. [Online]. Available: http://edok01.tib.uni-hannover.de/edoks/e01fb17/897149688.pdf. [Accessed 01 12 2017].

Own Publications:

No.	No. In thesis	Publication
1-	[37]	C. Schneider, M. Ibraheam, S. Hafner, M. Kaske, M. A. Hein and R. S Thoma, “On the reliability of multipath cluster estimation in realistic channel data sets,” in *the 8th European Conference on Antennas and Propagation (EuCAP),* The Hague, 2014.
2-	[48]	M. Ibraheam, B. Bieske, K. Blau, E. Schäfer, A. Jäger, S. Butt, R. Stephan and M. A. Hein, “Feasibility of Dual-polarized Antenna Arrays for GNSS Receivers at Low Elevations,” in *11th European Conference on Antennas and Propagation (EuCAP),* Paris, 2017.
3-	[49]	S. Irteza, M. Ibraheam, T. Harz, Y. Bulbin, R. Stephan and M. A. Hein, “Compact Satellite Navigation Antenna Array using Off-the-Shelf Ceramic Patch Antennas,” in *9th European Conference on Antennas and Propagation (EuCAP),* Lisbon, 2015.
4-	[50]	S. Irteza, C. Bornkessel, M. Ibraheam, R. Stephan, F. Wollenschläger, A. Dreher, L. Kurz, M. Meurer, T. Harz, Y. Bulbin and M. A. Hein, “Feld- und Labortests robuster und kompakter Satellitennavigationsempfänger für künftige Fahrautomatisierungen,” in POSNAV, Berlin, 2016.
5-	[51]	M. Ibraheam, S. Irteza, R. Stephan and M. A. Hein, “Dual-band Dual-polarized Stub-loaded Patch Antenna for Robust GNSS Receivers,” in *the 10th European Conference on Antennas*, Davos, 2016.
6-	[69]	M. Ibraheam, S. Irteza, S. Caizzone, A. Dreher, R. Stephan and M. A. Hein, “Compact dual-band dual-polarized antenna array for robust satellite navigation receivers,” in *the 9th European Conference on Antennas and Propagation (EuCAP)*, Lisbon, 2015.
7-	[79]	M. Ibraheam, A. Krauss, S. Irteza and M. A. Hein, “Reduction of Mutual Coupling in Compact Antenna Arrays Using Spatial Tilting,” in *the 8th German Microwave Conference*, GeMiC, Aachen, 2014.
8-	[98]	M. Ibraheam, S. Irteza and M. A. Hein, “Enhancing the radiation efficiency of compact antenna arrays using spatial tilting,” in *the 8th European Conference on Antennas and Propagation (EuCAP)*, The Hague, 2014.
9-	[122]	S. Irteza, E. Schäfer, M. Ibraheam, B. Bieske, R. Stephan and M. A. Hein, “Beamforming in Compact Antenna Arrays for Robust Satellite Navigation,” in *International Conference on Electromagnetics in Advanced Applications ICEAA*, 2014.
10-	[138]	M. A. Hein, R. Stephan, K. Blau, M. Ibraheam and S. Irteza-Butt, “Kompakte Satellitenempfangssysteme für robuste Navigationsanwendungen - KOSERNA : Schlussbericht der TU Ilmenau zum F&E-Verbundvorhaben,” 2017. [Online]. Available: http://edok01.tib.uni-hannover.de/edoks/e01fb17/897149688.pdf. [Accessed 01 12 2017].

List of abbreviations

RF	Radio Frequency
IF	Intermediate Frequencies
GNSS	Global Navigation Satellite Systems
JSR	Jamming-to-Signal Ratio
DMN	Decoupling and Matching Networks
PRN	Pseudo-Random Noise
RHCP	Right Hand Circular Polarization
LHCP	Left Hand Circular Polarization
PPD	Personal Privacy Device
DOP	Dilution of Precision
DoA	Direction of Arrival
IMU	Inertial Measurement Units
INS	Inertial Navigation Systems
XPD	Cross-Polarization Discrimination
PCB	Printed Circuit Board
ML	Mismatching Loss
AR	Axial Ratio
L1	L1/E1-Band (centered at 1.57542 GHz)
L5	L5/E5a-Band (centered at 1.17645 GHz)
LP	Linear Polarizations
ADS	Advanced Design System
ASIC	Application-Specific Integrated Circuit
UMC	United Microelectronics Corporation Technology
DIP	Dual In-Line Package
FPGA	Field-Programmable-Gate-Array
GUI	Graphical User Interface
PVT	Position, Velocity, and Time
CNR	Carrier-to-Noise Ratio
GDOP	Geometric Dilution of Precision
SNR	Signal-to-Noise Ratio
CW	Continuous Wave
KOSERNA	Compact Satellite Receiver System for Robust Navigation Applications
KOMPASSION	Compact Adaptive Terminal Antenna for Interference-Free Satellite Navigation
TU Ilmenau	Technische Universität Ilmenau
DLR	The German Aerospace Center (Deutsches Zentrum für Luft- und Raumfahrt)
IKN	Institut für Kommunikation und Navigation at DLR
IMMS	Institut für Mikroelektronik und Mechatronik Systeme gemeinnützige (IMMS) GmbH
ABB	Antennentechnik Bad Blankenburg (ABB) GmbH
EECS	Chair of Electrical Engineering and Computer Systems at RWTH Aachen University

Erklärung

Ich versichere, dass ich die vorliegende Arbeit ohne unzulässige Hilfe Dritter und ohne Benutzung anderer als der angegebenen Hilfsmittel angefertigt habe. Die aus anderen Quellen direkt oder indirekt übernommenen Daten und Konzepte sind unter Angabe der Quelle gekennzeichnet.

Weitere Personen waren an der inhaltlich-materiellen Erstellung der vorliegenden Arbeit nicht beteiligt. Insbesondere habe ich hierfür nicht die entgeltliche Hilfe von Vermittlungs- bzw. Beratungsdiensten (Promotionsberater oder anderer Personen) in Anspruch genommen. Niemand hat von mir unmittelbar oder mittelbar geldwerte Leistungen für Arbeiten erhalten, die im Zusammenhang mit dem Inhalt der vorgelegten Dissertation stehen.

Die Arbeit wurde bisher weder im In- noch im Ausland in gleicher oder ähnlicher Form einer Prüfungsbehörde vorgelegt.

Ich bin darauf hingewiesen worden, dass die Unrichtigkeit der vorstehenden Erklärung als Täuschungsversuch bewertet wird und gemäß § 7 Abs. 10 der Promotionsordnung den Abbruch des Promotionsverfahrens zur Folge hat.

Ort, Datum Unterschrift

Maysam Ibraheam